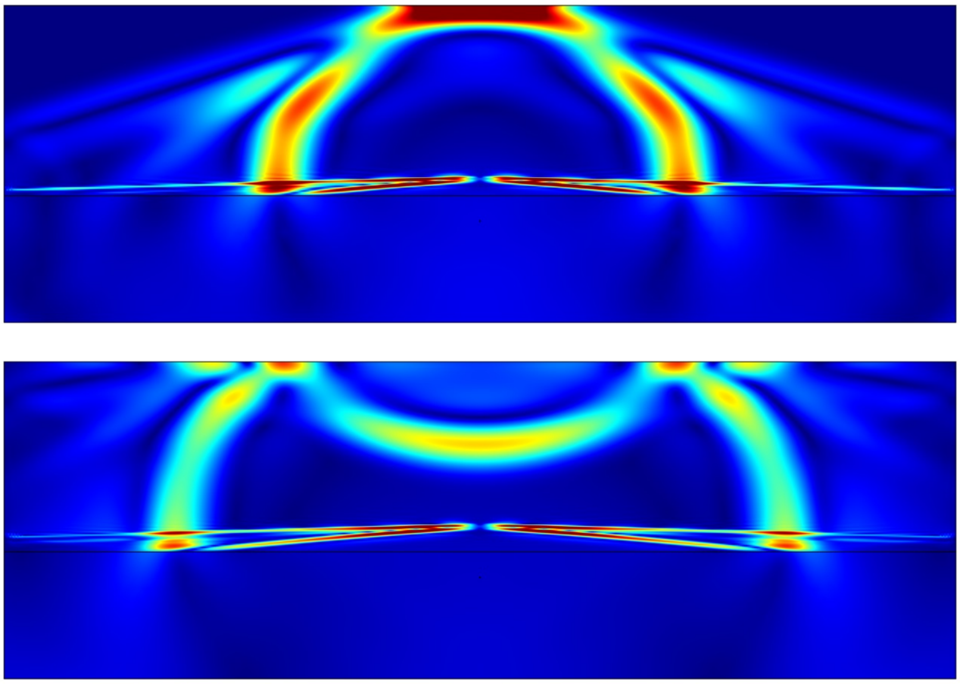

Assessment of the Swedish Standard for blasting induced vibrations

A parametric study on wave propagation in rock and clay using the finite element method

Master's thesis in Structural engineering and building technology

MATTIS DAHL ERIKSSON
AUGUST JANSSON

Department of Mechanics and Maritime Sciences
CHALMERS UNIVERSITY OF TECHNOLOGY
Gothenburg, Sweden 2018

Master's thesis 2018:54

Assessment of the Swedish Standard for blasting induced vibrations

A parametric study on wave propagation in rock and clay using the finite element method

MATTIS DAHL ERIKSSON
AUGUST JANSSON

CHALMERS
UNIVERSITY OF TECHNOLOGY

Department of Mechanics and Maritime Sciences
Division of Dynamics
Chalmers University of Technology
Gothenburg, Sweden 2018

Assessment of the Swedish Standard for blasting induced vibrations
A parametric study on wave propagation in rock and clay using the finite element method
MATTIS DAHL ERIKSSON, AUGUST JANSSON

Supervisor: Peter Olsson, Department of Mechanics and Maritime Sciences
Examiner: Peter Folkow, Department of Mechanics and Maritime Sciences

Master's Thesis 2018:54
Department of Mechanics and Maritime Sciences
Division of Dynamics
Chalmers University of Technology
SE-412 96 Gothenburg
Telephone +46 31 772 1000

Cover: A very nice picture of the wave propagation.

Gothenburg, Sweden 2018

Assessment of the Swedish Standard for blasting induced vibrations
A parametric study on wave propagation in rock and clay using the finite element method
Master of Science Thesis in the Master's Programme Structural Engineering and Building Technology
MATTIS DAHL ERIKSSON
AUGUST JANSSON
Department of Mechanics and Maritime Sciences
Chalmers University of Technology

Abstract

Since 1989 the Swedish Standard for blasting induced vibrations has been based primarily on distance and overburden. However, there is an uncertainty about the fundamentals which the Standard is based on, making room for optimization. The thesis aims to evaluate the Swedish Standard for blasting induced vibrations, by studying velocity- and frequency response of the governing parameters of wave propagation.

A parametric study with numerical models was conducted using finite element method. The parametric study was divided into material and geometrical properties such as degree of saturation, Poisson's ratio, Young's modulus, depth of overburden layer, distance from blast ,and angle of incidence. A poroelastic material model was created by coupling the elastic properties of the solid material with the water stored within the porous structure. The poroelastic material model resulted in velocity- and frequency responses which were comparable with the guidance levels of the Swedish Standard.

In conclusion, distance and overburden are applicable parameters. However, the blasting induced vibration is sensitive to changes in degree of saturation, Poisson's ratio, depth of the overburden surface layer, and to the angle of incidence. As the distance between the blast and the measurement point increases, the frequency range in the vibration was lowered and the risk for damage increases, as buildings are more susceptible to damage at lower frequencies. The P-wave is dominant if the blast is located below the building, however, if the angle of incidence changes, the Rayleigh wave becomes dominant. The frequency response of the Rayleigh wave is lower than for P-waves, thus guidance levels may be set differently depending on which is the dominant wave. A frequency based analysis generates the possibility to combine distance, overburden, material-, geometrical- and possible unidentified parameters, thus simplifying the method of establishing guidance levels for blasting induced vibrations in the soil structure.

Keywords: Blasting, vibrations, Wave propagation, Poroelasticity, Rock blasting, soil, Dynamic finite element analysis, COMSOL, Solid dynamics.

Acknowledgements

First and foremost, we would like to express our sincere gratitude for our supervisor Assoc. Prof. Peter Olsson for continuous support. His enthusiasm, brilliance and immense knowledge on the field of wave propagation helped us deliver this thesis and it is difficult to imagine any better supervisor than him.

Second, we would like to thank our examiner Assoc. Prof. Peter Folkow for giving us the possibility to do this final project in our journey through Chalmers. Doubt was raised during the project, which turned out to have may hidden obstacles, but with his great guidance and remarks, the project was finalized.

We would also like to thank Adj. Prof. Morgan Johansson from Norconsult and Sen. Lec. Joosef Leppänen at Chalmers for their supervision and counseling in meetings regarding blasting and Assoc. Prof. Jelke Dijkstra for consultation regarding poroelastic soil properties.

Lastly, we would like to thank Dr. Mathias Jern at Nitroconsult, Tomas Trapp and Johan Bengtsson at Markera Mark AB for providing the blasting measurements and material data used in the project, and our dear friend Karl Strigén for providing technical support with COMSOL Multiphysics.

Mattis Dahl Eriksson and August Jansson, Gothenburg, June 2018

Contents

1 Introduction

1.1 Background

The West Swedish Agreement is a major infrastructural project made to improve the public transport system in the west of Sweden, with the cost of SEK 34 000 million it includes the West Link, a railway passing through Gothenburg, Hisingsbron, the new bridge over Göta Älv, and the Marieholm Tunnel, a tunnel crossing Göta Älv (Trafikverket n.d).

A part of The West link is a dual-track railway tunnel, which will double the capacity of trains going through Gothenburg, thus relieving the large pressure in today's railway network in west Sweden. A new Central Station will be constructed within the heart of Gothenburg. In addition to the central station, new stations at Korsvägen, Haga and Gamlestadstorget will be constructed making commuting easy for everyone who works, studies or just passes through the city of Gothenburg. The construction of the West Link is planned to start in 2018 and to be due in 2027. (Trafikverket 2016).

The planned railway tunnel is 6 km long passing through both rock and clay, and in order to cut through the bedrock, methods of blasting are planned. There is an interest from both the municipality of Gothenburg and from Chalmers university of technology to further investigate the effects of blasting waves due to the construction of the West link. The vibrations from the blasting may give rise to damage such as cracking and subsidence to about 1600 properties, some properties are historical to the city of Gothenburg and others such as the Sahlgrenska hospital are critical to the city infrastructure and it is crucial that they are not affected negatively.

There are generally two ways to establish guidance levels for vibration. The Swedish Standard is based on distance and overburden type. However, in most international blasting standards, the guidance levels are based on frequency analyses which yield a lower tolerance for vibrations. Building are more susceptible to damage for vibration of lower frequencies (Jern, M. et al. 2013), thus by taking the frequency into account it may be possible to lower the risk of damage from blasting induced vibration.

The basis for the Swedish Standard was created from empirical research by Langefors and Kihlström in the 1960s (Thelin 2009), and the fundamentals of this research is not well documented. There is a large uncertainty for guidance levels set for historical buildings, which today are treated in a rudimentary manner. Thus, there is an interest from Trafikverket to evaluate the possibility of changes in the Swedish Standard.

When the Swedish Standard for calculations on seismic waves from blasting was created, measurements on vibrations were expensive and complicated, therefore it was decided that only the vertical peak particle velocity was economically feasible. In order to make a good prediction on the wave propagation it is necessary to do a multidirectional analysis (Wersäll, C. et al. 2008).

A more thorough understanding of the concepts of blasting and wave propagation in soil and rock creates the possibility of optimizing blasting duration and size of charges, creating the potential to make substantial economic savings during construction.

1.2 Purpose

This report aims to evaluate the Swedish standard for blasting induced vibrations that is in use today. The parameters that the Swedish Standard depend on will be studied in numerical models and the adequacy of the Swedish Standard can be established through a parametric study. The FE-models is based on material data from the construction of the West Link tunnel project, and calibrated with measured blasting data in order to validate the model. The FE-models is created in the FE-software COMSOL Multiphysics.

1.3 Limitations

This master thesis concerns wave propagation from blasting in the ground and how buildings are affected by horizontal and vertical vibrations globally. Structural damage such as cracking and failure in buildings is not included in the report.

The soil profile is modeled in 2D, with plane stress conditions.

The thesis assumes that no plastic deformations will occur in the soil and the rock.

1.4 Clarification of questions

The governing parameters, distance and overburden, used in the Swedish Standard determines the guidance level as PPV. However, as the risk of damage in buildings increase when subjected to vibrations with low frequencies, there is a need to establish a relationship between distance and overburden and the frequency of the vibration.

Furthermore, as the Swedish Standard is based primarily on distance and overburden, there is a possibility that parameters which has a large influence on the vibrations are not included. Differences in frequencies caused by geometrical, material and blasting parameters that are not included in the Swedish Standard should therefore be investigated.

As the Swedish Standard only takes the vertical vibration in one point of measurement into account, horizontal vibrations should be studied.

1.5 Thesis disposition

A literature study is done in order to describe the physics behind wave propagation in elastic and poroelastic material. Furthermore the study describes rock and soil properties with focus on the geological situation in Gothenburg. The literature study also describes the Swedish standard as it is used today together with a comparison on how blasting standards are used internationally.

The wave propagation is then described in FE formulation in order to do a 2D numerical wave propagation analysis.

Furthermore, a parametric study is done in the FE-software COMSOL Multiphysics. The model is based on material data obtained from Markera and calibrated with measured velocity time response curves obtained from Nitroconsult in order to determine the reliability of the model. This aims to evaluate and assess the Swedish Standard for blasting.

2
Theory

2.1 Soil properties

According to Knappett (2012), soil can be defined as any uncemented or weakly cemented mass of mineral particles that have been formed by erosion of rock. In the following chapters the term rock refers to the bedrock. Furthermore, the mineral particles that the soil consists of is grouped in the categories of clay, silt, sand, gravel, cobbles and boulders dependent on the diameter of the particle. In the Swedish literature there are subcategories for each particle category, as seen in Table 2.1 (Sällfors 2001).

Particle	**Size ranges** [mm]
Fine Clay	<0.0006
Course Clay	0.0006 - 0.002
Fine Silt	0.002 - 0.006
Medium Silt	0.006 - 0.02
Course Silt	0.02 - 0.06
Fine Sand	0.06 - 0.2
Medium Sand	0.2 - 0.6
Course Sand	0.6 - 2
Fine Gravel	2 - 6
Medium Gravel	6 - 20
Course Gravel	20 - 60
Medium Cobbles	60 - 200
Course Cobbles	200 - 600
Boulders	>600

Table 2.1: Particle sizes according to the Swedish nomenclature (Sällfors 2001).

The soil behaviour is heavily influenced by the proportions of particle sizes which it contains. Soils which is governed by the behaviour of clay and silt is referred to as fine-grained soils and soils which are governed by the behaviour of particles of sand size and gravel are called coarse-grained soils (Knappett 2012).

The soil can be described as grains of particles in different sizes that are mechanically interlocked, between the grain particles there are voids and tunnels creating a porous material system and illustrated schematically in Figure 2.1. Porosity is the ratio between the volume of voids in the soil and the total volume of the soil. The voids in the soil are called pores and can either contain water or air. When water enters the pores in the soil structure, a pore pressure occurs and increases with soil depth. This pore pressure contributes to the strength of the soil by withstanding some of the stresses applied on the soil. Consequentially, the soil skeleton will only be exposed to effective stress, σ', defined according to (Knappett 2012) as

$$\sigma' = \sigma - u_p \tag{2.1}$$

where σ is the total stress applied on the soil and u_p is the pore pressure (Knappett 2012).

Furthermore, water have a possibility to flow through the porous structure of the soil. A schematic visualization of a porous structure containing water is seen in Figure 2.1, the size of the material grains can vary with the particle sizes seen in Table 2.1. The transport of fluid occurs in the tunnels between the pores; this is described as the soil permeability. The permeability of the soil materials are heavily dependent by the soil type: coarse-grained soils have more open network of tunnels than fine-grained soil, as seen in Table 2.2 (Knappett 2012).

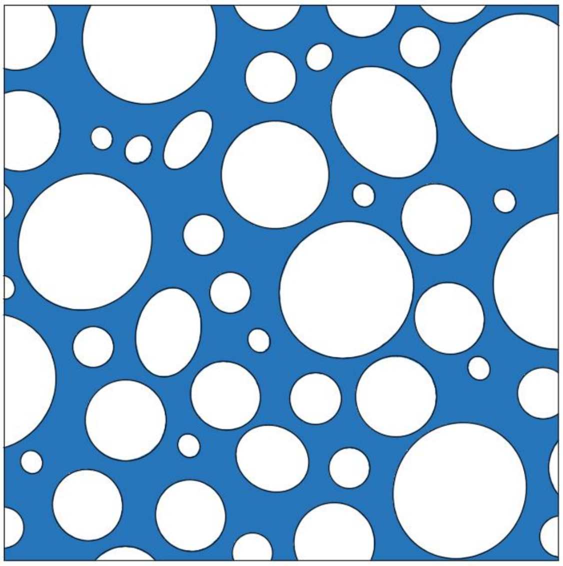

Figure 2.1: Porous and permeable material, the blue colour shows the water.

Soil type	**Permeability [m/s]**
Clean gravel	$1 - 10^{-1}$
Clean sand, mixtures of sand and gravel	$10^{-2} - 10^{-4}$
Silts, laminates of clay and silt, very fine sand	$10^{-5} - 10^{-7}$
Unfissured clays	$10^{-8} - 10^{-10}$

Table 2.2: Permeability of soils dependent of particle sizes.

Equally important is the soil's dependency on the load duration. If an applied load remains during a long time, water will be pressed out of the porous structure; this phenomenon is referred to as consolidation. For short term loads, the process of consolidation may not occur. It is therefore possible to divide the response of soils into two categories: drained and undrained response. The soil will have a drained response if it has consolidated, in other words if fluid has been drained from the structure, as in the case of long term loads. For short term loads, the soil will have an undrained response (Knappett 2012).

2.1.1 Elastic soil model

The elastic soil model is based on the assumption that the stress in the material is proportional to the strain. In order to define the proportionality, some parameters have to be defined. The most common elastic parameters for soil are the bulk modulus, K, shear modulus, G, Young's modulus, E, and Poisson's ratio ν (Gopalakrishnan 2016). However, the most important soil parameter for wave propagation is the shear modulus which accounts for how the material behaves when its affected by shearing (Hall 2013). The shear modulus is defined as the difference in shear stress per change of angle, see Figure 2.2a.

$$G = \frac{\partial \tau}{\partial \gamma} \tag{2.2}$$

The bulk modulus is the volumetric strain proportional to the pressure on the material, see as

$$K = \frac{\partial P}{\partial V} \tag{2.3}$$

where V is the volume and P is the effective pressure.

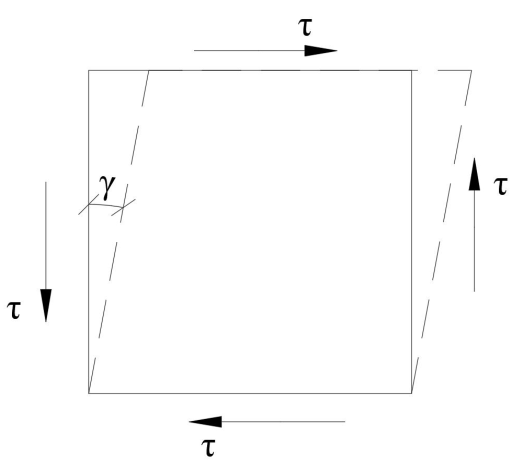

(a) Stress-strain relation for shearing in a material.

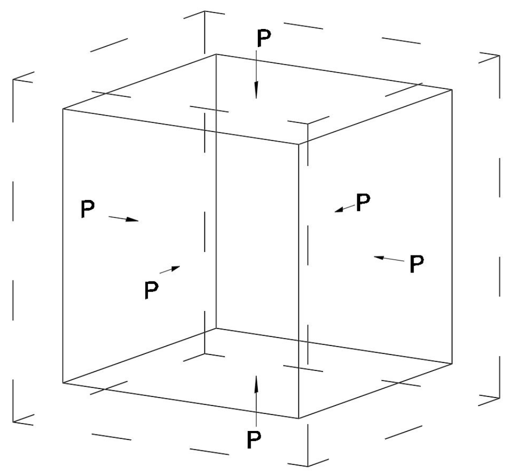

(b) Stress-strain relation for the volumetric change in the material

Figure 2.2: Constitutive relations for the elastic model.

The bulk modulus, K, which is dependent on the effective stress in the soil, increases with an increased value of the effective stress. For homogeneous soils, laboratory tests confirm that the stiffness tend to increase linearly with the depth of the soil material (Verruijt 2010).
Young's modulus is defined as the proportion of strain and stress in one direction only, and can be written as a function of the bulk modulus and the shear modulus as (Gopalakrishnan 2016)

$$E = \frac{3G}{1 + \frac{G}{K}}. \tag{2.4}$$

Another way of writing it is by using Poisson's ratio, which is a parameter describing the volumetric change perpendicular to the applied stress. Young's modulus can then be written in terms of Poisson's ratio as

$$E = 2G(1 + \nu). \tag{2.5}$$

According to Larsson (2008), fully water saturated soil materials can be considered as incompressible material, which is equivalent to $K \to \infty$ and $\nu \to 0.5$. Equation 2.5 can then be expressed as

$$E = 3G. \tag{2.6}$$

2.1.2 Nonlinear soil model

As mentioned Section 2.1.1, the most important parameter in the soil is the shear modulus which is described by equation 2.2. However, in reality, the shear modulus decreases with increased shear strain (Darendeli 2001). In Figure 2.3, the relation between the strain and the shear modulus is described as well as the secant modulus.

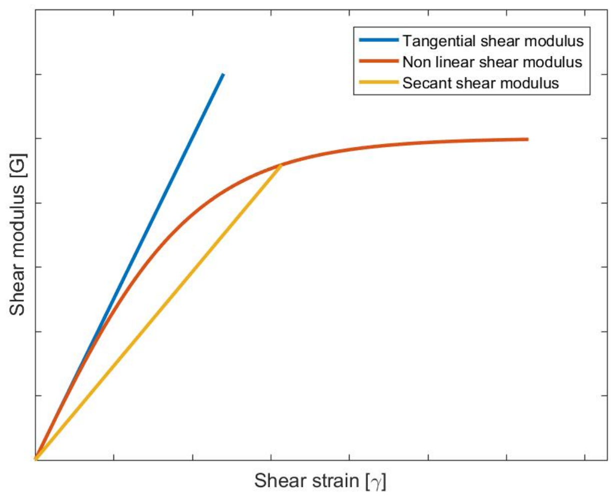

Figure 2.3: A schematic figure describing the nonlinear behaviour of soil and the simplification of the shear modulus.

The secant modulus is the average modulus between 0 and γ. Figure 2.3 also presents the tangential modulus, which is the initial shear modulus and valid for small strains in the material (Larsson 2008).

2.1.3 Poroelastic soil behaviour

The theory of poroelasticity was introduced by Biot M. A. in 1956 in order to describe wave propagation in porous elastic solids containing compressible viscous fluids (Biot 1956). Poroelastic material behaviour has been used to describe soils in applications such as settlements due to consolidation (Jueun & Selvadurai 2016), group interaction on piles (Jueun & Selvadurai 2014), soil retaining walls (Papagiannopoulos et al. 2015) and earthquake engineering (Lubis et al. 2012).

Soil materials contains pores that may or may not be filled with fluids. The elastic model is expanded into the concept of poroelasticity through two couplings between changes in stress in the solid and changes of pore pressure from the fluid. There occurs a solid-to-fluid coupling effect in the material when the applied stress is changed, the change in stress will generate a change in pore pressure. Also, there is a fluid-to-solid coupling effect in the soil when a change in pore pressure generates a volumetric change in the soil material (Wang 2000).

In order to describe the coupling effects above, poroelastic material parameters needs to be introduced. The important material parameters for poroelasticity are drained and undrained bulk modulus, poroelastic expansion coefficient, and the constrained storage coefficient. The relation between the drained and the undrained bulk modulus is that the drained bulk modulus only carries load through the porous skeleton frame, whereas the undrained bulk modulus also carries weight due to the fluid resisting compression. The poroelastic expansion coefficient is defined as the change in bulk volume with regards to a change in pore pressure, while the applied stress remains constant. The constrained storage coefficient can be defined as the ratio of change in fluid content in the porous structure, due to a change in pore pressure while the structure is under constant strain (Wang 2000).

The material parameters described above are used to determine the Biot-Willis coefficient, α, which is the drained bulk modulus multiplied with the poroelastic expansion coefficient. The Biot-Willis coefficient can be interpreted as the ratio of pore pressure that cancel out the applied stress. For example, if $\alpha \approx 1$, the pore pressure will counteract almost all applied stress, and the structure will be almost in-compressible. Materials such as clay, with low permeability will have a Biot-Willis coefficient, $\alpha \approx 1$ (Wang 2000).

In addition to the parameters described above, an important parameter for poroelastic materials is the compressibility, β, of the fluid within the porous structure. Water in itself has a very low compressibility of $\beta_0 = 0.5 \times 10^{-9}$ m^2/N. However in a soil system, the porous skeleton has a large influence on the compressibility. The compressability can be expressed as (Verruijt 2010)

$$\beta = S\beta_0 + \frac{1-S}{p_0} \tag{2.7}$$

where p_0 is the absolute pressure and S is the degree of saturation which describes the amount of water stored in the porous system. However, in a porous soil system, there will always be small bubbles of air trapped within the structure, even below the phreatic surface level. At atmospheric pressure $p_0 = 100$ kPa, a one percent decrease in saturation from fully saturated at $S = 1$ to $S = 0.99$ will yield a 200 times increase in compressibility $\beta(S = 0.99) = 1 \times 10^{-7}$ m^2/N (Verruijt 2010).

Another important parameter for poroelasticity is the dynamic viscosity, η, which can be described as the shear deformation resistance of the fluid within the pore structure. The dynamic viscosity is temperature dependent parameter which is measured in Pa $\cdot$ s (Dynamic Viscosity 2015). The dynamic viscosity for water with a temperature of 10° C is $1.3076 \cdot 10^{-3}$Pa $\cdot$ s (Engineering Toolbox 2004).

2.1.4 Soil profile

The soil profile is heavily dependent on the geological history of location. Generally there are several different soil profiles. However, four common soil profiles with distinctive characteristics can be determined. Firstly, cohesion soil materials such as different types of clay which lies on top of bedrock. Secondly, frictional material such as sand or moraine, also lying on top of bedrock. The third and fourth are combinations of frictional material above cohesion material and vice versa, both lying on top of bedrock. However, although not a soil profile, rock reaching above the soil is also a common situation (Knappett 2012).

In order to make an estimate of the behaviour of the soil, the soil profile must be determined. The soil profile describes the layering of different material in the soil from the bedrock to the soil surface, an example of a soil profile is seen in Figure 2.4. The soil surface and top layer is often exposed to erosion due to rain, cycles of freeze and thaw and influence of human impact. These effect of erosion on the soil surface disturbs the material behaviour of the soil. The disturbed layer is often described as fill (Knappett 2012).

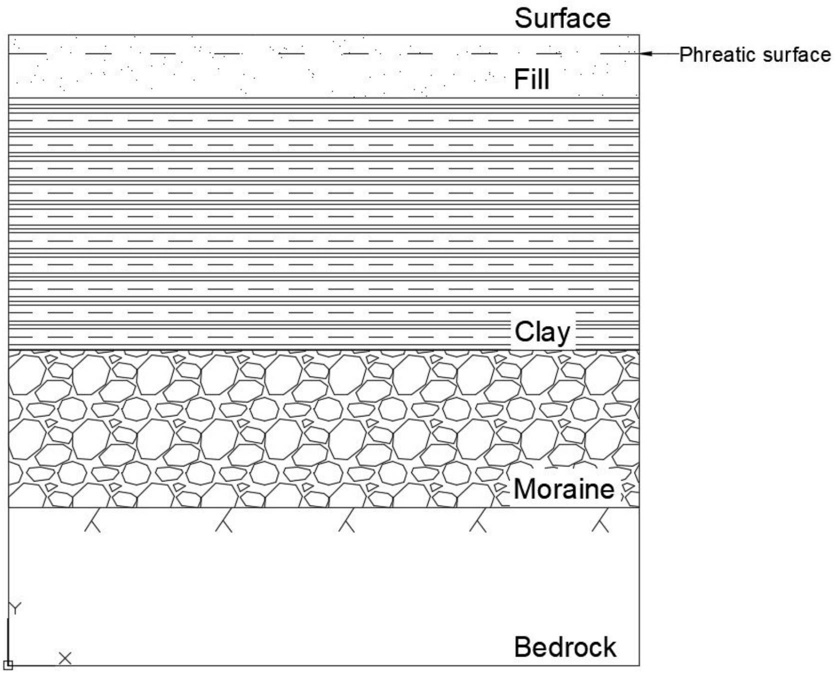

Figure 2.4: Example of a soil profile.

The soil profile can be determined by means of previously measured and new site investigation (Knappett 2012). Previously measured data can be obtained at various databases, for example, the Geological Survey of Sweden (Geological Survey of Sweden n.d). New site investigation is then done if more data needs to be obtained for the actual site.

In chapter 4.1, the specific soil profile for two sections in the city of Gothenburg is described. The soil profiles where determined through site investigations at two separate locations, one at Haga and the other at Liseberg, which is adjacent to Korsvägen. The models used in the parametric study are based on these soil profiles.

2.2 Elastic wave propagation

A mechanical wave can be defined as energy transported from one location to another, without the transport of any material. It is a propagation of mechanical energy that requires a medium such as a solid body. The speed of the wave is dependent on the material properties of the medium, generally a material with higher density such as steel will pass mechanical waves faster than in in a lower density material such as rock (Gopalakrishnan 2016).

In an infinite elastic body, where no boundary conditions affect the wave propagation, there are two types of waves. The primary wave, P-wave, is the fastest and the particles move in the direction of the wave, shown in Figure 2.5. In the secondary wave, S-wave, shown in Figure 2.6, the particles move perpendicular to the direction of the wave and it is slower than the P-wave (Hall 2013).

The P-wave propagates in the longitudinal direction. When a P-wave propagates through a material, the material is initially compressed and then elongated in the direction of the wave (Hall 2013).

In S-waves, the particles move perpendicluar to the direction of the propagating wave, and generates shear deformations in the material. The S-waves can have either in-plane or out-of-plane motion. An S-wave with in-plane motion is called SV-wave, and an S-wave with out-of-plane motion is called SH-wave. In fluids, such as water, which does not have any shear resistance, S-waves cannot propagate (Hall 2013).

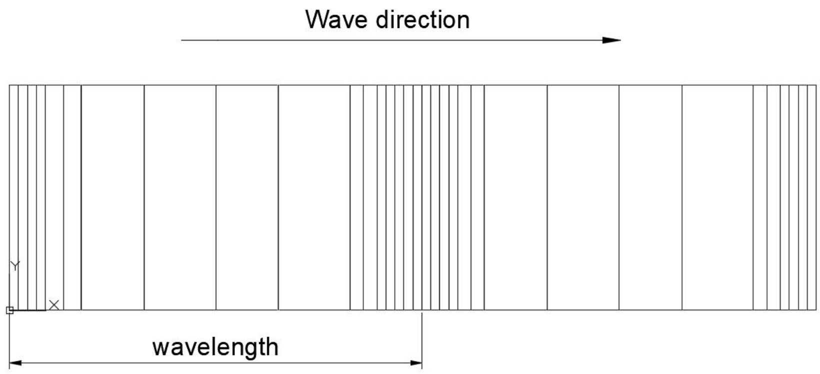

Figure 2.5: P-wave.

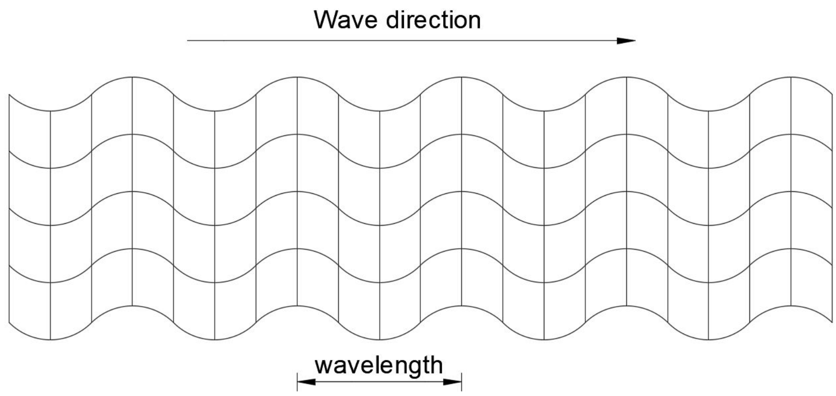

Figure 2.6: S-wave

Finite elastic bodies require boundary conditions. Such boundary conditions can be for example the material surface and interfaces between materials. These boundary conditions will give rise to surface waves, reflection and refraction of the indecent waves, as explained in Section 2.2.4 (Olsson 1990).

The soil material will determine how fast the wave from the source will propagate and how much energy that is left when the wave reaches the buildings. In rock and soils, the wave speed of the P-wave varies from 500 m/s to roughly 5000 m/s. The S-wave, which can only propagate through solid material, ranges in the wave speeds of 1 m/s to 2500 m/s (Möller, B. et al. 2017). The wave speed can be calculated as

$$c = \frac{\Lambda}{f} \tag{2.8}$$

where Λ is the wavelength and f is the frequency of the wave.

2.2.1 Equation of motion

Consider a solid body of an elastic, homogeneous and isotropic material which is loaded in one or more directions. The deformation of the body is described by the field components, u, v and w which are parallel to the x, y and z directions, respectively. In each infinitesimal part of the body, stresses act due to forces in all directions. In Figure 2.7, the stresses in the x-direction are shown.

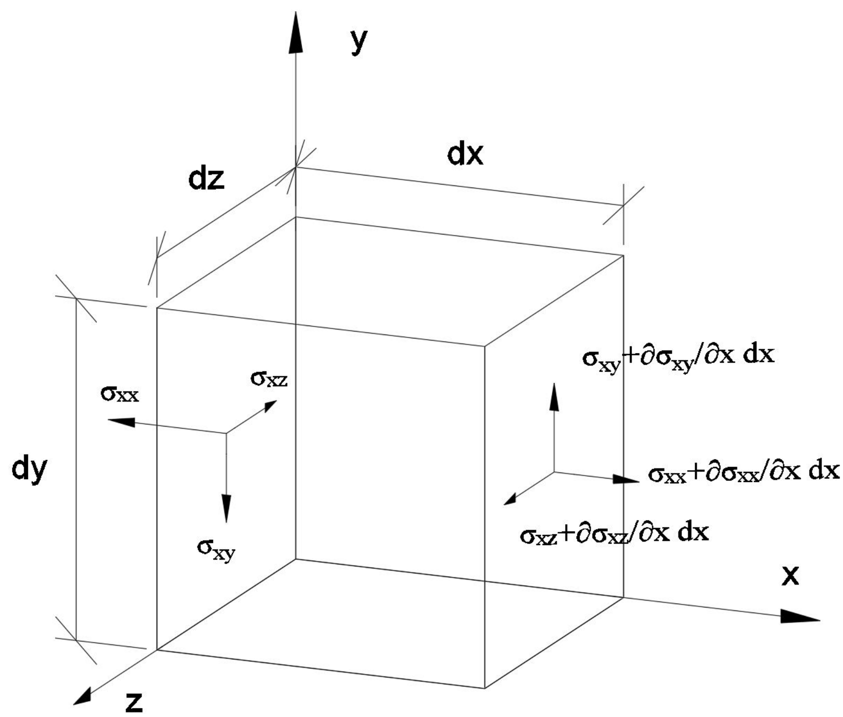

Figure 2.7: An infinitesimal part of an elastic material with stresses in the x-direction.

The equations of motion can be expressed in terms of stresses. Firstly all forces acting in the infinitesimal part of the body is summed in each direction according to equation 2.9 where all forces in the x-direction is summed (Rao 2007).

$$\sum F_x = \Big(\sigma_{xx} + \frac{\partial \sigma_{xx}}{\partial x} dx\Big) dydz - \sigma_{xx} dydz + \Big(\sigma_{xy} + \frac{\partial \sigma_{xy}}{\partial y} dy\Big) dxdz \\ - \sigma_{xy} dxdz + \Big(\sigma_{xz} + \frac{\partial \sigma_{xz}}{\partial z} dz\Big) dxdy - \sigma_{xz} dxdy \tag{2.9}$$

Secondly, using Newton's second law, that the mass times acceleration is equal to the forces in that direction, gives equation 2.10.

$$\frac{\partial \sigma_{xx}}{\partial x} + \frac{\partial \sigma_{xy}}{\partial y} + \frac{\partial \sigma_{xz}}{\partial z} = \rho \frac{\partial^2 u}{\partial t^2} \tag{2.10}$$

The same procedure made in equations 2.9 and 2.10 is done in the other directions, v and w, as well.

In order to calculate the stresses in equation 2.10, Lamé's material constants, λ and μ are introduced. Lamé's constants are based on Hooke's law which describes the constitutive relation between stress, σ, and strain, ε. The constants are given by equations 2.11 and 2.12.

$$\lambda = \frac{\nu E}{(1+\nu)(1-2\nu)} \tag{2.11}$$

$$\mu = \frac{E}{2(1+\nu)} = G \tag{2.12}$$

where E is Young's modulus of elasticity, ν is Poisson's ratio and G is the shear modulus.

For stresses in the normal direction, equation 2.13 is used, while for stresses in the transverse direction, equation 2.14 is used.

$$\sigma_{ii} = \lambda \Delta + 2\mu \varepsilon_{ii} \qquad \not\Sigma_{ii} \tag{2.13}$$

$$\sigma_{ij} = \mu \varepsilon_{ij} \quad \text{where} \quad i \neq j \tag{2.14}$$

where $\Delta = \varepsilon_{xx} + \varepsilon_{yy} + \varepsilon_{zz}$.

The strain-displacement relation is defined as strain being the derivative of displacement in the normal direction. In the transverse direction, the strain is defined as the sum of the derivatives in each direction. The strains in the x-directions is written as

$$\varepsilon_{xx} = \frac{\partial u}{\partial x} \tag{2.15}$$

$$\varepsilon_{xy} = \frac{1}{2}\left(\frac{\partial u}{\partial y} + \frac{\partial v}{\partial x}\right) \tag{2.16}$$

$$\varepsilon_{xz} = \frac{1}{2}\left(\frac{\partial u}{\partial z} + \frac{\partial w}{\partial x}\right). \tag{2.17}$$

Combining equation 2.10 with equations 2.13 to 2.17 gives the equation of motion in the x-direction.

$$\frac{\partial}{\partial x}\left(\lambda\Delta + 2\mu\frac{\partial u}{\partial x}\right) + \frac{\partial}{\partial y}\left(\mu\left(\frac{\partial v}{\partial x} + \frac{\partial u}{\partial y}\right)\right) + \frac{\partial}{\partial z}\left(\mu\left(\frac{\partial w}{\partial x} + \frac{\partial u}{\partial z}\right)\right) = \rho\frac{\partial^2 u}{\partial t^2} \tag{2.18}$$

This equation can be rewritten as

$$(\lambda + \mu)\frac{\partial \Delta}{\partial x} + \mu\nabla^2 u = \rho\frac{\partial^2 u}{\partial t^2} \tag{2.19}$$

with

$$\nabla = \begin{bmatrix} \frac{\partial}{\partial x} \\ \frac{\partial}{\partial y} \\ \frac{\partial}{\partial z} \end{bmatrix} \tag{2.20}$$

The same procedure is made for the y and z directions as well, resulting in

$$(\lambda + \mu)\nabla(\nabla \cdot \mathbf{u}) + \mu\nabla^2\mathbf{u} = \rho\ddot{\mathbf{u}} \tag{2.21}$$

here $\mathbf{u}$ is the vector field in all three directions and where $\ddot{\mathbf{u}}$ is the second order time derivative of the displacements.

2.2.2 Wave types

The displacement vector field described above, see equation 2.21, can be divided into P- and S-waves using Helmholtz decomposition theorem (Hagedorn 2007)

$$\mathbf{u}(x, y, z, t) = \mathbf{u}_{\mathrm{P}}(x, y, z, t) + \mathbf{u}_{\mathrm{S}}(x, y, z, t) \tag{2.22}$$

with the curl and divergence properties

$$\nabla \times \mathbf{u}_{\mathrm{P}} = 0, \qquad \nabla \cdot \mathbf{u}_{\mathrm{S}} = 0 \tag{2.23}$$

where the displacement vector field pertaining to the P-waves are $\mathbf{u}_{\mathrm{P}}$ and the S-waves are $\mathbf{u}_{\mathrm{S}}$. By combining equation 2.22 with the equation of motion, 2.21, together with the curl and divergence properties above, it is possible to write the differential equation

$$(\lambda + \mu)\nabla\Big[\nabla \cdot (\mathbf{u}_{\mathrm{P}} + \mathbf{u}_{\mathrm{S}})\Big] + \mu\nabla^2(\mathbf{u}_{\mathrm{P}} + \mathbf{u}_{\mathrm{S}}) = \rho(\ddot{\mathbf{u}}_{\mathrm{P}} + \ddot{\mathbf{u}}_{\mathrm{S}}) \tag{2.24}$$

It can be shown (Hagedorn 2007) that by separately taking the divergence and the curl of equation 2.24 and using properties in 2.23, that the differential equations for the P-wave and S-wave can be written as

$$c_P^2\nabla(\nabla\cdot\mathbf{u}_\mathrm{P})=\ddot{\mathbf{u}}_\mathrm{P}\qquad \mathrm{c}_\mathrm{P}=\sqrt{\frac{\lambda+2\mu}{\rho}} \tag{2.25}$$

$$-c_S^2\nabla(\nabla\times\mathbf{u}_\mathrm{S})=\ddot{\mathbf{u}}_\mathrm{S}\qquad \mathrm{c}_\mathrm{S}=\sqrt{\frac{\mu}{\rho}} \tag{2.26}$$

where c_P and c_s are the speed of the waves.

2.2.3 Wave equation

In order to solve the wave equations 2.25 and 2.26, the curl and divergence conditions, 2.23 are used again. For a wave in one dimension along the x-axis the curl condition gives for the vector field $\mathbf{u}_\mathrm{P}(x,t)$ that the particles only move in the same direction.

$$\mathbf{u}_\mathrm{P}=(u_{Px},0,0)^\mathrm{T} \tag{2.27}$$

For the same one dimensional wave, the divergence of the vector field $\mathbf{u}_\mathrm{S}$ shows that the particles move in the perpendicular directions of the wave.

$$\mathbf{u}_\mathrm{S}=(0,u_{Sy},u_{Sz})^\mathrm{T} \tag{2.28}$$

Equations 2.27 and 2.28 can be solved with a harmonic wave solution, such as

$$u(x,t)=e^{i(kx-\omega t)} \tag{2.29}$$

where k is the wavenumber and ω is the circular frequency in Hz.

Now, considering a two dimensional plane, the direction of a wave can be described by a unit vector $\hat{\mathbf{n}}=(\cos\theta,\sin\theta,0)^\mathrm{T}$ where θ is an angle of direction. The wave equation for P-waves, 2.25, can be solved in two dimensions as

$$\mathbf{u}_\mathrm{P}(x,y,t)=A_P\hat{\mathbf{n}}e^{ik_P(x\cos\theta+y\sin\theta-c_Pt)} \tag{2.30}$$

where A_P is the amplitude of the P-wave and k_P is the wave number.

For equation 2.26, the vector $\hat{\mathbf{a}}=(0,0,1)$ is introduced, which is a direction perpendicular to $\hat{\mathbf{n}}$. The other perpendicular direction is given from the cross product of $\hat{\mathbf{a}}$ and $\hat{\mathbf{n}}$.

$$\hat{\mathbf{a}}\times\hat{\mathbf{n}}=(-\sin\theta,\cos\theta,0)^\mathrm{T} \tag{2.31}$$

The solution to the differential equation for S-waves, 2.26, can now be written as

$$\mathbf{u}_\mathrm{S}(x,y,t)=A_V\hat{\mathbf{a}}\times\hat{\mathbf{n}}e^{ik_S(x\cos\theta+y\sin\theta-c_St)}+A_H\hat{\mathbf{a}}e^{ik_S(x\cos\theta+y\sin\theta-c_St)} \tag{2.32}$$

where A_V and A_H are amplitudes for the SV-wave and SH-wave, respectively. Combining equations 2.30 and 2.32 gives the total displacement field. The field can then be split into components in each direction as follows (Hagedorn 2007)

$$u = A_P \cos\theta e^{ik_P(x\sin\theta + y\cos\theta - c_P t)} - A_V \sin\theta e^{ik_S(x\sin\theta + y\cos\theta - c_S t)} \tag{2.33}$$

$$v = A_P \sin\theta e^{ik_P(x\sin\theta + y\cos\theta - c_P t)} + A_V \cos\theta e^{ik_S(x\sin\theta + y\cos\theta - c_S t)} \tag{2.34}$$

$$w = A_H e^{ik_S(x\sin\theta + y\cos\theta - c_S t)} \tag{2.35}$$

2.2.4 Boundary Conditions

The above mentioned P- and S-waves propagate through infinite solid medium without any boundary conditions. The inclusion of a boundary conditions, for example the ground surface, can reflect the wave or give rise to surface waves. Also, at an interaction between two materials, the waves will refract and reflect (Hagedorn 2007).

2.2.4.1 Reflection on a free surface

Each kind of wave, P-wave, SV-wave and SH-wave behave different when reflecting against a boundary. In an elastic plane, with a free surface, the P-wave and SV-wave both reflects a P-wave and a SV-wave while the SH-wave only reflects another SH-wave (Hagedorn 2007). As the study is focused on 2D wave propagation, the out-of-plane SH-wave can be excluded from the study (V.W. L et. al 2014).

For a free boundary, the stresses on the surface must be zero. That is, for a two dimensional wave in the x-y-plane with a boundary at $y = 0$, the stresses in all directions is zero.

$$\sigma_{yy} = 0 \quad \text{at} \quad y = 0 \tag{2.36}$$

$$\sigma_{xy} = 0 \quad \text{at} \quad y = 0 \tag{2.37}$$

For a P-wave, reflected at a free surface, the wave field can be represented as two P-waves and one SV-wave

$$\begin{aligned} \mathbf{u}(x, y, t) = {} & A_{P0}\hat{\mathbf{n}}_{\mathrm{P0}} e^{ik_{P0}(x\cos\theta_{P0} + y\sin\theta_{P0} - c_P t)} + A_P\hat{\mathbf{n}}_{\mathrm{P}} e^{ik_P(x\cos\theta_P - y\sin\theta_P - c_P t)} \\ & + A_V\hat{\mathbf{a}} \times \hat{\mathbf{n}}_{\mathrm{V}} e^{ik_S(x\cos\theta_V - y\sin\theta_V - c_S t)} \end{aligned} \tag{2.38}$$

where A_{P0}, A_P and A_V is amplitudes for the incoming P-wave, the reflected P-wave and the reflected S-wave respectively. The unit vectors $\hat{\mathbf{n}}_{\mathrm{P0}}$, $\hat{\mathbf{n}}_{\mathrm{P}}$ and $\hat{\mathbf{n}}_{\mathrm{V}}$ are the direction of the incoming P-wave, the outgoing P-wave and the outgoing S-wave respectively. The directions of the waves θ can be seen in Figure 2.8.

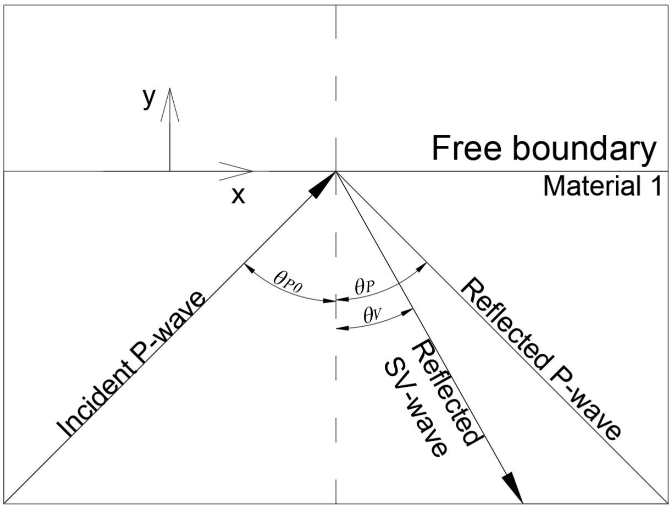

Figure 2.8: An incident P-wave reflected on a free boundary. The angles for the reflected P-wave and SV-wave are shown in the figure.

In order to satisfy the boundary conditions, the incoming P-wave and the reflected P-wave will have the same angle and the angle of the outgoing SV-wave can be calculated using Snell's law by

$$\frac{\sin\theta_P}{\sin\theta_V} = \frac{c_P}{c_V} = \kappa \tag{2.39}$$

The SV-waves behave in a similar manner. The two dimensional vector field of displacement for a reflected SV-wave can be written as

$$\begin{aligned}\mathbf{u}(x,y,t) = A_{V0}\hat{\mathbf{n}}_{\mathrm{V0}} e^{ik_{V0}(x\cos\theta_{V0}+y\sin\theta_{V0}-c_P t)} + A_P\hat{\mathbf{n}}_{\mathrm{P}} e^{ik_P(x\cos\theta_P - y\sin\theta_P - c_P t)}\\ + A_V\hat{\mathbf{a}}\times\hat{\mathbf{n}}_{\mathrm{V}} e^{ik_S(x\cos\theta_V - y\sin\theta_V - c_S t)}\end{aligned} \tag{2.40}$$

and can be seen in Figure 2.9.

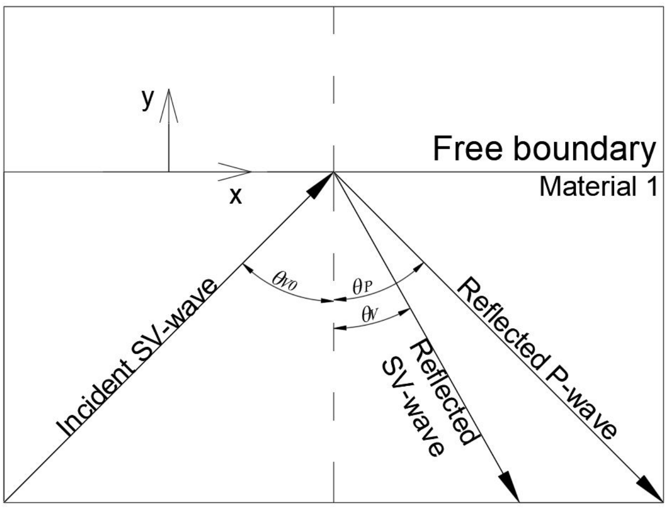

Figure 2.9: An incident SV-wave reflected on a free boundary. The angles for the reflected P-wave and SV-wave are shown in the figure.

As for the P-wave, in order to satisfy the boundary conditions, the angle of the incident SV-wave have the same angle as the reflected SV-wave (Hagedorn 2007).

2.2.4.2 Material interfaces

In an elastic body, consisting of different layers of material where each material have their own properties, the interfaces between the layers have an influence on the wave propagation. At an interface between two layers the wave split into two parts, one refracted and one reflected. What governs the direction of the refracted and reflected parts of the wave is the angle of incidence, the wave speed and the density of the materials (Hall 2013).

When a P-wave reaches the interface between two materials with different properties the refracted part contain a refracted P-wave and a refracted SV-wave. Also, the reflected part contains a reflected P-wave and a reflected SV-wave, as seen in Figure 2.10a (Hall 2013).

In the same way, when an incoming SV-wave reaches the interface, the refracted part includes a refracted SV-wave and a refracted P-wave. The reflected part of the wave contains a reflected SV-wave and a reflected P-wave 2.10b (Hall 2013).

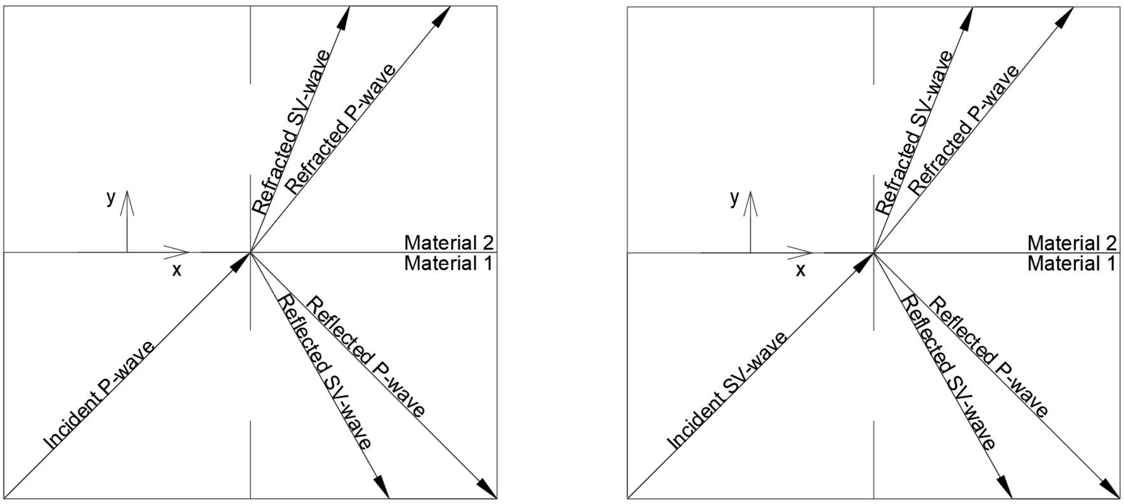

(a) Incident P-wave **(b)** Incident SV-wave

Figure 2.10: Reflection and refraction of P- and SV-waves.

When a P-wave reaches the interface between two solid materials with different material properties, it may give rise to Stoneley waves which travel along the interface of two half-spaces. The Stoneley waves, which is a combination of P- and S-waves and has a lower wave speed than P-waves, decreases exponentially as the distance from the interface increases (Flores-Mendez, E. et al. 2012). However, Stoneley waves cannot exist in all solid-solid interfaces, as their existance is dependent on the material properties of the solids (Chadwick & Borejko 1994).

The displacement field at an interface between two elastic solids can be written as

$$\mathbf{u}_2(x, y, t) = \mathbf{u}_{2\text{P}}(x, y, t) + \mathbf{u}_{2\text{S}}(x, y, t) \tag{2.41}$$

$$\mathbf{u}_1(x, y, t) = \mathbf{u}_{1\text{P}}(x, y, t) + \mathbf{u}_{1\text{S}}(x, y, t) \tag{2.42}$$

with $\mathbf{u}_{2\text{P}}$ and $\mathbf{u}_{2\text{S}}$ from Equation 2.30 and $\mathbf{u}_{1\text{P}}$ and $\mathbf{u}_{1\text{S}}$ from Equation 2.32. The indices 1 and 2 is dependent on the domain, as seen in Figure 2.10. The boundary conditions that needs to be fulfilled at the interface is

$$\mathbf{u}_2(x, y, t) - \mathbf{u}_1(x, y, t) = 0 \tag{2.43}$$

$$\boldsymbol{\sigma}_2(x, y, t) - \boldsymbol{\sigma}_1(x, y, t) = 0 \tag{2.44}$$

2.2.4.3 Rayleigh waves

An important surface wave is the Rayleigh-wave, seen in Figure 2.11. It is a combination of P- and S-waves and occur as waves travel along the surface of an elastic body (Olsson 1990). The effect of the Rayleigh-wave is highly concentrated at the surface and decreases significantly fast towards the depth of the material. The speed of the Rayleigh-wave is lower than that of the P- and S-wave (Rao 2007).

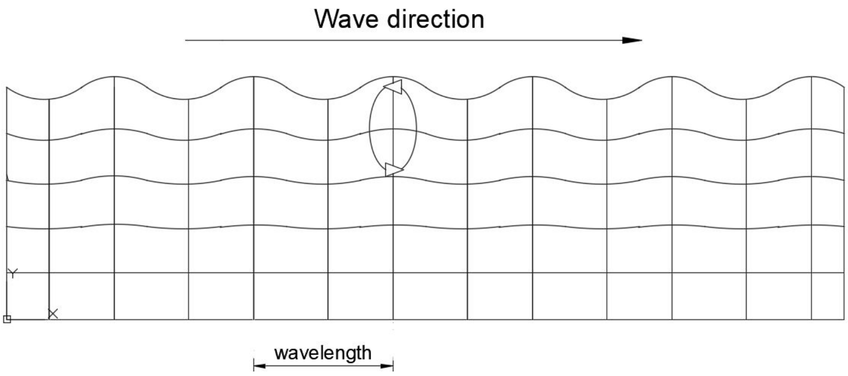

Figure 2.11: Rayleigh wave

According to Hagedorn (2007), the waveform given in equation 2.22 can, for a Rayleigh wave, be written as

$$\mathbf{u}(x, y, t) = (\mathbf{A}_\text{P} e^{k_P y} + \mathbf{A}_\text{S} e^{k_S y}) e^{i(kx - \omega t)} \tag{2.45}$$

where $\mathbf{A}_\text{P}$ and $\mathbf{A}_\text{S}$ are vectors representing the amplitude in the longitudinal and the transverse direction of the wave respectively. The amplitude of the Rayleigh wave is only excited in the two directions of the plane, x and y in Figure 2.11.

Hagedorn (2007) also describes the speed of the Rayleigh wave by

$$c_R = c_S \xi \tag{2.46}$$

where ξ is the root of

$$\xi^6 - 8\xi^4 + 8\left(3 - \frac{2}{\kappa^2}\right)\xi^2 - 16\left(1 - \frac{1}{\kappa^2}\right) = 0 \tag{2.47}$$

which satisfies the conditions of

$$\frac{\xi}{\kappa} - 1 \leq 0 \quad \text{and} \quad \xi - 1 \leq 0. \tag{2.48}$$

Another type of surface wave is known as the Love wave. However, similar to the SH-wave mentioned above, it is also an out-of-plane wave, and thus not further studied.

2.2.5 Damping

Waves propagating trough soil will undergo attenuation, which is gradual loss of amplitude of the waves as they propagate. The effect of attenuation is dependent on the geometrical- and material damping of the soil. The decrease in amplitude with regard to distance can be described as

$$A_2 = A_1\left(\frac{R_1}{R_2}\right)^n e^{-d_m(R_2-R_1)} \tag{2.49}$$

where A_1 and A_2 are the amplitudes, R_1 and R_2 are distance from the charge, n is the geometrical damping factor and d_m is the material damping factor (Dong-Soo & Jin-Sun 2000).

The effect of geometrical damping occurs in perfectly elastic materials. The geometrical damping factor can be described analytically as a function of the wave type, the distance from the vibration source and the source type. For a buried explosion, when the source is located in the ground, the geometrical damping factor is $n = 1.0$ (Dong-Soo & Jin-Sun 2000).

However, as described in Section 2.1.2, soil materials does not have a perfectly elastic material behaviour. Material damping will occur in the soil due to friction and cohesion between the material particles. Material damping is described as a function of the soil type and the frequency of the vibration as

$$d_m = \frac{\pi\eta f}{C_i} \tag{2.50}$$

where η is the loss factor, which describes the loss of energy during vibration, f is the frequency of the vibration and C_i is the wave speed. Thus the effect of material damping is frequency dependent damping and the amount of damping is also dependent on the wave type (Dong-Soo & Jin-Sun 2000).

In plastic clay, the material damping can be described by the material damping ratio, D_{clay}, which is dependent of the friction between soil particles, strain rate during deformation and non-linearity in the stress-strain relationship. The relationship between material damping ratio and strain amplitude, γ, gives three different damping ranges, where the soil behaviour acts differently, as seen in Figure 2.12. At shear strain amplitudes below $\gamma = 0.001\%$ there is a linear elastic material behaviour, the damping ratio in this region is constant and minimum. In the region $0.001 < \gamma < 0.01\%$ there is a nonlinear elastic material behaviour, the material damping ratio increases in this region. If the strain amplitude exceeds $\gamma = 0.01\%$ the material is in the plastic range where the material damping increases even further (Darendeli 2001).

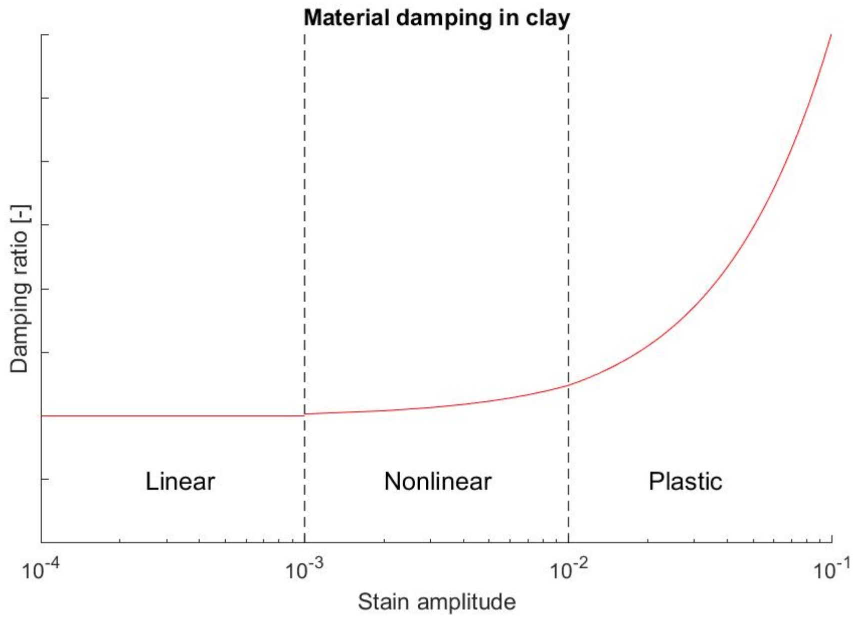

Figure 2.12: Material damping in clay, the ranges are divided by the dashed lines.

In addition to the effect from shear strain amplitude, the material damping ratio is also affected of by the confining pressure, i.e. the mean effective stress. The damping ratio becomes more linear when the level of confining pressure is increased. It is also affected by consolidation, the amount of load cycles, the loading frequency and the soil type (Darendeli 2001).

In rock, the damping is heavily influenced by joints in the rock mass. The joints can be divided into two categories; frictional and filled. In frictional joints, there is no material between the cracked surfaces, thus the wave propagates across the crack in friction. However, in filled joints there is material between the cracked surfaces, which have a large influence on the damping as they damp more effectively than the frictional joints. Furthermore, the damping is also influenced by the orientation of the joints. In particular, the S-wave will attenuate faster than the P-wave due to its dependency on the joint orientation. The damping effect from the joint orientation is decreased by the influence of confining pressure (Sebastian 2015). The presence of discontinuities in the rock has a damping effect on the higher frequencies of the shock wave coming from the blast. Therefore as the shock wave propagates and reaches the surface, the frequency content will mostly contain low frequencies (Yang

J et. al 2016).

A convenient and common way to model damping in FE analysis is by means of Rayleigh damping. Rayleigh damping is a frequency dependent damping method which takes into account of the mass and stiffness of the soil structure. A damping curve is determined by combining the effect of damping by stiffness and mass given by choosing appropriate frequencies f_1 and f_2 together with relative damping ratios ζ_1 and ζ_2 where

$$\frac{f_1}{f_2} < \frac{\zeta_2}{\zeta_1} < \frac{f_2}{f_1}. \tag{2.51}$$

In a simple one dimensional case of Rayleigh damping the relation between mass, stiffness and damping is determined by

$$C = aM + bK \tag{2.52}$$

where C, M and K is the damping, mass and stiffness coefficients, and a and b constants dependent on the soil structure. The constants a and b is related to the chosen frequencies and relative damping ratios according to

$$a = 4\pi f_1 f_2 \frac{\zeta_1 f_2 - \zeta_2 f_1}{f_2^2 - f_1^2} \tag{2.53}$$

$$b = \frac{\zeta_2 f_2 - \zeta_1 f_1}{\pi(f_2^2 - f_1^2)}. \tag{2.54}$$

The damping ratio, D, for each frequency, f, is determined as

$$D = \frac{1}{2}\left(\frac{a}{f2\pi} + bf2\pi\right). \tag{2.55}$$

Thus, by using Rayleigh damping, it is possible to choose an appropriate damping ratio for each material in the soil structure (Sheng-Huoo & Shen-Haw 2007).

For example, see Figure 2.13, the damping curve is generated given the frequencies $f_1 = 200$ Hz and $f_2 = 2000$ Hz and the relative damping ratios $\zeta_1 = \zeta_2 = 0.05$. The red and green curves in Figure 2.13 represents the damping effect from the stiffness and mass of structure respectively, the summation of the damping effect of mass and stiffness gives the Rayleigh damping curve represented by the blue curve.

In a study by Bos & Slawinski (2010), a wave front is described as a characteristic hypersurface using elastodynamic equations. The speed of a wave front is not determined by the damping, since the damping terms contain only lower order derivatives.

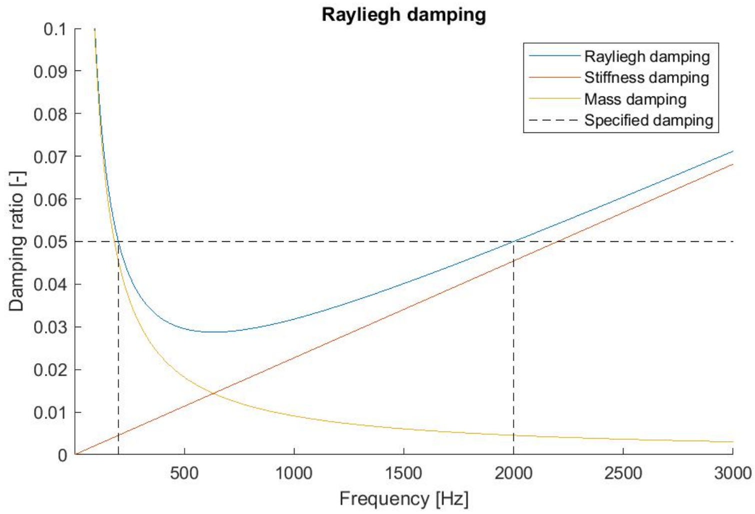

Figure 2.13: Rayliegh damping based on frequencies $f_1 = 200$ Hz and $f_2 = 2000$ Hz and relative damping ratios $\zeta_1 = \zeta_2 = 0.05$

2.3 Poroelastic wave propagation

As stated in Section 2.1.3, a fluid inside a porous material will influence the material behaviour. When stresses are applied to the material the fluid will cause pressures inside the material. The fluid will then flow in the direction where the pressure is lower. Compared to elastic wave propagation, poroelastic wave propagation uses two additional variables. The first variable is the pore pressure which describes the pressure in the material from the fluid inside. The other variable is the variation in fluid content that describes the change of fluid volume per volume of solid frame (Wang 2000).

By expanding elastic wave propagation to poroelastic wave propagation through introduction of Darcy's law, a second P-wave is observed. The second P-wave, commonly expressed as the P2-wave is a slow out of phase wave which is highly attenuated. According to Biot's theory of wave propagation, there are two frequency regions which separate the governing parameters in poroelastic wave propagation. The critical frequency is given as

$$\omega_{\mathrm{crit}} = \frac{\mu\phi}{\alpha_\infty \kappa \rho_{\mathrm{f}}} \tag{2.56}$$

where μ is the dynamic viscosity, ϕ is the porosity, α_∞ is the tortuosity factor, κ is the permeability and ρ_{f} is the density of the fluid (Kudarova 2016). The tortousity of a material is the path that a fluid takes when passing through a media divided by the length of the medium (Pisani 2011). According to Chertkov & Ravina (1993), the tortuosity of clay's are in the region of $1.4 - 3.25$.

In the frequency region below frequencies below ω_{crit}, there is no P2-wave and the wave propagation is governed by viscous forces between the solid and fluid phases.

However, in the frequency region above ω_{crit} both P1- and P2-waves propagate through the material. The P2-wave is heavily dependent on the tortuosity. The frequency range for vibrations in soil is often much lower than ω_{crit}, thus it is unlikely that the P2-wave is observed in the velocity response of the vibration (Kudarova 2016).

2.3.1 Constitutive equations

In the linear model, six constitutive equations are used, one for each direction of space, Equation 2.13, and three for the shear directions, Equation 2.14. In poroelasticity, a seventh equation is added, describing the fluid's flow and pressure. Since the pore pressure is acting equally in all three directions, the pore pressure is included in the directional equations

$$\sigma_{ii} = \lambda\Delta + 2\mu\varepsilon_{ii} - \alpha p \qquad \not\Sigma_{ii} \tag{2.57}$$

$$\sigma_{ij} = \mu\varepsilon_{ij} \quad \text{where} \quad i \neq j \tag{2.58}$$

$$p = M(\xi_f - \alpha\varepsilon) \tag{2.59}$$

where p and ξ_f are the variables, pore pressure and the variation of fluid flow respectively. The constants α and M are the Biot-Willis coefficient and the inverse constrained storage coefficient respectively (Wang 2000).

2.3.2 Differential equations

Instead of describing the displacements in the body with one displacement field, as done in Section 2.2.1, the displacement in the poroelastic body will be done with two fields. One field describes the solid displacement, u, and one describes the displacement in the fluid, U. The relation of the displacement fields is written as (Cheng 2016)

$$w = \phi(U - u). \tag{2.60}$$

In order to determine the differential equations, an equilibrium equation using Newton's second law is adopted. The same principle as in Equation 2.10 is used, but with the extra displacement field. The equilibrium equation in one direction, x, can then be written as

$$\frac{\partial \sigma_{xx}}{\partial x} + \frac{\partial \sigma_{xy}}{\partial y} + \frac{\partial \sigma_{xz}}{\partial z} = \rho \frac{\partial^2 u_x}{\partial t^2} + \rho_f \frac{\partial^2 w_x}{\partial t^2} \tag{2.61}$$

where ρ_f is the density of the fluid.

The flow of the fluid in the body is described by Darcy's law with inertia effects

$$\frac{\partial w_x}{\partial t} = -\kappa\Big(p + \rho_f \frac{\partial^2 u_x}{\partial t^2} + \rho' \frac{\partial^2 w_x}{\partial t^2}\Big) \tag{2.62}$$

where κ is the permeability and ρ' can be written as $\frac{\rho_f}{\phi}$ or as $\frac{\rho_f}{\phi} + \frac{\rho_a}{\phi^2}$, where ρ_a is apparent added density and depends on the tortuosity in the material (Chen 1994).

Inserting the constitutive relations from Equations 2.57, 2.58 and 2.59 in 2.61 and 2.62, the governing equation in the time domain can be written for all directions as

$$\mu\nabla\mathbf{u} + (\lambda+\mu)\nabla(\nabla\cdot\mathbf{u}) + \alpha M\nabla(\nabla\cdot\mathbf{w}) = \rho\ddot{\mathbf{u}} + \rho_{\mathrm{f}}\ddot{\mathbf{w}} \tag{2.63}$$

$$\alpha M\nabla(\nabla\cdot\mathbf{u}) + M\nabla(\nabla\cdot\mathbf{w}) - \frac{1}{\kappa}\mathbf{w} = \rho_{\mathrm{f}}\ddot{\mathbf{u}} + \rho'\ddot{\mathbf{w}} \tag{2.64}$$

By applying the divergence criteria in Equation 2.23 on 2.63 and 2.64 it is possible to write the coupled equation system as

$$\nabla\nabla\cdot\begin{pmatrix}\lambda+2\mu & \alpha M\\ \alpha M & M\end{pmatrix}\begin{pmatrix}\mathbf{u}\\ \mathbf{w}\end{pmatrix} = \begin{pmatrix}\rho & \rho_f\\ \rho_f & \rho'\end{pmatrix}\begin{pmatrix}\ddot{\mathbf{u}}\\ \ddot{\mathbf{w}}\end{pmatrix} + \begin{pmatrix}0 & 0\\ 0 & \frac{1}{\kappa}\end{pmatrix}\begin{pmatrix}\dot{\mathbf{u}}\\ \dot{\mathbf{w}}\end{pmatrix} \tag{2.65}$$

or as

$$\nabla\nabla\cdot(\mathbf{K}_P\mathbf{U}) = \mathbf{M}_P\ddot{\mathbf{U}} + \mathbf{C}_P\dot{\mathbf{U}} \tag{2.66}$$

where

$$\mathbf{K}_P = \begin{pmatrix}\lambda_u+2\mu & \alpha M\\ \alpha M & M\end{pmatrix} \tag{2.67}$$

$$\mathbf{M}_P = \begin{pmatrix}\rho & \rho_f\\ \rho_f & \rho'\end{pmatrix} \tag{2.68}$$

$$\mathbf{C}_P = \begin{pmatrix}0 & 0\\ 0 & \frac{1}{\kappa}\end{pmatrix} \tag{2.69}$$

$$\mathbf{U} = \begin{pmatrix}\mathbf{u}\\ \mathbf{w}\end{pmatrix}. \tag{2.70}$$

In order to describe the poroelastic wave equations in the same manner as the elastic wave Equations 2.25 and 2.26, Equation 2.66 is multiplied from the left with the inverted poroelastic mass matrix $\mathbf{M}_P$. A matrix $\mathbf{P}_P$, containing the eigenvectors of $\mathbf{M}_P^{-1}\mathbf{K}_P$ is then introduced in order to diagonalize $\mathbf{M}_P^{-1}\mathbf{K}_P$. The inverse of $\mathbf{P}_P$ is multiplied from the right and $\mathbf{P}_P$ is multiplied from the left, as

$$\begin{gathered}\nabla\nabla\cdot(\mathbf{M}_P^{-1}\mathbf{K}_P\mathbf{U}) = \ddot{\mathbf{U}} + \mathbf{M}_P^{-1}\mathbf{C}_P\dot{\mathbf{U}}\\ \mathbf{P}_P^{-1}(\mathbf{M}_P^{-1}\mathbf{K}_P)\mathbf{P}_P = \begin{pmatrix}c_{p1}^2 & 0\\ 0 & c_{p2}^2\end{pmatrix}.\end{gathered} \tag{2.71}$$

The displacement fields $\mathbf{U}$ can then be written as

$$\mathbf{W}_P = \mathbf{P}_P^{-1}\mathbf{U} \tag{2.72}$$

and the system in Equation 2.66 can be expressed as

$$\begin{pmatrix} c_{P1}^2 & 0 \\ 0 & c_{P2}^2 \end{pmatrix} \nabla(\nabla \cdot \mathbf{W}_P) = \ddot{\mathbf{W}}_P + (\mathbf{P}_P^{-1}\mathbf{M}_P^{-1}\mathbf{C}_P\mathbf{P}_P)\dot{\mathbf{W}}_P. \tag{2.73}$$

The poroelastic S-wave can be expressed in the same way by applying the curl criteria in Equation 2.23 on Equations 2.63 and 2.64. As shear waves cannot propagate in fluid material, there is only one poroelastic S-wave.

$$-\nabla\nabla \times \begin{pmatrix} G & 0 \\ 0 & 0 \end{pmatrix} \begin{pmatrix} \mathbf{u} \\ \mathbf{w} \end{pmatrix} = \begin{pmatrix} \rho & \rho_f \\ \rho_f & \rho' \end{pmatrix} \begin{pmatrix} \ddot{\mathbf{u}} \\ \ddot{\mathbf{w}} \end{pmatrix} + \begin{pmatrix} 0 & 0 \\ 0 & \frac{1}{\kappa} \end{pmatrix} \begin{pmatrix} \dot{\mathbf{u}} \\ \dot{\mathbf{w}} \end{pmatrix}. \tag{2.74}$$

Following the same procedure as with the P-waves, it is possible to express Equation 2.74 as

$$-\begin{pmatrix} c_S^2 & 0 \\ 0 & 0 \end{pmatrix} \nabla(\nabla \times \mathbf{W}_S) = \ddot{\mathbf{W}}_S + (\mathbf{P}_S^{-1}\mathbf{M}_P^{-1}\mathbf{C}_P\mathbf{P}_S)\dot{\mathbf{W}}_S. \tag{2.75}$$

The intrinsic poroelastic damping matrix, $\mathbf{C}_\mathrm{P}$, does not affect the wave speed of the poroelastic waves and should be distinguished from the Rayleigh damping mentioned in Sections 2.2.5.

2.3.3 Poroelastic boundary conditions

When the poroelastic waves reach a material interface, it will reflect back to the material and refract through the interface into the other material. When an incident P-wave in an elastic material reaches the boundary between an elastic and a poroelastic material, it will generate a reflected P-wave, reflectes S-wave, refracted P1- and P2-waves and a refracted S-wave (Bouzidi & Schmitt 2009).

The poroelastic waves will give rise to poroelastic Rayleigh waves at the free surface. One Rayleigh wave will be generated as a combination of the P1-wave and the S-wave, another Rayleigh wave will be created from the P2-wave and the S-wave. These surface waves are referred to as R1- and R2-waves. The R1-wave is heavily dependent on the permeability at the soil surface and share similarities with the elastic Rayleigh wave. The R2-wave however, only exists for impermeable and partially permeable materials and is like the P2-wave, heavily dependent on the tortousity of the porous medium (Yu et al. 2012).

2.4 Blasting

A detonation blast is a very fast process that generates high temperatures and high density gases, measured in VoD, velocity of detonation and pressure. The velocity of detonation describes the speed of the wavefront as it propagate through the explosive (Persson et al. 1993). The detonation process consists of two distinct phenomena, firstly a shock wave, secondly a high pressure gas.

Studies has been done in order to separate the effect from the shock wave and the effect from the high pressured gas. The initial shock wave fractures the rock creating micro- and macro cracks which forms a crack pattern. The high pressured gas flows into the crack pattern and expands the cracks (Lanari & Fakhimi 2011). The shock wave propagates through the soil as P-, S- and, at the surface, as Rayleigh waves (Ainalis, D et al 2016).

The effect of attenuation generates the possibility to divide the soil and rock affected by the blast into two regions. The first region, defined as the near-blast region, is where the rock is subjected to plastic deformations from shearing, crushing and fragmentation. The plastic deformations in this region is not further treated, as specified in Chapter 1. The second region is defined as the far-field region, where the blast causes no permanent damage to the soil and rock. The effect from the blast in the far-field region are ground vibrations which, if they are large, can affect structures negatively (Ainalis, D et al 2016). A study on the frequency spectrum of blasting induced vibration by Y. Chenglong & Han (2018) shows how the shape of the wave changes form as it travels from the near field to the far field. In the near field, the wave has a large positive amplitude, followed by a significantly smaller negative amplitude. However, when in the far field, the positive and negative amplitudes has the same magnitude.

There are many factors that influence the ground vibration in the far-field. The most significant factors are charge weight, delay interval between blast rounds, the blast hole confinement, which describes how well the blast hole is covered and the distance between the charge and the measurement point. Furthermore, the ground vibration is influenced by the type of explosive and the type and amount of material overburdening the blast. The range of frequencies in vibrations from blasting is 1-300 Hz (Ainalis, D et al 2016).

When blasting for tunnels, a sequenced method of several smaller blasting rounds is used. The duration of a blasting round is chosen dependent on the situation and can last up to 10-15 seconds. The sum of all charges gives the total charge load. However as tunnel blasting consists of smaller loads that each creates separate blasting waves, the total charge load is not the governing charge load. The governing charge load is the co-operative charge load, which is often defined as the largest charge in the interval (Hall 2013).

2.4.1 Methods of prediction

According to Khandelwal & Saadat (2015), blasting induced ground vibration has been historically predicted analytically by methods of regression analysis made from vibration data from test measurements at the blasting site. An empirically found expression, called a scaling law. It is based on the distance between the charge load, the point of measurement, R, and the co-operative charge load, Q and is used in order to predict a value for the peak particle velocity, PPV. The equation is given as

$$PPV = K\left(\sqrt{\frac{Q}{R^{2/3}}}\right)^{B}. \tag{2.76}$$

As Equation 2.76 are significantly dependent on the geographical location of the blasting site, the test measurement are highly important (Hall 2013). When a sufficient amount of test blasting is done, the empirical constants K and B can be determined and the charge load can be increased by means of regression analysis. However, if the site geology is inconsistent, the measured data will scatter and the regression analysis will become unpredictable (Persson et al. 1993).

Various scaling laws have been used to predict the PPV from blast vibration internationally, also dependent on the maximum charge and the distance between the blast and the point of measurement. International scaling laws are presented in Table 2.3 (Khandelwal & Saadat 2015).

Table 2.3: International scaling laws.

Scaling law	**Equation for** PPV [mm/s]
United States Bureau of Mines (1962)	$PPV = K(R/\sqrt{Q})^{-B}$
Ambraseys-Hendon (1968)	$PPV = K(R/Q^{1/3})^{-B}$
Bureau of Indian Standards	$PPV = K(R^{2/3}/Q)^{-B}$

Since there are difficulties predicting the PPV using these formulas, research into development of reliable scaling laws has been done. For example, through inclusion of more parameters such as powder factor, which is the amount of explosive needed to fracture one ton of rock, blastability index, which is the ratio between the compressive and the tensile strength of the rock. The modulus of elasticity of the rock, the spacing of the explosives, the burden of explosives, which is the distance from the charge to closest free surface, the charge length and the hole depth were also included (Khandelwal & Saadat 2015).

2.4.2 Blasting models

Today a large emphasis has been put on the possibility to model blasting numerically using computers. Due to the immense pressure and temperatures generated at detonation, there are significant difficulties to do experimental measurements on blast holes. The pressure is instead predicted through empirical formulas or detonation theories. A blasting model needs to account for the blast hole wall pressure, which is the pressure at the face of the rock, coming from the explosion and its time dependency (Ainalis, D et al 2016).

One of the most common ways to describe the blast hole wall pressure from an explosive can be expressed with an Equation of State, EoS. An EoS is a thermodynamic or constitutive equation between two or more state functions dependent on temperature, pressure, volume or internal energy (Sazid & Singh 2013). The John-Wilkins-Lee Equation of State, JWL EoS is a function that describes the blast hole wall pressure

$$P_b = A_b(1 - \frac{\omega_{jwl}}{R_1 V})e^{-R_1 V} + B_b(1 - \frac{\omega_{jwl}}{R_2 V})e^{-R_2 V} + \frac{\omega_{jwl} e_s}{V} \tag{2.77}$$

where V is the specific volume, e_s is the specific energy, ω_{jwl}, A_b, B_b, R_1 and R_2 are constants dependent on the explosive material.

However, a simpler yet very efficient way of expressing blast hole wall pressure is

$$P_b = \rho_b \frac{D_e^2}{8} \left(\frac{d_e}{d_h} \right)^3 \tag{2.78}$$

where ρ_b is the density of the explosive material, D_e is the velocity of detonation, d_e the diameter of the explosive material, and d_h is the blast hole diameter (Xia, X et al. 2018).

In addition to the blast hole wall pressure, a blasting model describes the time dependency of the blast. The rise and fall process of the pressure can be described by mathematical pressure-decay functions, which are widely used for modeling blasting analysis, and can provide a realistic picture of the blast hole pressure time history (Ainalis, D et al 2016). A pressure-decay function described by Xia, X et al. (2018), which represents a pulse function, see Figure 2.14, can be used in order to generate the wave coming from the explosive charge.

$$P(t) = 4P_b(e^{-\beta_r t/\sqrt{2}} - e^{-\sqrt{2}\beta_r t}), \qquad \beta_r = \sqrt{2} ln(2)/t_r \tag{2.79}$$

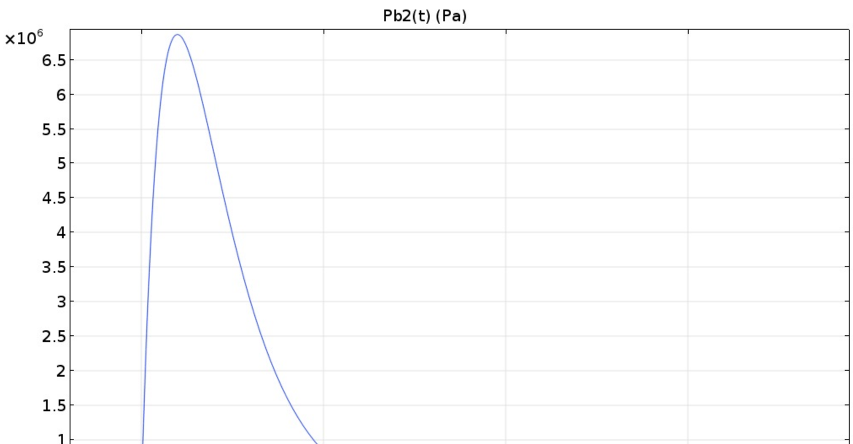

Figure 2.14: Pressure-decay function.

where P_b is the blast hole wall pressure as described above, β_r is a damping factor dependent on the rising time t_r of the blast hole wall pressure.

The rising time t_r of the blast hole wall pressure is dependent on the type of explosive material used, the blast hole length, the level of confinement and the type of rock which is affected by the blast. A study by Yang J et. al (2016) shows a frequency response dependency related to the rising time t_r. A low rising time yields a broad frequency spectrum with high frequencies, whereas high rising times results in a narrow spectrum with more low frequencies. However, the dominant frequency is unaffected by a change of rising time. The rising times used in the study by Yang J et. al (2016) vary between $0.8 \leq t_r \leq 3.2$ ms.

2.5 Standards

Standardization of procedures is done in order to establish a consensus between different groups of interest on how repeated problems should be tackled. Generally the aims when creating a standard is to define guidelines on consistent function and quality, increasing the efficiency of processes, having more transparency, improving the conditions for safety and accessibility, lower the environmental impact by conserving resources and to promote development (Swedish Standards Instiute n.d).

The methods of standardization for guidance levels for vibrations on buildings from blasting can be divided into two types. The first type gives guidance levels of peak particle velocity, PPV, based on distance and the soil type under the building. Standards of establishing guidance levels based on distance and soil type is only used in Sweden, Finland and Estonia. However, buildings are generally more susceptible to damage due to vibrations at low frequencies as there is an increased risk of resonance. Thus, the second and most common way of standardization is by relating the guidance levels of PPV to the frequency of the vibration (Jern, M. et al. 2013).

There are other differences between the methods of standardizations, for example, the guidance levels set by the Swedish Standard accounts only for vertical PPV, whereas in most international standards a triaxial PPV is accounted for. Another difference is how induced vibrations are measured. In Sweden the measurements are done at the foundation of the building, whereas in Germany inside the building at the bottom floor (Jern, M. et al. 2013).

2.5.1 Swedish standard

The Swedish standard for blasting induced vibration is used in order to obtain guidance levels for vertical PPV. By determining the maximum PPV it is possible to evaluate the risk for damage on adjacent constructions generated by blasting operations (Swedish Standard Institute 2011). The PPV is defined as the velocity that a particle moves around a point of equilibrium (Wersäll, C. et al. 2009).

The guidance levels are calculated for nearby buildings that may be affected by the blasting induced vibrations. The standard cannot be applied directly on slender constructions such as skyscrapers and certain bridge supports, neither is it suitably for risk calculations on underground facilities and pipes. The standard does not account for the effect of vibration on humans. The guidance levels refers to the maximum value of the PPV (Swedish Standard Institute 2011).

The guidelines for choosing the maximum levels for PPV is based on the book *The Modern Technique of Rock Blasting* by Langefors and Kihlström (Thelin 2009). The risk of damage from vibration in a wall section is calculated empirically based on possible ways of deformation. The wall was studied with regard to compression and elongation, shearing and bending. On top of the deformation certain stationary loads were superponed on the wall in order to have a real like scenario. The governing factors for the vibration occurring in the wall are the natural frequency, the frequency of the imposed vibration, the wall height and material parameters such as modulus of elasticity and density. The damage criteria as a function of the above mentioned governing factors can be expressed as a function of amplitude and frequency. The damage is proportional to the relative velocity, which is defined as the ratio between the vibration velocity in the wall and the wave speed in the ground, for a certain frequency interval of $40 - 500$ Hz. Four categories of damage are determined; no noticeable cracks, insignificant cracking, cracking and major cracks. Through the damage criteria is was possible to determine the vibration velocities needed for damage to occur, as seen in Figure 2.15. Langefors and Kihlström determined the guidance levels for rock through experiments (Langefors 1978).

The guidance levels according to the Swedish Standard for blasting induced vibrations is calculated as

$$v = v_0 \cdot F_b \cdot F_m \cdot F_d \cdot F_t \tag{2.80}$$

where v_0 is the uncorrected velocity dependent on the soil or rock properties directly below the building, F_b is the building factor which accounts for the vibration sensitivity. F_m is dependent on the material, F_d on the distance between the charge and the building and F_t is a factor that is dependent on the duration of blasting work (Swedish Standard Institute 2011).

The uncorrected PPV, v_0 which can be chosen from three values dependent on soil material, is based on the research by Langefors and Kihlström which was described above. The values for Scandinavian bedrock and soils is given in Table 2.4.

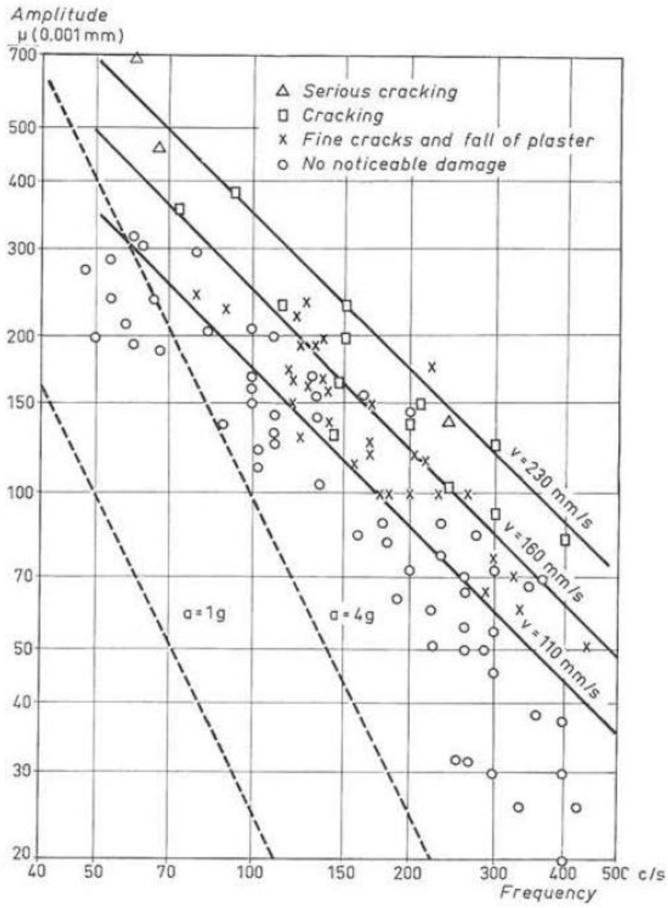

Figure 2.15: Connection between amplitude, frequency and damage (Langefors 1978).

Table 2.4: Uncorrected PPV.

Overburden material	Uncorrected PPV, $\mathbf{v_0}$ [mm/s]
Clay	18
Moraine and sand	35
Rock	70

The uncorrected PPV in mm/s is related to the P-wave propagation speed, c_P in m/s using Equation 2.81 (Persson et al. 1993)

$$v_0 = \frac{c_P}{65} \tag{2.81}$$

The building factor F_b is given in five classes ranging from 1.7 for heavy constructions such as bridges and docks, to particularly sensitive historic buildings with a value of $F_b < 0.5$. The material factor F_m accounts for the sensitivity of the material in building. There are four classes ranging from the strong materials such as reinforced concrete, steel and timber with $F_b = 1.20$ to calcium silicate bricks with $F_b = 0.65$. The distance factor is dependent on the shortest distance between the charge and the measurement point on the building. It is calculated using the following Equations (Swedish Standard Institute 2011)

$$F_d = 1.91d^{-0.28} \qquad d \leq 10\text{m} \tag{2.82}$$

$$F_d = 1.56d^{-0.19} \qquad d > 10\text{m}, \text{for clays} \tag{2.83}$$

$$F_d = 1.91d^{-0.29} \qquad d > 10\text{m}, \text{for moraine and sand} \tag{2.84}$$

$$F_d = 2.57d^{-0.42} \qquad d > 10\text{m}, \text{for rock} \tag{2.85}$$

if the distance is above $d = 350$ m the values become constant since the Rayleigh wave is considered as dominant for distances above 350 m (Jern, M. et al. 2013). The constant value for clay at $d > 350$ m is chosen as $F_d = 0.5$, for moraine as $F_d = 0.35$ and for rock as $F_d = 0.22$, as seen in Figure 2.16. With distances less than 10 m it is also necessary to investigate the vibrations more thoroughly.

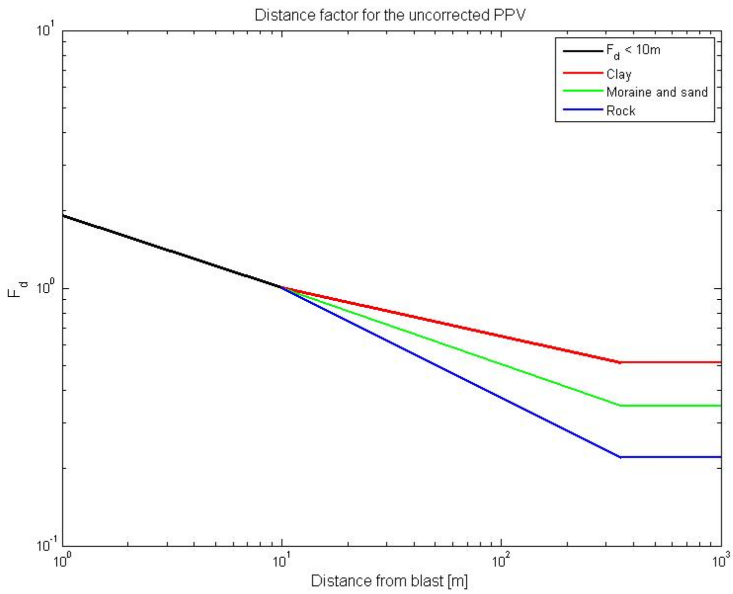

Figure 2.16: Distance factor according to SS 4604866:2011

The function factor F_t accounts for the duration of the blasting activities. It is chosen as $F_t = 1.0$ for tunnels and foundations and $1.0 < f_t < 0.75$ for quarries and mines (Swedish Standard Institute 2011).

2.5.2 Frequency based standards

As mentioned in Section 2.5, the most common way to determine guidance levels for PPV for blasting operations is by means of frequency based standards. As constructions are more susceptible to damage at lower frequencies due to the effect of resonance, the guidance levels set according to frequency based standards restricts the tolerance at lower frequencies. Similarly to the Swedish Standard based on distance and overburden, the frequency based standards are often dependent on the type of building, the historical value and the material properties. However, the dependency is not given as factors in the same manner as in the Swedish Standard. The most restrictive guidance levels are set in the frequency range of $1 \leq f \leq 10$ Hz, where the guidance levels for PPV are set around 10 mm/s. (Jern, M. et al. 2013).

The frequency based standard used in the USA is also based on empirical research. Through a collection of measurements on existing buildings with a categorization of major and minor structural damage as well as cosmetic damage it was possible to establish guidelines between PPV and frequency. However, compared to the Swedish Standard, no distance factor is applied (D.E. Siskind et. al 1980). The guidance levels for regular buildings according to the US standard is seen in Figure 2.17.

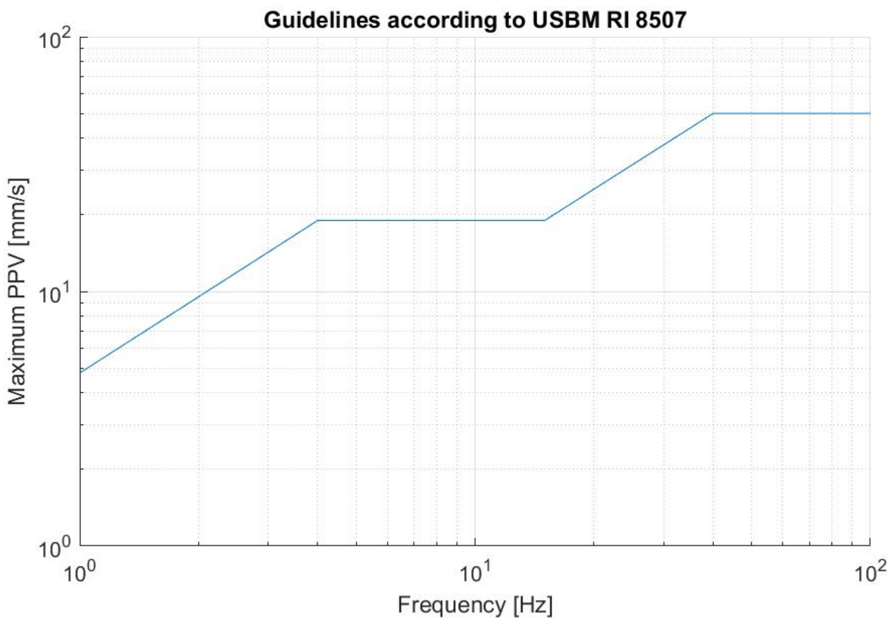

Figure 2.17: US frequency based standard for regular buildings.

The vibration at the surface will be in a certain frequency interval. In frequency based standards it is important to relate the measured maximum PPV to a certain frequency, however, the maximum PPV is not necessarily related to the dominating frequency. The German standard accounts for this by means of a frequency analysis in a short interval close to the maximum PPV (Jern, M. et al. 2013).

The regulations on blasting induced vibration is set differently in a lot of countries. For example in historical buildings which often have irreplaceable historic value, the limits are set as seen in Table 2.5 (Lu, W et al. 2012).

Table 2.5: International safety standards for peak pressure velocity in historic buildings

Country	**PPV** [mm/s]
America	12-25
China	1-5
England	7.5
France	2.5-7.5
Switzerland	3
Sweden	18
Germany	25
India	2 ($f < 8$) Hz
	5 ($8 < f < 25$) Hz
	10 ($f > 25$) Hz

3 FEM Implementation

This chapter will treat the finite element method that were used in this project. All FE modelling has been done in the computational FE program COMSOL Multiphysics. The chapter will cover the meshing and time stepping routines of the models as well as a convergence analysis and the boundary conditions that have been used.

As mentioned in Section 1.3, all models are made in two dimensions with plane stress conditions.

3.1 COMSOL Multiphysics

In order to create a model as close to reality as possible, COMSOL Multiphysics provide a modelling environment with varying physics modules. A module in COMSOL is a set of equations and a specific data input that represent a physical model. The modules in COMSOL vary from structural mechanics to electromagnetics and the physics of the modules can be coupled.

In this project, two sets of modules are used and combined. The first module is the structural mechanics module and is used for analyzing stress and strains in solid structures. The second module that is the Darcy's law module, which is used for calculating flow in porous structures. These modules combined give rise to a poroelastic module which is used in the project.

In order to describe the blasting induced vibrations in COMSOL Mulitphysics transient analyses is used. In order to express the vibrations in the frequency domain, a discrete Fourier transform function is applied on the time domain data using MATLAB.

3.2 Material models

The differential equation for the elastic material model used in COMSOL Muilti-physics is Equation 2.21. For the poroelastic material model in COMSOL, the displacement field for the fluid, $\mathbf{w}$, is replaced by pore pressure. This way, the equation system is reduced from 6 to 4 variables, which reduces the computation time.

A general expression for dynamics in FE is

$$\mathbf{M\ddot{u}} + \mathbf{C\dot{u}} + \mathbf{Ku} = \mathbf{F} \tag{3.1}$$

where **M**, **C** and **K** are the mass, damping and stiffness matrices respectively, **u** is the displacement vector and **F** is the force vector.

3.3 Time step

Since all models in this project are programmed to be time dependent, a time stepping scheme are determined. By default, COMSOL Multiphysics uses the generalized α method for structural and solid mechanics, which is also used for the models in this project. The generalized α method is an implicit time stepping scheme, and is calculated using the following equations: (Chung & Hulbert 1999)

$$\mathbf{\dot{u}}_{\mathrm{n+1}} = \mathbf{\dot{u}}_{\mathrm{n}} + \Delta \mathrm{t}\Big((1-\gamma)\mathbf{\ddot{u}}_{\mathrm{n}} + \gamma\mathbf{\ddot{u}}_{\mathrm{n+1}}\Big) \tag{3.2}$$

$$\mathbf{u}_{\mathrm{n+1}} = \mathbf{u}_{\mathrm{n}} + \Delta \mathrm{t}\mathbf{\dot{u}}_{\mathrm{n}} + \frac{\Delta \mathrm{t}^2}{2}\Big((1-2\beta)\mathbf{\ddot{u}}_{\mathrm{n}} + 2\beta\mathbf{\ddot{u}}_{\mathrm{n+1}}\Big) \tag{3.3}$$

where Δt is the chosen time step, and both γ and β are algorithmic constants. Equation 3.1 is then solved for $\mathbf{\ddot{u}}_{\mathrm{n+1}}$ as

$$\begin{gathered}\mathbf{M}\Big((1-\alpha_{\mathrm{m}})\mathbf{\ddot{u}}_{\mathrm{n+1}} + \alpha_{\mathrm{m}}\mathbf{\ddot{u}}_{\mathrm{n}}\Big) + \mathbf{C}\Big((1-\alpha_{\mathrm{f}})\mathbf{\dot{u}}_{\mathrm{n+1}} + \alpha_{\mathrm{f}}\mathbf{\dot{u}_{n}}\Big) + \\ \mathbf{K}\Big((1-\alpha_{\mathrm{f}})\mathbf{u}_{\mathrm{n+1}} + \alpha_{\mathrm{f}}\mathbf{u}_{\mathrm{n}}\Big) = (1-\alpha_f)\mathbf{F}_{\mathrm{n1+1}} + \alpha_{\mathrm{f}}\mathbf{F}_{\mathrm{n}}\end{gathered} \tag{3.4}$$

where α_f and α_m are also algorithmic constants. The relationship between the algorithmic constants is set as (Chung & Hulbert 1999)

$$\gamma = \frac{1}{2} - \alpha_m + \alpha_f \qquad \beta = \frac{1}{4}(1-\alpha_m+\alpha_f)^2. \tag{3.5}$$

For the time scheme to be unconditionally stable the constants are set as $\alpha_m \leq \alpha_f \leq \frac{1}{2}$. The different values of α_m and α_f are used in order to control the amount of numerical dampening in the model (Chung & Hulbert 1999).

Haigh (2005) suggests that the time step should be chosen as at least one 20th of the time for the fastest wave to pass through the smallest element.

3.4 Mesh

The elements in the models are chosen as second order Lagrangian triangular elements. According to Haigh (2005), the element size of a 1D material should be chosen as one 10th of the wavelength and frequency of the fastest wave. Since the materials have different material properties, and the mesh size is dependent on the material properties, each material have it's own mesh size.

3.5 Convergence Analysis

A convergence analysis is performed in the purpose of determining the right amount of elements and time steps that is needed for each material domain, thus establishing stability and accuracy. The wavelength of the excitation is calculated according to Equation 2.8. The wave speedis chosen according to Equation 2.25.

The analysis is done by adding a parameter, N_{rock}, which control the size of the elements and keep the time step at 20 steps per element in the rock. As the clay has different material properties, another parameter N_{clay} is introduced in order to generate a mesh for the clay.

The equation used for the element length, l, is

$$l = \frac{\lambda}{N_i} \tag{3.6}$$

and the equation for the time step, Δt, is

$$\Delta t = \frac{1}{\max\{N_{\text{rock}}, N_{\text{clay}}\}20 f_{\max}} \tag{3.7}$$

where $f_{\max}$ is the maximum frequency of the wave, which is chosen iteratively from the numerical study. By continually increasing N, both the element size and the time step are decreased in the model until the output data of the model no longer has any significant change from the previous model. The convergence study for rock and clay are done with the geometries in Figure 3.1.

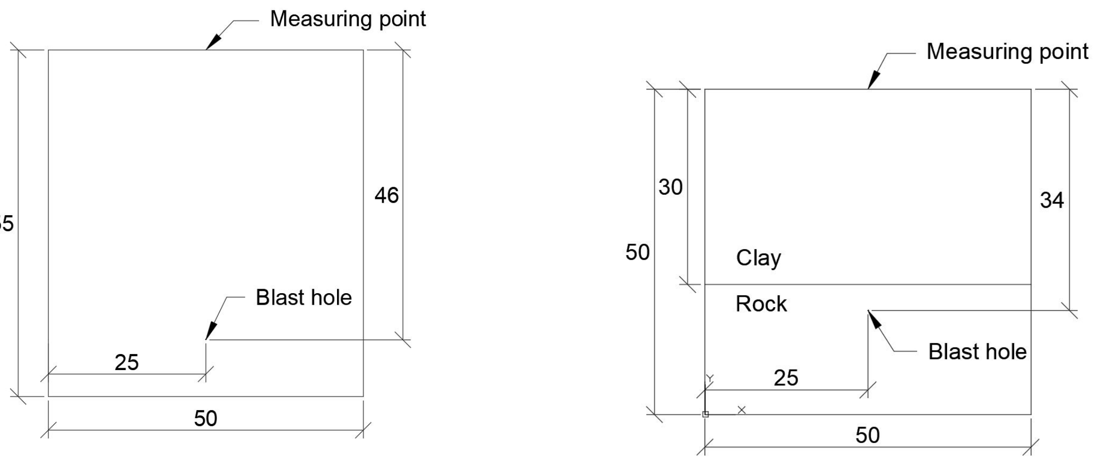

(a) Geometry used for the convergence study with a domain of rock.

(b) Geometry used for convergence with a soil profile of rock and clay.

Figure 3.1: Geometries used for convergence studies with different soil profiles.

3.6 Causality

A possible issue regarding frequency dependent damping is causality. According to the principle of causality, the response in a soil structure from an arbitrary external force, such as a blast, cannot appear before the wave reaches the measurement point. While using a frequency dependent damping method such as Rayleigh damping in a transient study, the time dependent vibrations are translated to the frequency domain, using a Fourier transform function. The vibrations are then damped in the frequency domain and translated back to the time domain using an inverse Fourier transform function. It is possible that the inverse Fourier transfer function introduces numerical problems in the model, which does not satisfy the principle of causality (Antes & Von Estorff 1987). The intrinsic damping in the poroelastic model is not affected by this, since it is not dependant on any frequencies.

It is not described how COMSOL Multiphysics employ the inverse Fourier transform function, thus it is possible that the response in the numerical model will not satisfy the principle of causality and predict the velocity-time response before the actual wave reaches the point of measurement.

Two models with the geometry of 30×30 m with material parameters of rock is created. The point of measurement is placed at a distance of 27.5 m from the blast. On of the model has no damping and a mesh of $N_{\text{rock}} = 20$. The other model is damped with Rayleigh damping, but with a mesh of $N_{\text{rock}} = 2$. The models are checked with regard to causality and compared with a calculation of the wave speed in rock.

3.7 Boundary conditions

In reality the soil can be regarded as infinite, however, in order to reduce the computational time a finite computational domain of smaller size was created, as seen in Figure 3.2. The computational domain should be able to describe the wave propagation in the same manner as the infinite media, thus the boundary conditions should be able to absorb the energy in the waves (Semblat 2015).

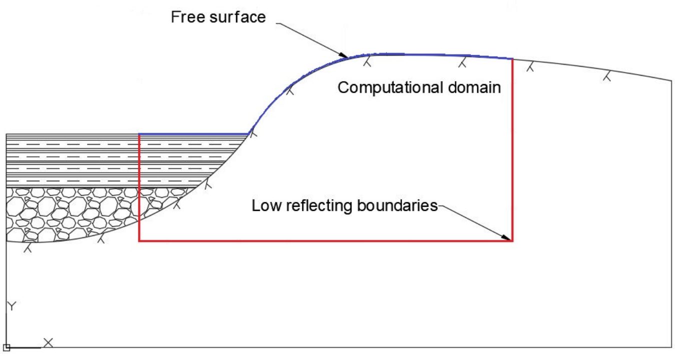

Figure 3.2: Computational domain and low reflecting boundary conditions.

In COMSOL, this was possible by using the Low-Reflecting Boundary Condition, LRBC. The LRBC is used in the transient analyses in order for the waves to refract from the finite computational domain by minimizing reflection at the boundaries. The material data from the domain in which the wave is propagating is used to generate a perfect impedance match for the P- and S-waves. Two adjacent materials with the same impedance will not cause any reflection, therefore the LRBC is maximizing the refraction and minimizing the reflection in the boundary. In COMSOL, the equation for LRBC is given as

$$\sigma\mathbf{n} = -\rho c_{\mathrm{P}}\left(\frac{\partial\mathbf{u}}{\partial\mathrm{t}}\mathbf{n}\right)\mathbf{n} + -\rho c_{\mathrm{S}}\left(\frac{\partial\mathbf{u}}{\partial\mathrm{t}}\mathbf{t}\right)\mathbf{t} \tag{3.8}$$

where $\mathbf{n}$ is the unit normal vector and $\mathbf{t}$ is the unit tangential vector (COMSOL Documentation n.d).

The soil surface is modeled in COMSOL as a free surface in order to describe the reflection at the surface.

The LRBC is a boundary condition in the solid mechanics module in COMSOL. When coupling the solid mechanics module with Darcy's law, the LRBC only affects the solid structure. However, there is no equivalent boundary condition for Darcy's law. All boundaries for the fluid phase is modeled as No Flow boundaries, such that no flow occurs at the free surface and in the inteface between the poroelastic rock and the elastic rock.

The load, P, in Equation 2.79 is applied in Pa on the boundary of the blast hole as an external stress, $\mathbf{F}$, in the normal direction of the boundary surface.

$$P\mathbf{n_s} = \mathbf{F} \tag{3.9}$$

where $\mathbf{n_s}$ is the normal to the surface.

4 Parametric Investigation

This chapter will treat the process of creating models that describe blasting induced vibration. Firstly, input data for the models are presented. Secondly, calibrations of the numerical models to the input data is presented. The calibrated models are then divided in the categories of geometric and material parameters. The models are all created in the program COMSOL Multiphysics.

4.1 Input data

In Appendix A, material data for two sections are presented which describe the soil conditions in Gothenburg. One describes the soil profile at Haga and the other at Korsvägen. The data are given by Markera Mark AB, a company working with the geotechnical situation during the construction of the Westlink tunnel.

The soil profile in both cases has the following order from the surface layer: disturbed fill material, highly plastic clay, moraine and bedrock. The phreactic surface level lies in the range $1 - 1.8$ m from the surface and the total depth of the soil to the bedrock varies from 1 m to 63 m.

The Young's modulus given in Appendix A is given as the secant Young's modulus, E_{50} as described in Section 2.1.2. Thus, a tangent Young's modulus is calculated based on the tangent shear modulus, G_0, according to Equation 2.5. In the linearized stiffness equation seen in Table 4.1, y is the distance from the soil surface. The linearized stiffness is a simplification in order to describe the stiffness in the soil profile.

A simplification is made, as no stiffness is given for the disturbed fill material, and no data is given that could describe what the disturbed fill material consisted of. Thus the disturbed fill material is excluded from the model.

The material stiffness parameters obtained from Markera Mark AB and parameters found in literature, are listed in Table 4.1.

Table 4.1: Typical material parameters in the study.

Parameter	**Rock**	**Clay**	**Unit**
Young's modulus	$60 \cdot 10^3$	$44204 + 4381y$	MPa
Poisson's ratio	0.25	0.495	-
Density	2600	1700	kg/m^2
Compressibility of fluid	-	$3.5 \cdot 10^{-10}$	1/Pa
Dynamic viscosity	-	$1.0518 \cdot 10^{-3}$	$\text{Pa} \cdot \text{s}$
Biot-Willis coefficient	-	1	-
Porosity	-	0.7	-
Permeability	-	10^{-10}	m^2

Measured velocity time response curves for varying overburden material types are obtained from Nitroconsult. The set of measured data comes from an underground tunnel construction project, for blasting in rock in urban areas. A response curve displays a sequence of several blasts within a time span of 6-10 seconds, as seen in Figure 4.1. All measurements obtained from Nitroconsult shows the velocity response at the ground surface. For a specific response curve the distance between the blast and the measurement point is given as well as the overburden type at the measurement point. The distance and overburden type corresponds to F_d and v_0 according to the measurement regulations in the Swedish Standard, see Section 2.5.1. In the data set obtained from Nitroconsult, there is no specific material properties given for the overburden type, neither are there any given soil profile. In Figures 4.1 and 4.2, velocity response curves for rock and clay are shown respectively.

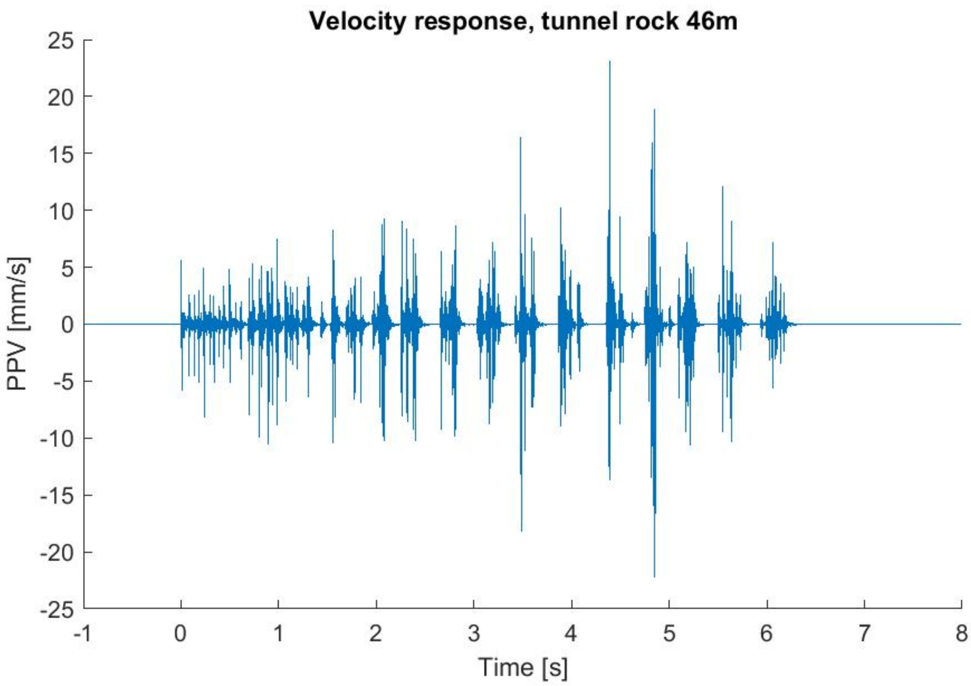

Figure 4.1: Velocity time response curve for blasting in rock at the distance of 46 m, obtained from Nitroconsult.

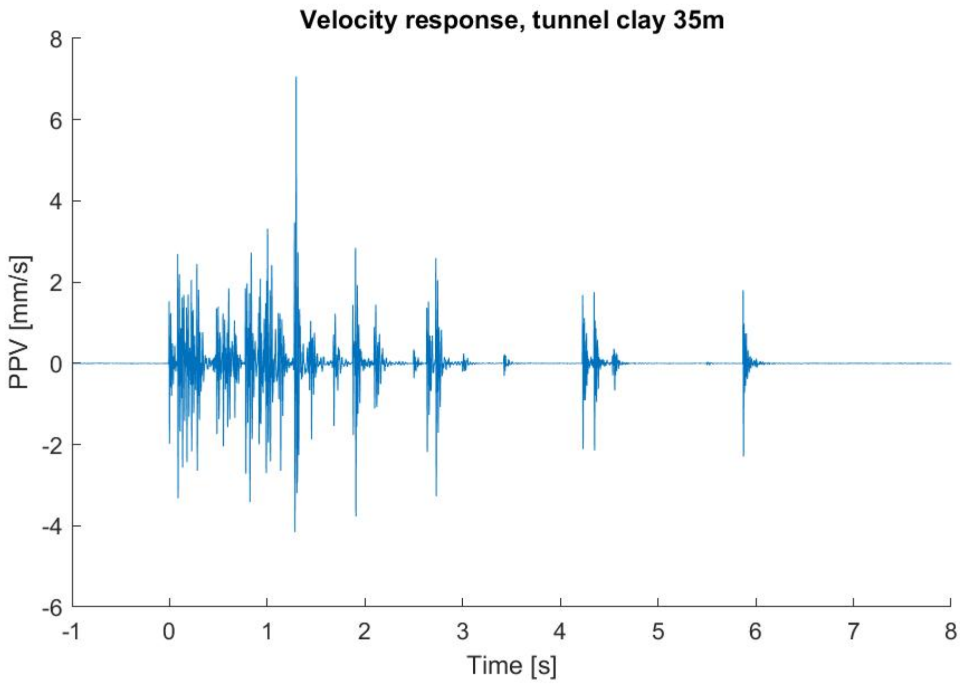

Figure 4.2: Velocity time response curve for blasting in rock at the distance of 35 m with overlaying clay, obtained from Nitroconsult.

4.2 Models

For every model, the result is dependent of the input data. The parameters that are used as input data for the models can have different importance for the result. Some of the parameters have a larger impact of the result than other parameters which will be investigated in the following section.

For each following example, a single parameter will be examined by letting it vary in several simulations. The results will include values for peak particle velocity as well as frequency spectra.

In order to validate the numerical models, the wave speeds are calculated using hand calculations. The elastic wave speeds are calculated using Equations 2.25, 2.26 and 2.46. The model is checked for interface waves by determining that Equations 2.41, 2.42 fulfills the boundary conditions given in Equations 2.43 and 2.44. Damping is not included in the wave speed calculations as described in Section 2.2.5. The poroelastic wave speeds are obtained using Equation 2.71. Furthermore, the critical Biot frequency is calculated using Equation 2.56.

For all models, the responses are measured at the ground surface since the guidance levels from the Swedish Standards are set as such. The measurement points for all models is also given in each respective model geometry.

When referring to a blast in rock and clay, the blast is localized in rock with an overburden of clay. The depth of the overburdening clay is given in each respective model geometry.

4.2.1 Calibration

In order to calibrate the models, a single blast from each blasting sequence in Figures 4.1 and 4.2 is studied. The single blasts with the least interference were chosen and the studied blasts for rock and clay respectively can be seen in Figures 4.3 and 4.4. The parameters in the blasting Equations 2.78 and 2.79 are chosen such that the velocity response curve from the numerical model is calibrated to the measured data for one blast. Rayleigh damping is applied in order to damp the higher frequencies caused by irregularities in the material, as described by Yang J et. al (2016).

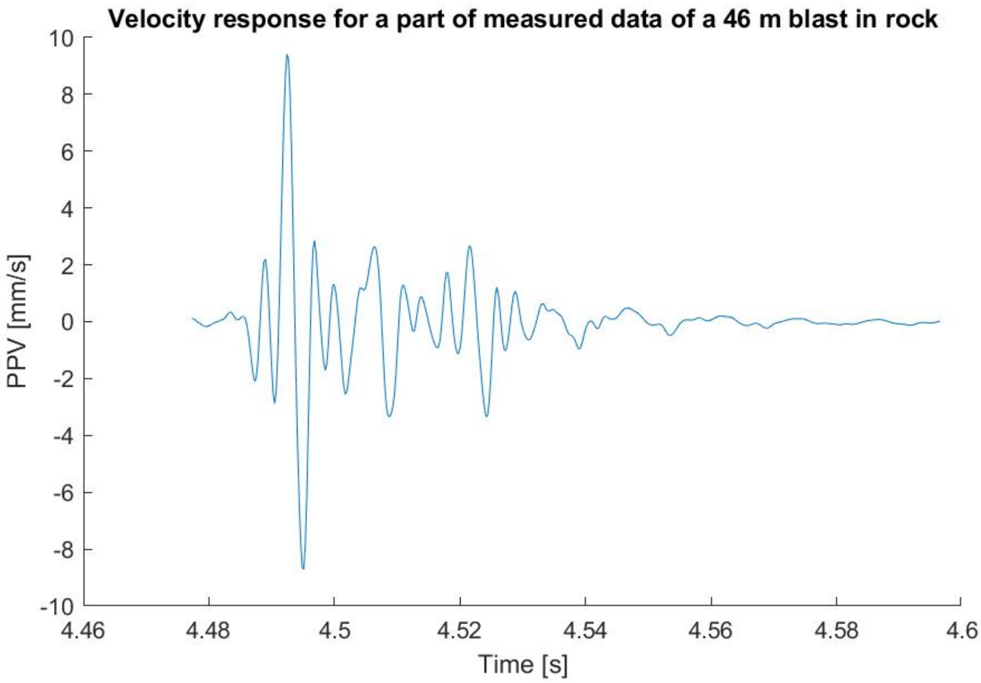

Figure 4.3: Velocity time response curve for one blast in rock at the distance of 46 m, obtained from Nitroconsult.

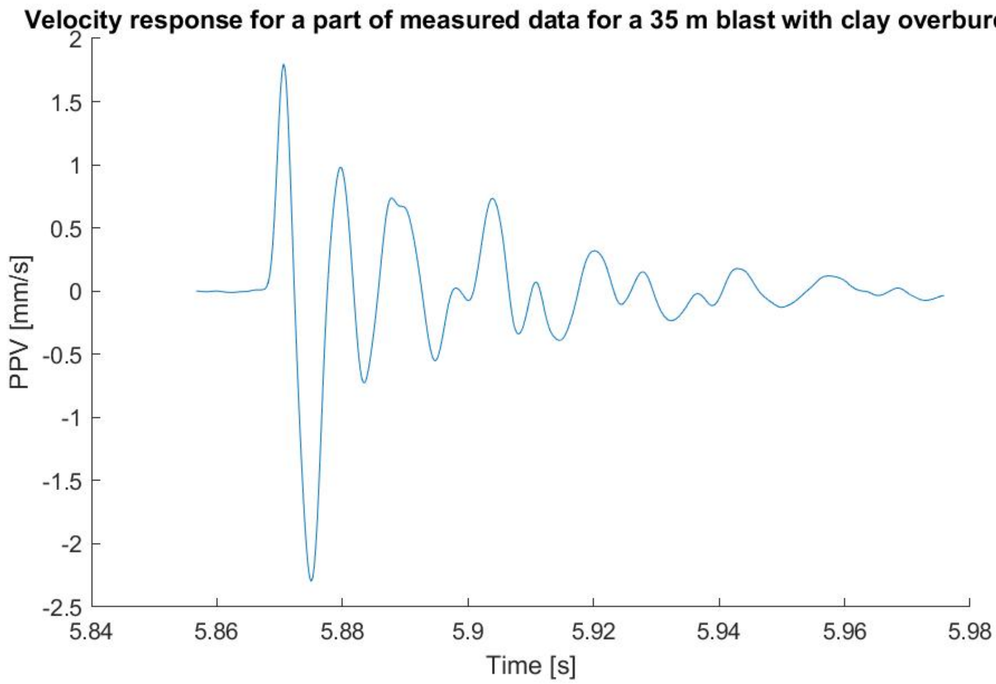

Figure 4.4: Velocity time response curve for one blast in rock at the distance of 35 m with overlaying clay, obtained from Nitroconsult.

Since there are no specific material properties and soil profiles given in the measured data obtained from Nitroconsult, the material models used in the calibrations are based on material data obtained from Markera Mark AB. Thus the possibility of an exact calibration for the numerical model to the measured data is highly improbable. Since the velocity response curves from Nitroconsult originate from underground tunnel blasting, it is assumed that the blast hole is located directly underneath the measure points. The geometries used in the calibrations is seen in Figures 4.5 and 4.6.

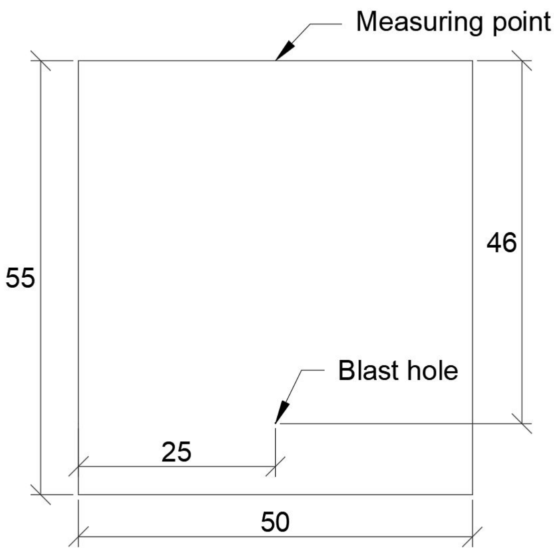

Figure 4.5: Geometry used for calibrating in only rock.

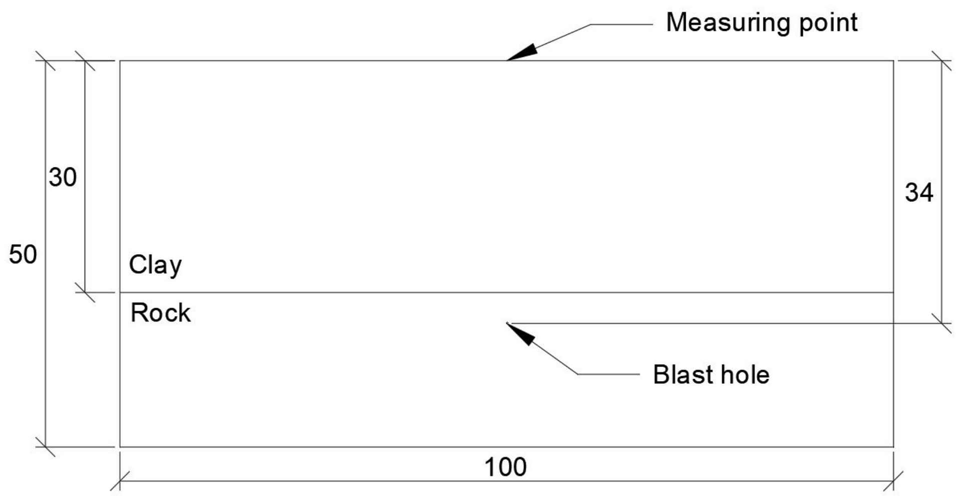

Figure 4.6: Geometry used for calibrating with a soil profile of rock and clay.

4.2.1.1 Blast function

There are two factors in the blasting function that can be calibrated in order to achieve accuracy between the numerical model and the measured data. Firstly, the amplitude of the vibration can be calibrated by varying the blast hole pressure P_b calculated with equation 2.78. Since the material models are linear elastic, a normalization of the velocity response curve for both the numerical and the measured data are made. This simplified the comparison between the two curves. Secondly, the rising time, t_r, in Equation 2.79 has significant influence on the frequency range. The rising time t_r is chosen through an iterative procedure such that the frequency range of the numerical blasting vibrations is calibrated to the velocity response for the measured blasting induced vibrations, seen in Figures 4.3 and 4.4. The rising time, t_r, is evaluated in the interval of $1 \leq t_r \leq 2$ ms.

4.2.1.2 Damping effects

The effect of damping in transient wave propagation analyses can be modeled in COMSOL using Rayleigh damping. In order to calibrate the numerical model to the measured data, it is necessary to dampen higher frequencies. Appropriate damping ratios, ζ_1, ζ_2 and damping frequency range, f_1 and f_2 are chosen through an iterative process, which reduces the maximum frequencies of the model. By damping the unnecessary high frequencies it is possible to generate a courser mesh without any loss of accuracy. The Rayleigh damping parameters are evaluated at $f_1 = 0$ Hz, $200 \leq f_2 \leq 2000\ Hz$ with $\zeta_1 = 0$ and $\zeta_2 = 0.05$.

4.2.1.3 Material model

In Chapter 2, a poroelastic and an elastic material model are introduced for clay. By using the same blasting function and damping as described in Sections 4.2.1.1 and 4.2.1.2 and material data from Table 4.1, velocity response curves for both elastic and poroelastic material models are made and compared to the velocity response curves acquired from Nitroconsult.

4.2.1.4 Width of the model

In order to verify the validity of the boundary conditions, the size of the domain is altered. This is done for both the domain only made of rock and for the domain with both rock and clay. In both cases the width of the model varies between 50 and 150 m. Boundary conditions used are a free surface at the top of the model and low reflecting boundaries at the sides and at the bottom for the solid phase, see Figures 4.7 and 4.8. The boundary conditions used in the poroelastic material model are No Flow boundaries at the free surface, the interface between the poroelastic clay and the elastic rock and at the left and right sides.

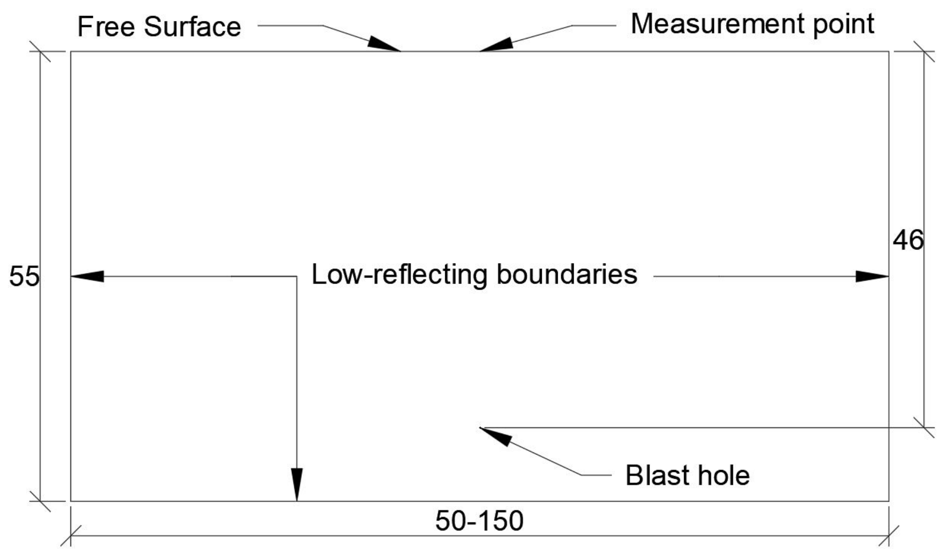

Figure 4.7: A domain for testing the difference between varying widths of the rock model.

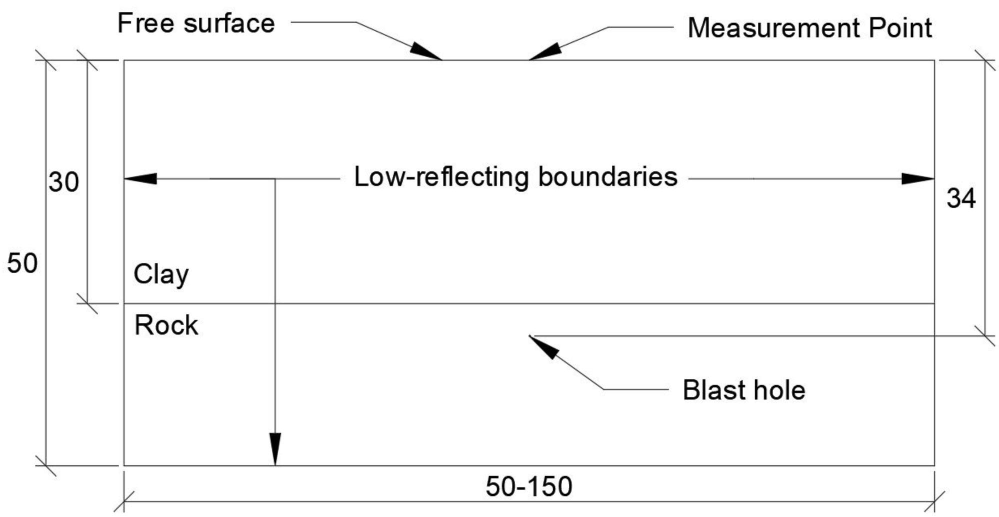

Figure 4.8: A domain for testing the difference between varying widths of the rock and clay model.

4.2.2 Material parameters

The material parameters in the poroelastic model are not typical for site measurements and have not been acquired from Markera Mark AB. Therefore, in order to determine the importance of each parameter used in the poroelastic model, the parameters are varied one by one in several models. The material parameters that are studied are the compressibility of the fluid, Poisson's ratio and Young's modulus. The models used in the studies are calibrated according to Section 4.2.1. The models created in this Section are all made with a poroelastic material model.

4.2.2.1 Compressibility of fluid

The compressibility of a fluid in a porous material is dependent on the degree of saturation, as seen in Section 2.1.3. A clay can be considered as fully saturated under the phreatic surface. However, as Verruijt (2010) states, there will always be air bubbles within the porous skeleton. Thus, the analysis is made by assuming different degrees of saturation, from 0.95 to 1 as seen in Table 4.2

Table 4.2: The saturation degrees and corresponding compressibility for the compressibility analysis.

Degree of saturation [−]	**Compressibility** [1/Pa]
0.95	$5.0048 \cdot 10^{-7}$
0.99	$1.0050 \cdot 10^{-7}$
1	$5.0000 \cdot 10^{-10}$

4.2.2.2 Poisson's ratio

For clays, Poisson's ratio is usually assumed as 0.5 (Hall 2013) and is classified as an incompressible material. By inserting $\nu \to 0.5$ in the wave speed Equation 2.25 it can be determined that $c_P \to \infty$. Because of this, an analysis of Poisson's ratio is done by varying it between 0.49 to 0.499.

4.2.2.3 Young's modulus

The Swedish Standard for blasting induced vibrations accounts for material below the point of measurement through the parameter v_0. The parameter v_0, is as mentioned in Section 2.5.1 related to the wave speed c_P. However, as mentioned in Section 2.1.1, the wave speed is a stiffness dependent parameter. Thus a study of stiffness variations in clay is done in order to assess the predictability of v_0.

The model consist of a 50×100 m^2 domain with a clay depth of 30 m, as seen in Figure 4.9. Poisson's ratio is chosen as $\nu = 0.495$. Young's modulus as a function of the soil depth is linearly approximated based on the material data obtained from Markera Mark AB, as described in Section 4.1, the linear increase of stiffness is shown in Figure 4.10. Three equations for the increase in tangent Young's modulus, E_0, is studied according to Table 4.3.

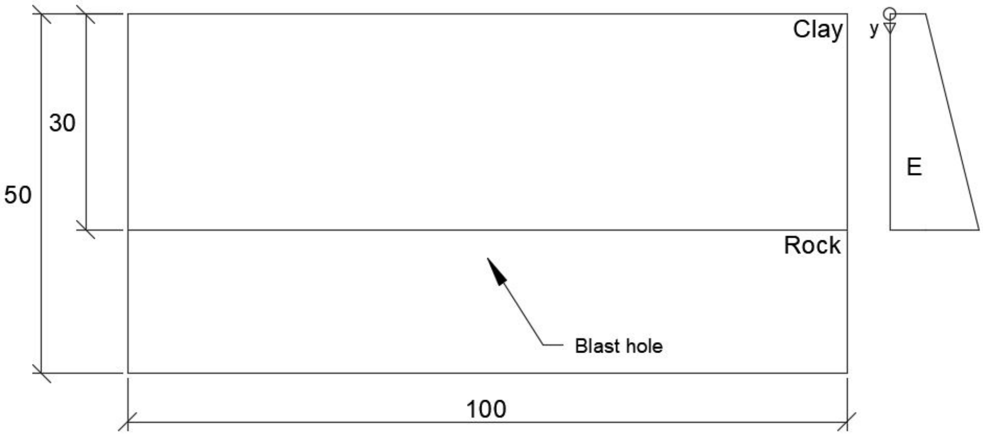

Figure 4.9: Model for stiffness analyses.

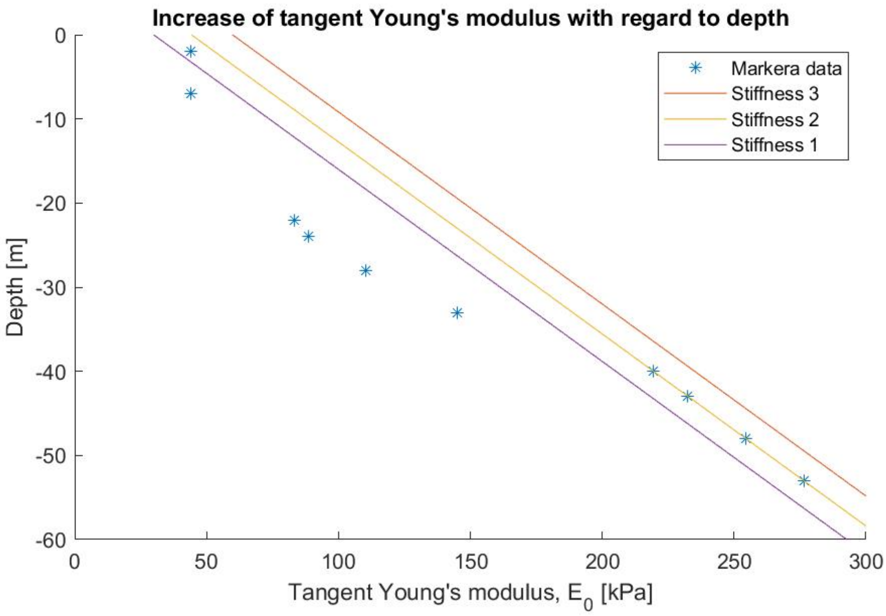

Figure 4.10: Linear increase in Youngs modulus with regard to depth in clay layer.

Table 4.3: The linear increase of tangent Young's modulus for the stiffness variation analysis.

Model	**Young's Modulus** [kPa]
Stiffness 1	$29900 + 4381y$
Stiffness 2	$44204 + 4381y$
Stiffness 3	$59800 + 4381y$

4.2.2.4 Overburden surface layer

As described in Section 2.5.1, the guidance level is dependent on which material is closest to the surface. In order do study the difference in the frequency spectrum for either clay- or rock overburden, two models are made with a blast at 34 m but different overburdens. The geometry for this study can be seen in Figures 4.11 and 4.12.

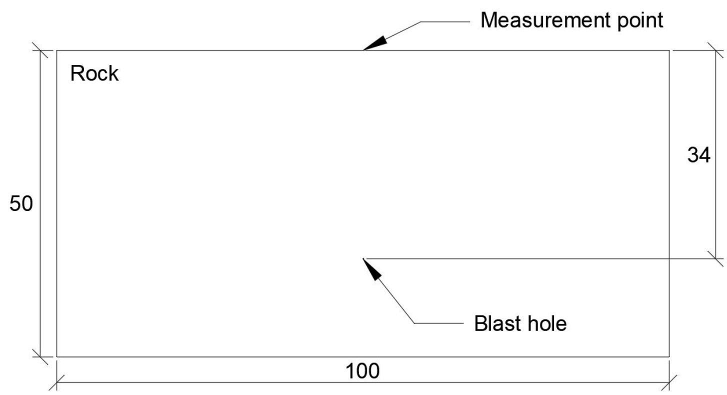

Figure 4.11: The geometry for a 34 meter blast with rock overburden.

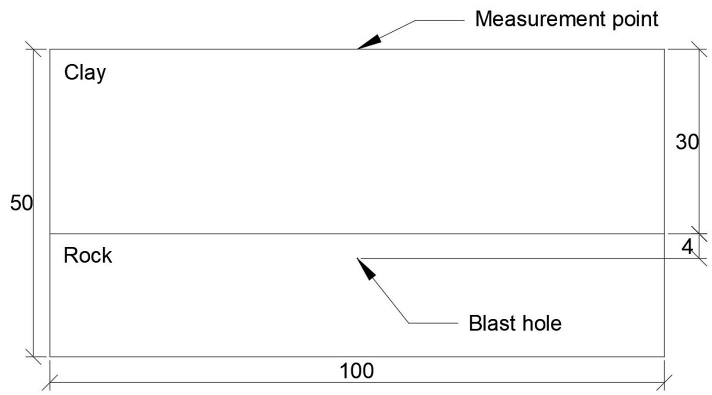

Figure 4.12: The geometry for a 34 meter blast with clay as overburden.

4.2.3 Geometric parameters

In this section, the blasting induced vibrations dependency on geometrical variations is studied. The materials models are poroelastic clay and elastic rock with the material parameters as seen in Table 4.1. The models used in the studies are calibrated according to Section 4.2.1.

4.2.3.1 Distance factor

As seen in Section 2.5.1, the guidance level for PPV is lowered for increasing distances from the blast hole. By modelling a blast from an increasingly longer distance from the measuring point, as seen in Figure 4.13, a relation between blast length and frequencies can be established. The blast range is varied between 10 and 100 meter.

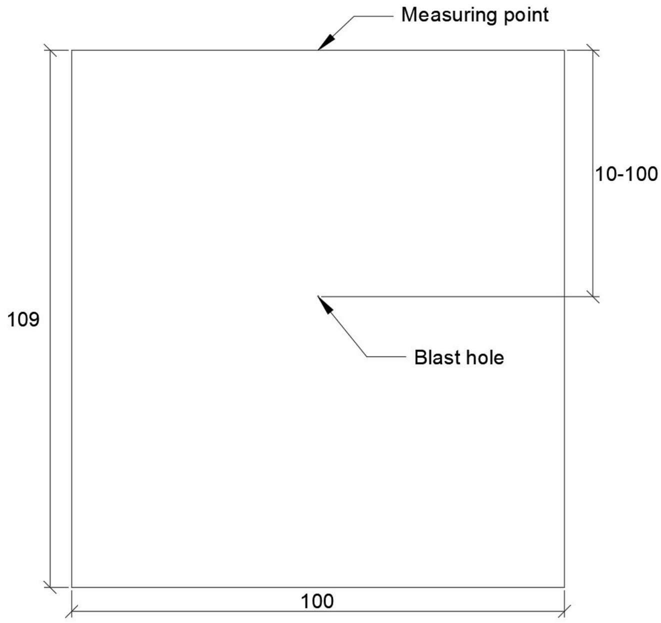

Figure 4.13: The geometry for increased range of the blast hole.

4.2.3.2 Depth of clay

This model is intended to study the overburden's effect on the blasting induced ground vibration. As seen in Section 2.5.1, the guidance value from the Swedish Standard does not consider the depth of the soil layers. Therefore, models are created with the same range between measuring point and detonation point, but different depth of clay layer, which according to the Swedish Standard, will have the same guidance level. In particular, the depth of the clay is modeled in the range $5 \leq x \leq 40$ m, see Figure 4.14.

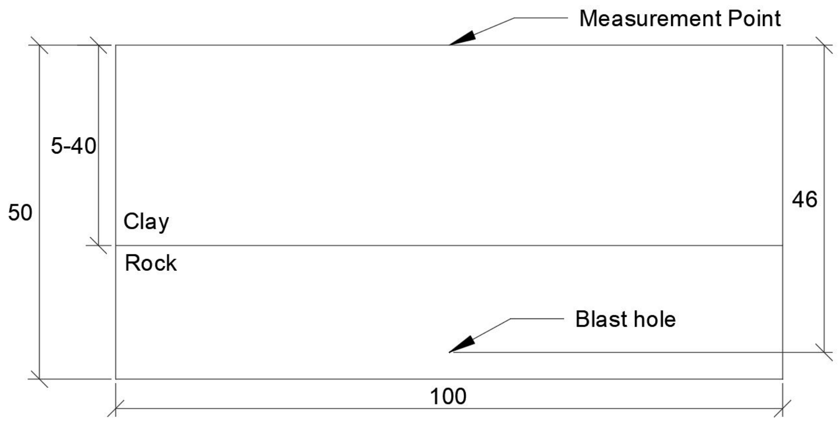

Figure 4.14: The geometry for the study of the depth of clay.

4.2.3.3 Angle of incidence

The distance parameter from Section 2.5.1 regulates the guidance value depending on both overburden and distance, but it does not take the angle of incidence into account. Models are therefore made with blast points at the same range from the measuring point, but with alternating depth from the surface, see Figure 4.15. This entails that for all angles, the guidance level from the Swedish Standard are the same.

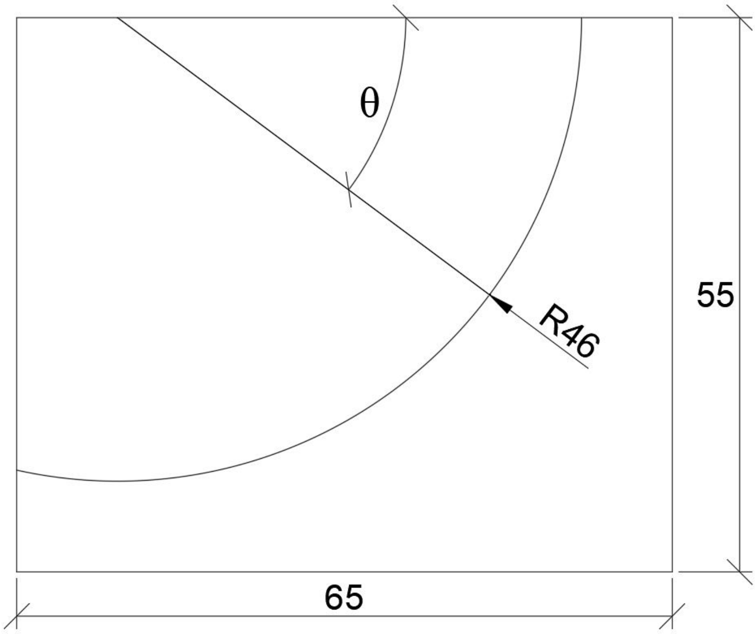

Figure 4.15: A 60 meter wide domain for testing the boundary conditions.

5 Results

5.1 Wave Speeds

This result is from Section 4.2. With the material data obtained from Markera Mark AB and those found in literature the wave speeds for the materials are calculated. The calculation is done according to Equations 2.13, 2.14, 2.25, 2.26 and Section 2.2.4.3. The calculation on the Rayleigh wave is seen in Appendix B and the calculations on poroelastic waves are seen in Appendix C. The wave speeds in clay are calculated from maximum and minimum stiffness based on the material data obtain from Markera Mark AB. The hand calculations on wave speed are used to evaluate the wave propagation in the numerical models. Since the speed of the wavefront is not determined by the damping, as mentioned by Bos & Slawinski (2010), the damping parameters are disregarded in the calculations on the wave speeds.

Table 5.1: Elastic wave speeds calculated based on the material parameters used in the study for clay depth of $1 - 53$ m.

Parameter	**Rock**	**Clay**	**Unit**
λ	$24 \cdot 10^9$	$1.4 \cdot 10^9 - 9.2 \cdot 10^9$	Pa
μ	$24 \cdot 10^9$	$14 \cdot 10^6 - 92 \cdot 10^6$	Pa
c_P	5262	$961 - 1445$	m/s
c_S	3038	$94 - 143$	m/s
c_R	2900	$89 - 123$	m/s

Table 5.2: Poroelastic wave speeds calculated based on the material parameters used in the study for clay depth of $1 - 53$ m.

Parameter	**Clay**	**Unit**
λ	$1.4 \cdot 10^9 - 9.2 \cdot 10^9$	Pa
μ	$14 \cdot 10^6 - 92 \cdot 10^6$	Pa
c_{P1}	$1335 - 2811$	m/s
c_{P2}	$0 - 1265$	m/s
c_S	$127 - 325$	m/s

The Biot critical frequency for clays is calculated conservatively by choosing the largest tortousity, $\alpha_\infty = 3.25$ as

$$\omega_{crit} = \frac{\mu\phi}{\alpha_\infty \kappa \rho_f} = \frac{1.05 \cdot 10^{-3} \cdot 0.7}{3.25 \cdot 10^{-10} \cdot 1000} = 2262\text{Hz}. \tag{5.1}$$

Thus, no P2-waves should be observed below 2262 Hz, according to Kudarova (2016). The hand calculated wave speed for poroelastic clay is plotted in Figure 5.1 together with the velocity response for for a numerical model of a blast in rock with an overburden of poroelastic clay. The poroelastic material is modeled with a constant stiffness with λ = 3.7 GPa and ν = 37.5 MPa in order to simplify the hand calculation seen in Appendix C.

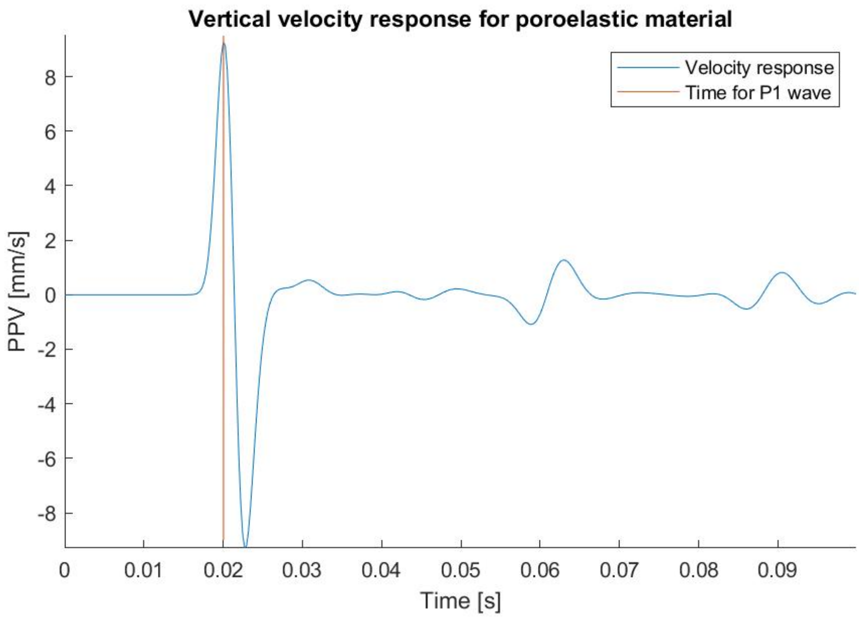

Figure 5.1: Numerical calculation with a poroelastic material model compared with hand calculation for poroelastic wave speed.

The hand calculation for the interface wave shown in Appendix D, showed that Equation 2.41 and 2.42 did not fulfill the boundary conditions in Equation 2.43 and 2.44, as seen in Figure 5.2. Thus, there were no interface waves for the material parameters used in the model.

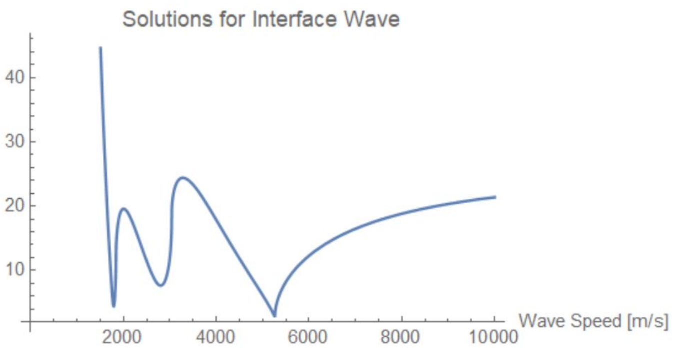

Figure 5.2: Solution for the wave in the solid-solid interface.

5.2 Convergence analysis

Th results presented here are from Section 3.5. The convergence study for the rock material is done with a model of $50m^2$ linear elastic rock. Rayleigh damping parameters are chosen as $f_1 = 0$, $\zeta_1 = 0$, $f_2 = 500$ and $\zeta_2 = 0.05$ in order to dampen the higher frequencies, as seen in figure 5.3. In Table 5.3 the amount of elements are seen for an increasing value of N_{rock}.

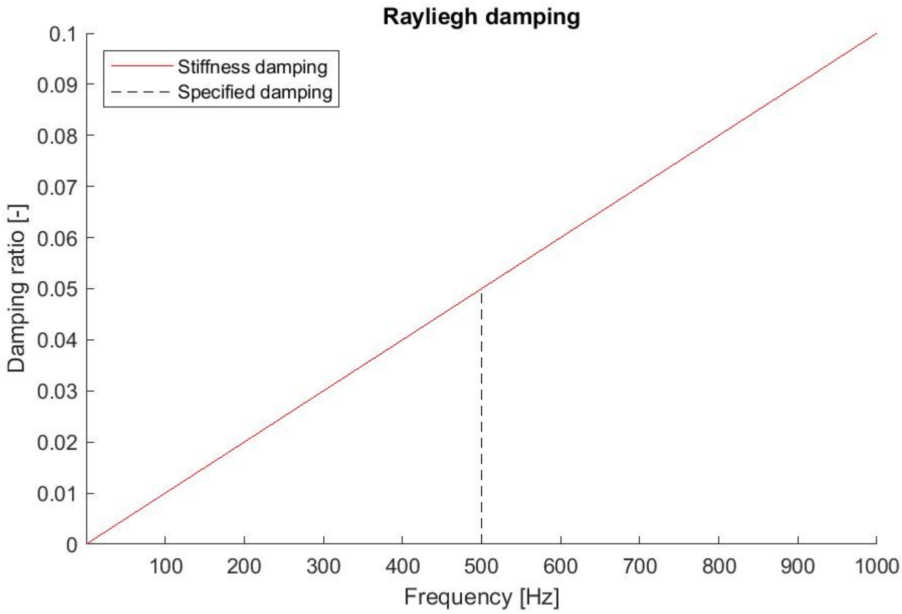

Figure 5.3: Rayleigh damping used to dampen high frequencies.

Table 5.3: The iteration scheme for the convergence analysis over the rock domain.

N_{rock}	**Elements**
0.1	1213
0.3	1368
0.4	1510
0.5	1463
1	1575
2	2284
3	3515

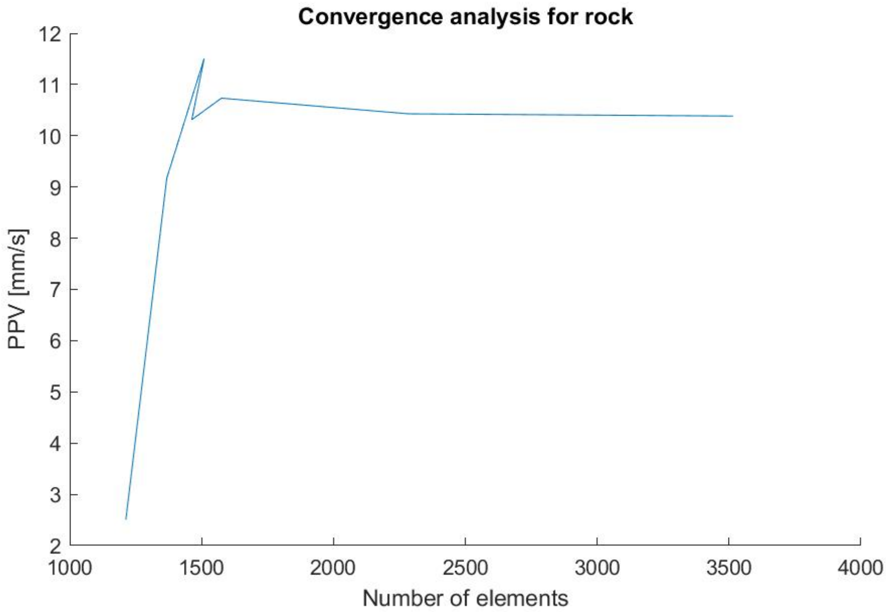

Figure 5.4: Convergence for rock material.

The spike in Figure 5.4 with 1510 elements in the domain could be due to difficulties of generating a mesh at $N_{\text{rock}} = 0.4$. It is clear from Figure 5.4 that a value of $N_{\text{rock}} = 2$, with 2284 elements in the domain, are enough for convergence to be reached in the rock material.

The convergence study for the clay material is done with the same procedure as for the rock material, increasing the value of N_{clay} successively until convergence is reached. In Table 5.4 the amount of elements are seen for an increasing value of N_{clay}. The procedure is done for both elastic and poroelastic material properties.

Table 5.4: The iteration scheme for the convergence analysis over the elastic and poroelastic clay domain.

N_{clay}	**Elements**
0.5	2722
0.7	3592
1	5412
1.2	6874
1.5	9644
2	15354
2.5	22644
3	31492

Convergence for elastic clay is reached at 31492 elements in the domain with $N_{\text{clay}} = 3$, as seen in Figure 5.5.

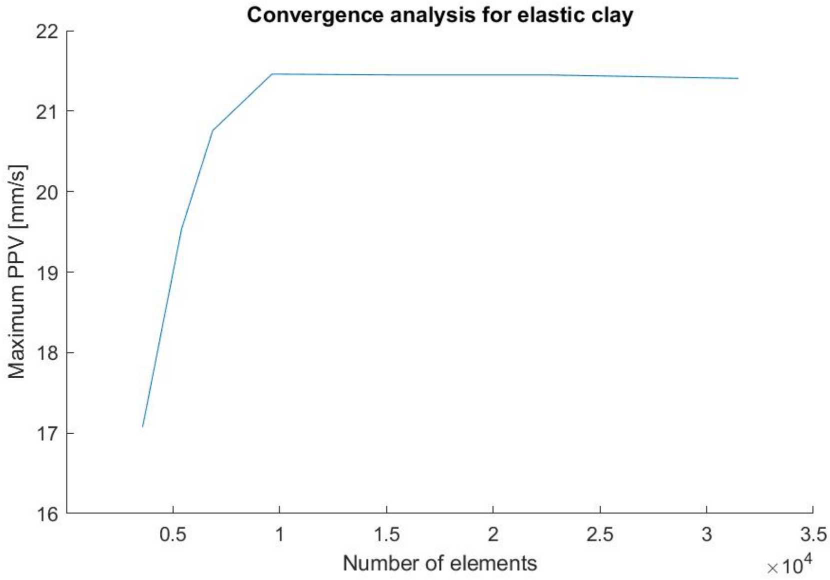

Figure 5.5: Convergence for elastic clay material.

Convergence for poroelastic clay is also reached at 31492 elements in the domain with $N_{\text{clay}} = 3$, as seen in Figure 5.6.

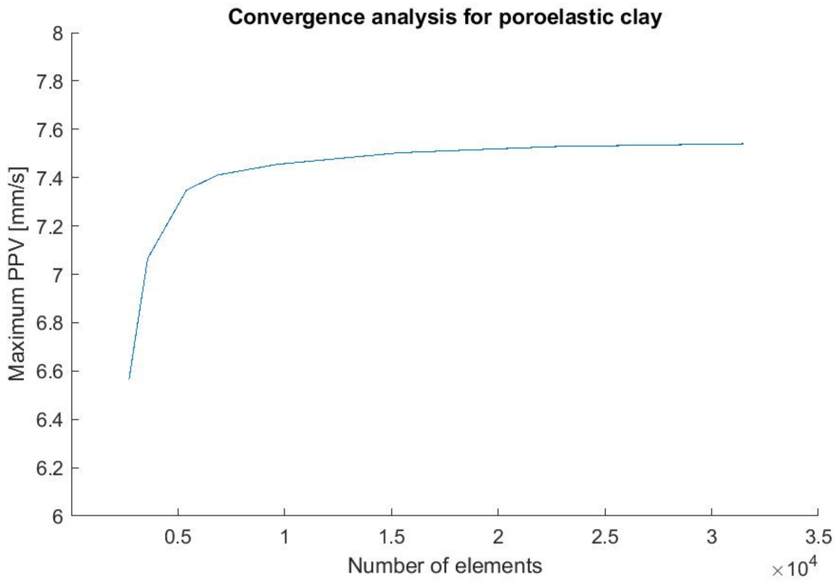

Figure 5.6: Convergence for poroelastic clay material.

5.3 Causality

The results from Section 3.6 is presented here. An undamped model, with a very fine mesh with $N_{\text{rock}} = 20$ and damped model with $N_{\text{rock}} = 2$ is compared with wave speed calculated in rock, as seen in Table 5.1.

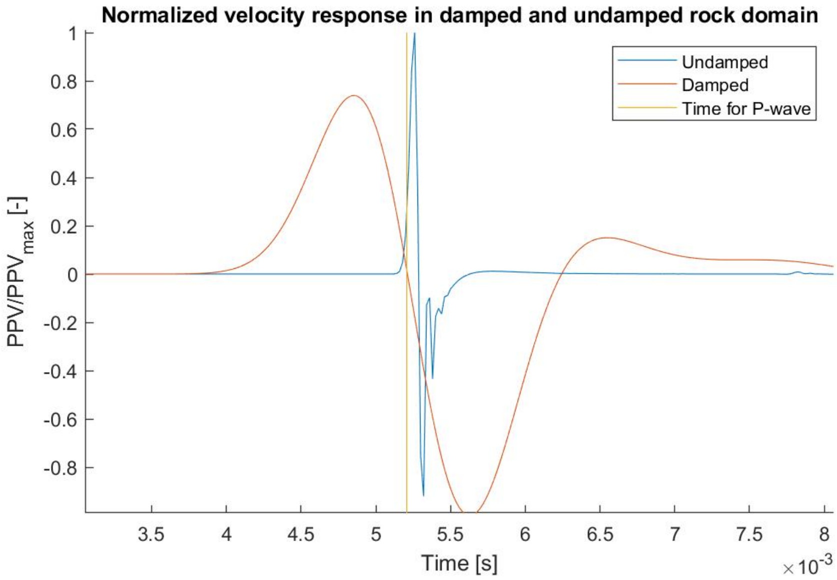

Figure 5.7: Velocity response for the undamped model with $N_{\text{rock}} = 20$.

In figure 5.7, the calculated P-wave the surface almost at the same time as the undamped model reaches the surface, thus the principle of causality is not satisfied for the undamped model. However, it is possible that causality can be achieved with a finer mesh. Furthermore, the undamped model with $N_{\text{rock}} = 20$ took approximately 15 hours of computational time, without converging, thus no model with finer mesh was generated.

The damped model plotted in Figure **??** have converged but the calculated P-wave reaches the surface after damped model, thus the principle of causality is not satisfied for the damped model. It is possible, as mentioned by Antes & Von Estorff (1987), that this is due to numerical problems rising due to the frequency based damping. The coming studies are done with a damped model, even though it does not satisfy the principle of causality.

5.4 Calibration

Here the results from Section 4.2.1 are presented. The material data obtained from Markera Mark AB is from a soil profile in Gothenburg, from the West link project. The blasting data obtained from Nitroconsult is from another project, thus the soil conditions for the separate projects are presumably completely different. With this in consideration, the calibration of the numerical model is done with a normalized amplitude. It is then possible to calibrate simple numerical models to the obtained blasting measurement data and the material properties of soil in Gothenburg, both for a rock and for a clay profile. The calibration of the models are made in order to have realistic response in the numerical calculations.

The calibration process is made for three models. One model is calibrated for a domain consisting only of rock. The other two models are calibrated for both rock and clay domains but with different material models for the clay, elastic and poroelastic. In Appendix E, figures of the wave propagation is presented for each calibration model.

As written in Chapter 4.2.1, the calibration is done with respect to the rising time for the blasting function. The influence on the velocity response and the frequency spectrum due to a change in rising time is presented in Figures 5.8 and 5.9. The change of rising time has an effect on the negative amplitude of the velocity response, as the rising time increased, the negative amplitude decreased.

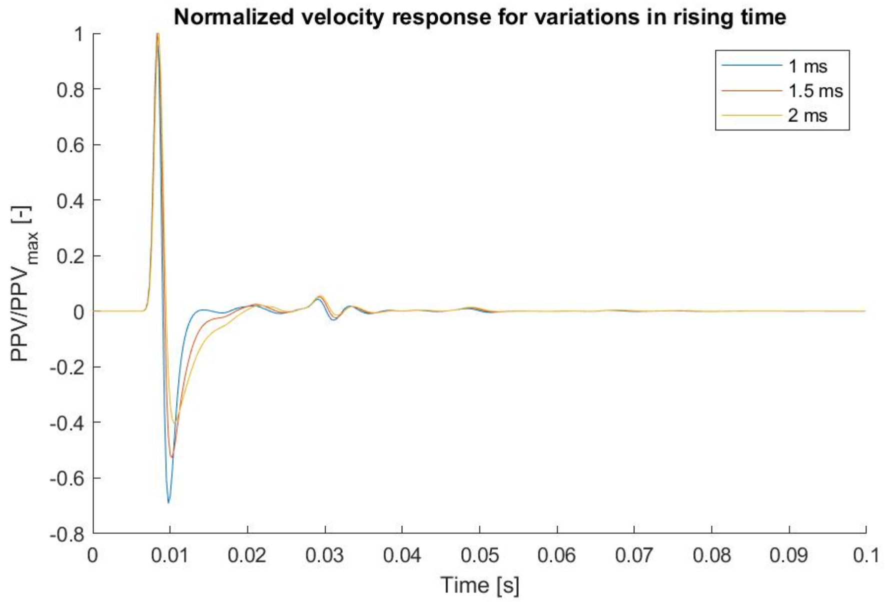

Figure 5.8: The velocity response for the variation in rising time.

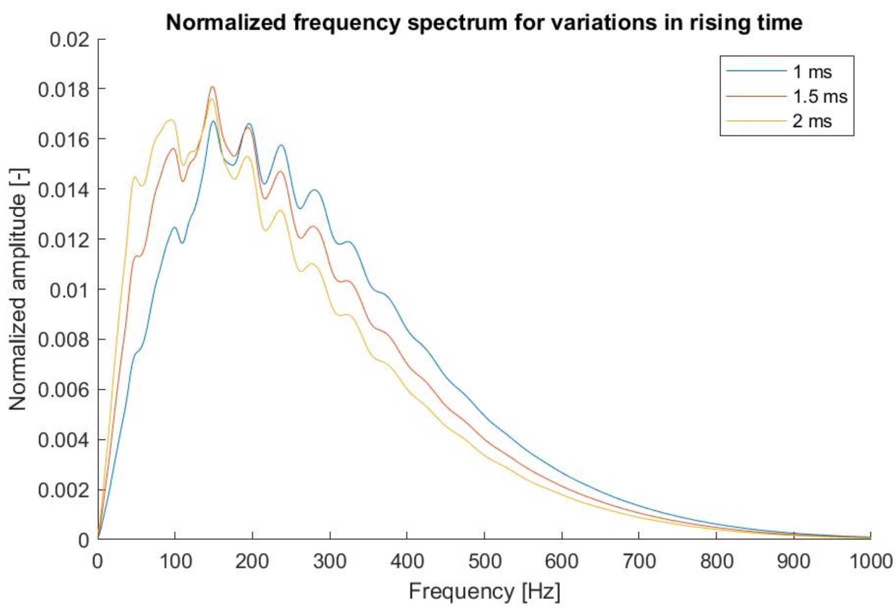

Figure 5.9: The frequency spectrum for the variation in rising time.

5.4.1 Rock calibration

The calibrated curves for velocity response and frequency spectrum are plotted and compared with measured values in Figures 5.10 and 5.11. The rising time used in the calibrated model is $t_r = 1$ ms and the damping parameters are $f_1 = 0$, $\zeta_1 = 0$, $f_2 = 500$ and $\zeta_2 = 0.05$

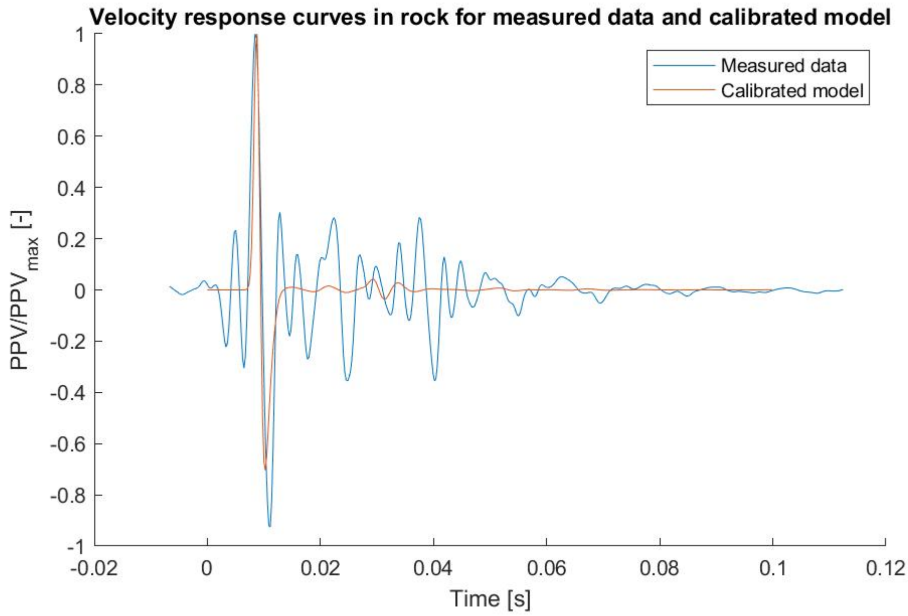

Figure 5.10: Velocity response curves for the calibrated model and the measured data.

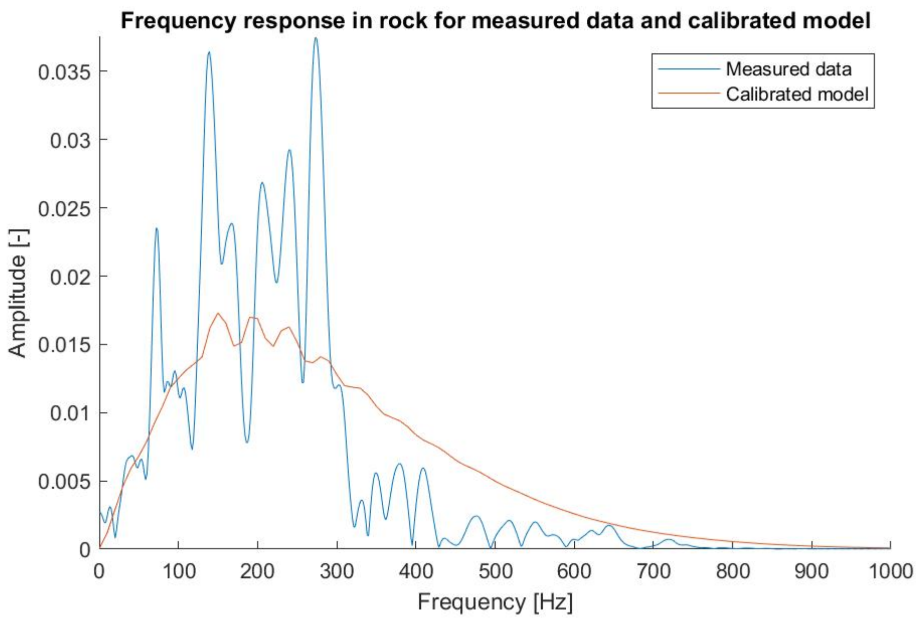

Figure 5.11: Frequency spectrums for the calibrated model and the measured data.

In Figure 5.10, the velocity response in the numerical model shows similarities with the measured blasting data. With the normalization, it is possible to capture the oscillation with the largest amplitude in the velocity response curve. However, as the numerical model is an elastic solid, the numerical velocity response included less interference than the measured velocity response. The oscillations with lower amplitudes in the measured data in Figure 5.10 could be caused by cracks and faults that gave rise to interference and damping, as mentioned by Yang J et. al (2016). The frequency response spectrum, as seen in Figure 5.11, shows comparable result. In the frequency range of $1 \leq f \leq 60$ Hz, a good correlation is achieved. However, larger frequencies do not show a good correlation.

As no material properties on cracks and faults in the rock are given, there is a large uncertainty on how to model the damping. However, as supported by Yang J et. al (2016), cracks and faults in the rock dampen out high frequencies. As seen in Figure 5.11, high frequencies are damped, therefore the damping model used in the model could presumably model the real behaviour of damping in rock.

5.4.2 Clay calibration

The velocity time response and the frequency spectrum of the calibrated models with an elastic material model for the clay are plotted in Figures 5.12 and 5.13. The rising time used in the calibrated model is $t_r = 1$ ms and the damping parameters are $f_1 = 0$ Hz, $\zeta_1 = 0$, $f_2 = 500$ Hz and $\zeta_2 = 0.05$.

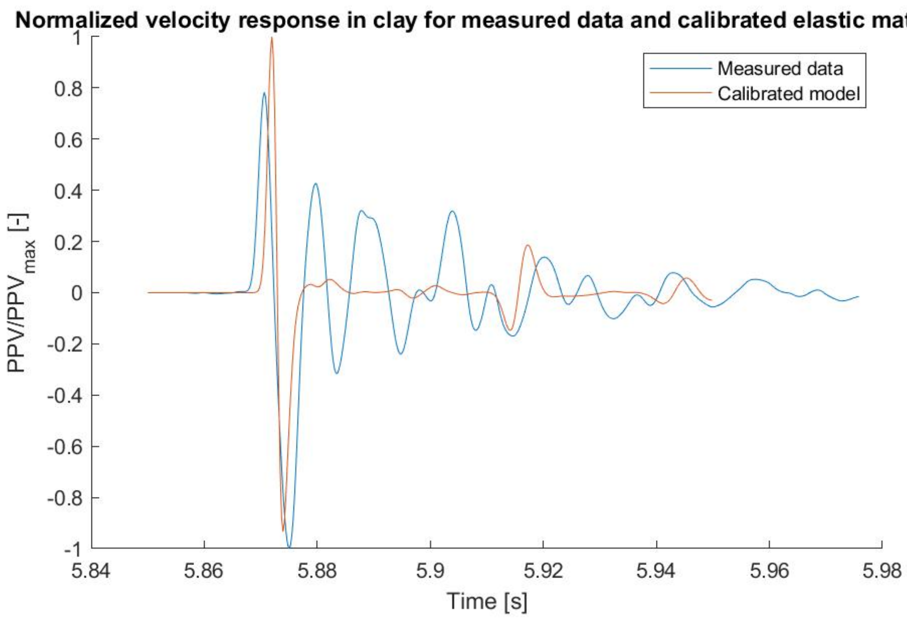

Figure 5.12: The velocity response for the calibration with an elastic material model.

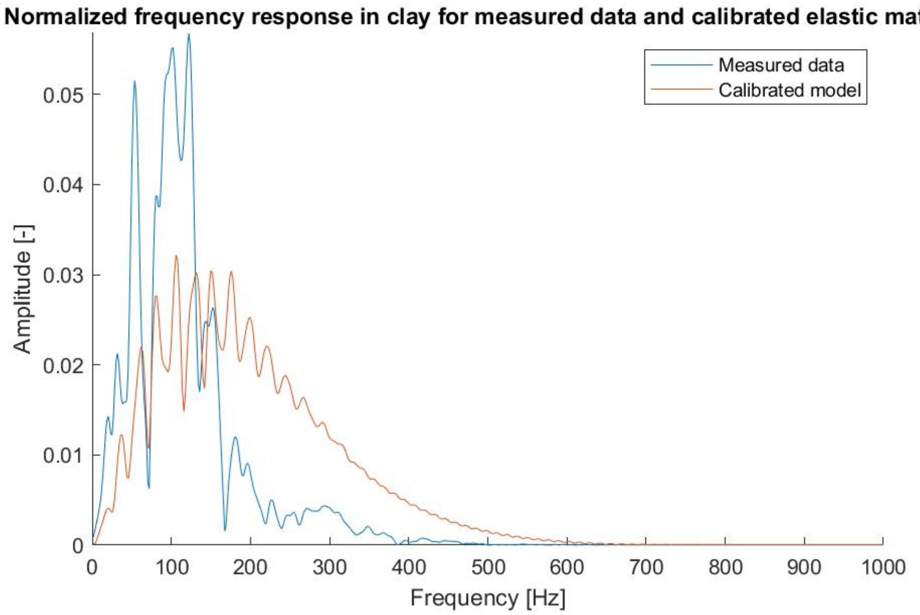

Figure 5.13: The frequency spectrum for the calibration with an elastic material model.

In Figures 5.14 and 5.15 the calibration for a poroelastic material model for the clay are presented. The clay is assumed to be fully saturated.

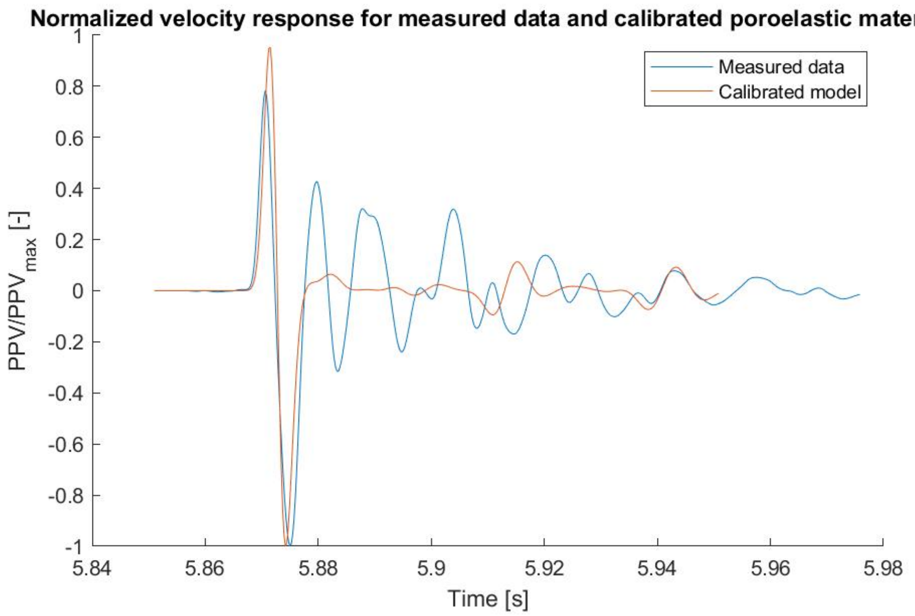

Figure 5.14: The velocity response for the calibration with a poroelastic material model.

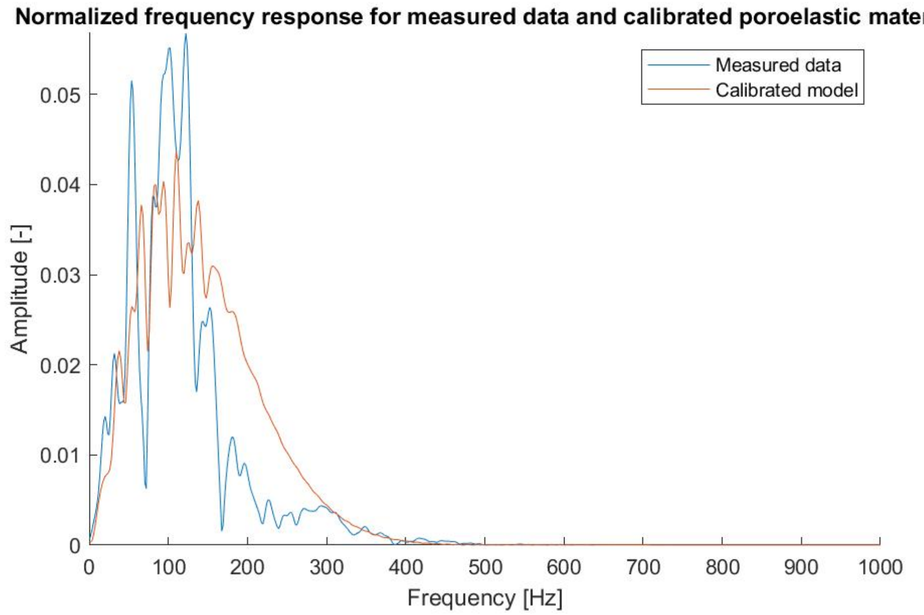

Figure 5.15: The frequency spectrum for the calibration with a poroelastic material model.

The calibration between the measured blasting data in clay and numerical model with an elastic material model showed a fairly good correlation. As seen in Figure 5.12, the velocity response in the calibrated model does not capture the maximum PPV of the measured data as the wave length in the measured data is larger than that of the numerical model. Furthermore, in the frequency response there is also a fairly good correlation for this case, as seen in Figure 5.13.

However, in the calibration of the numerical model with poroelastic clay model, the velocity response is more suitable than for elastic clay model, as seen in Figure 5.14. Furthermore, the frequency response of the calibrated numerical model with poroelastic material properties, as seen in Figure 5.15 shows similarities with the measured data, although it contained frequencies in the higher range. Thus the study argues for the importance of taking into account the water stored in the material.

5.4.3 Width of the model

These results are from Section 4.2.1.4. The variation of the width of the domain is made in order to verify the influence of the boundary conditions. The velocity response and frequency spectrum for a rock material model is plotted in Figures 5.16 and 5.17. In Figure 5.18 the maximum PPV is plotted for each point along the surface of the domain.

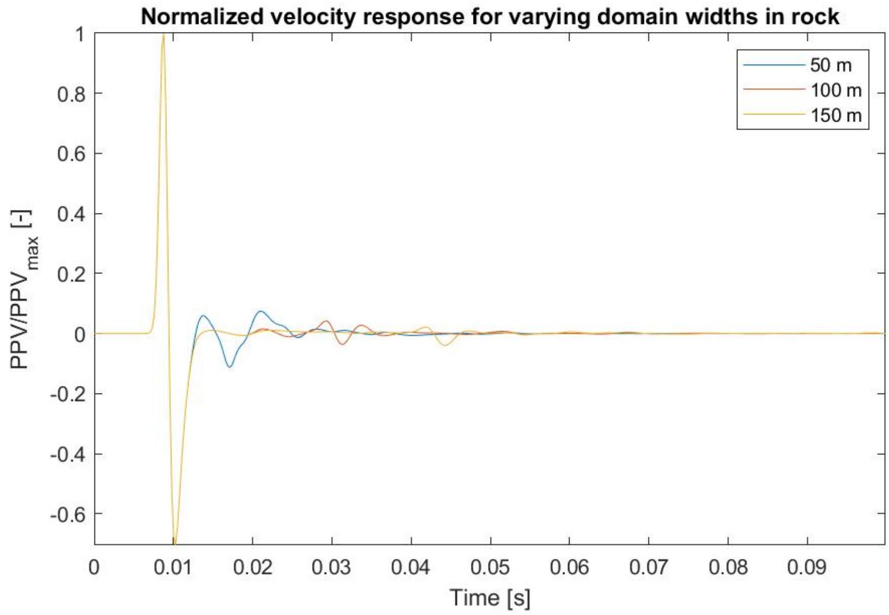

Figure 5.16: The velocity response for different widths of the rock domain.

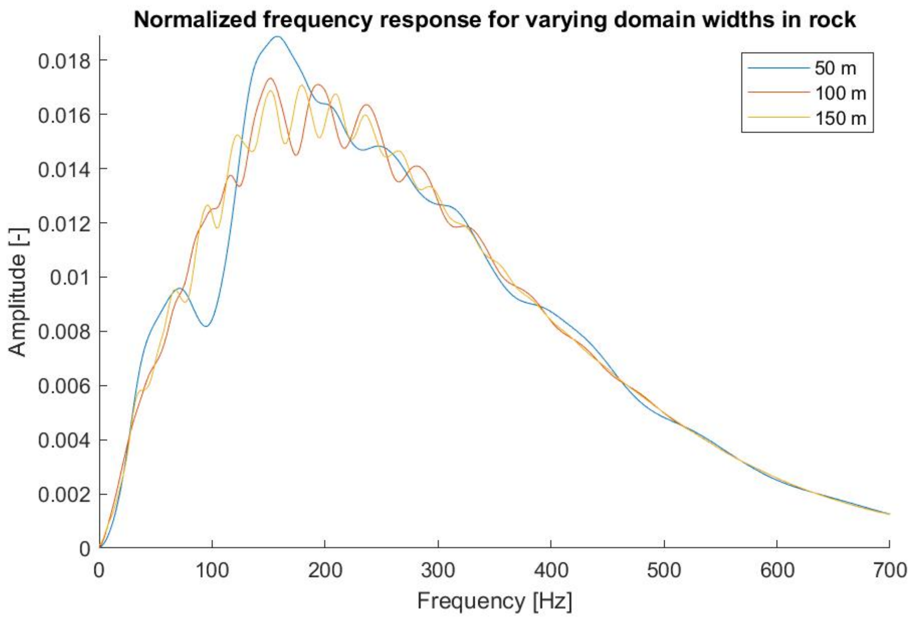

Figure 5.17: The frequency spectrum for different widths of the rock domain.

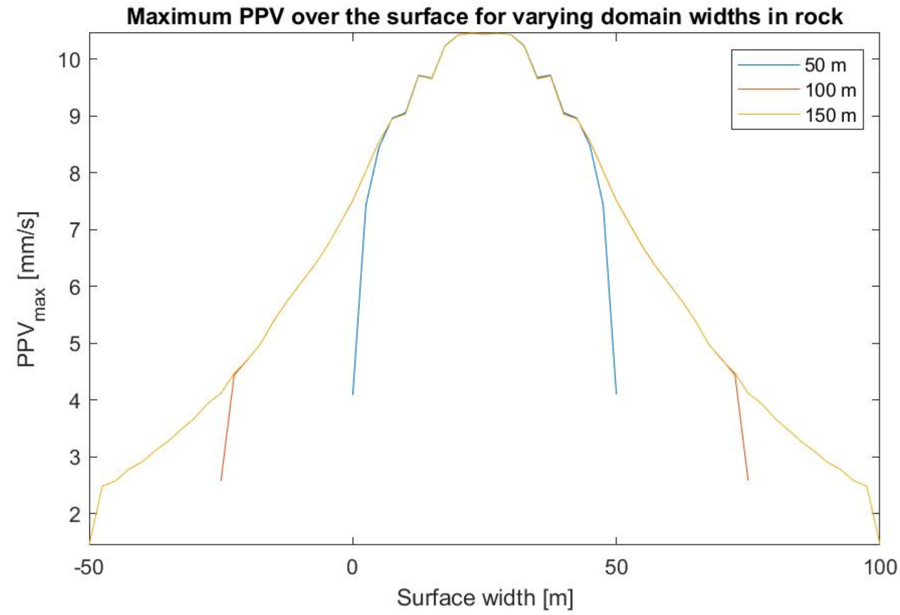

Figure 5.18: The maximum PPV for each point along the surface for different widths of the rock domain.

The velocity response and frequency spectrum for a clay with an elastic material model is plotted in Figures 5.19 and 5.20. In Figure 5.21 the maximum PPV is plotted for each point along the surface of the domain.

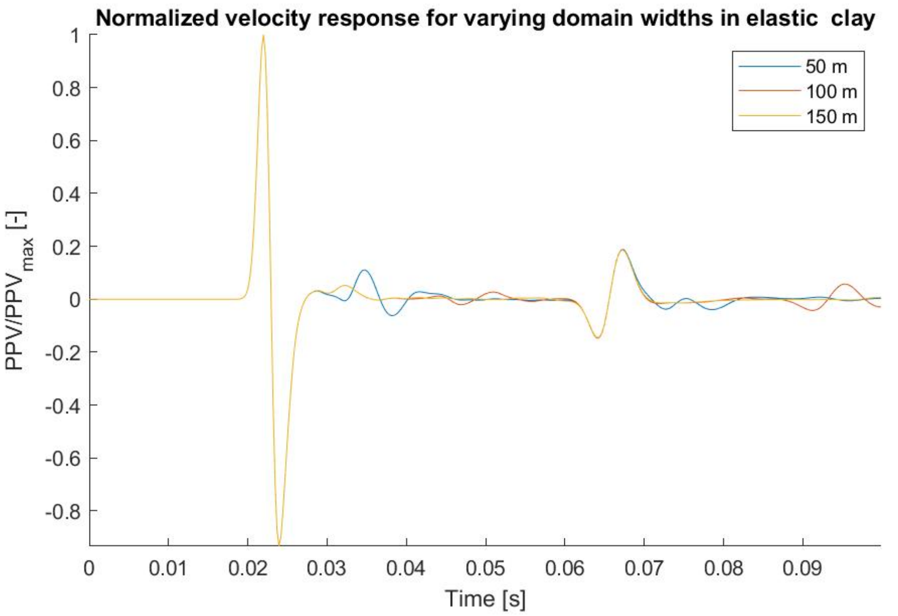

Figure 5.19: The velocity response for different widths of the rock and clay domain with an elastic material model.

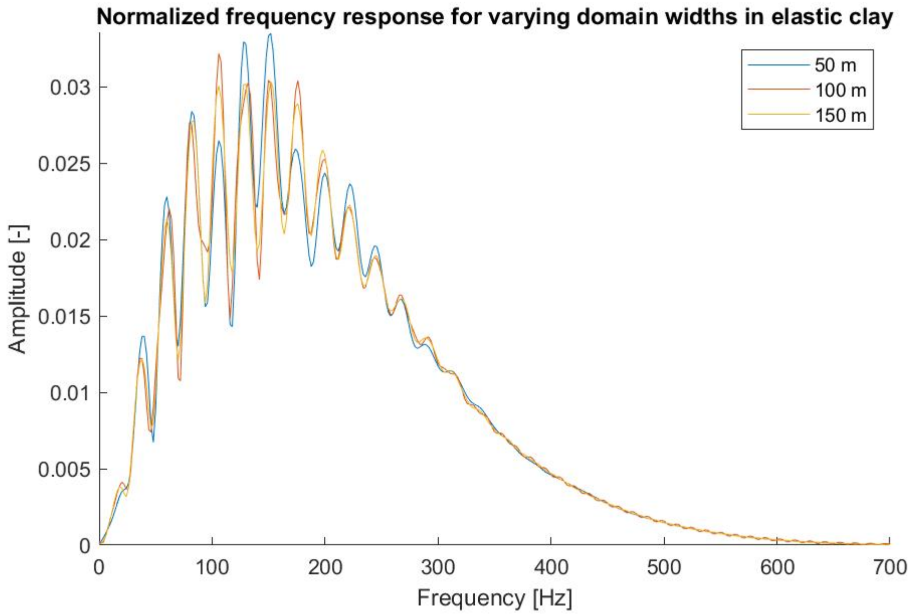

Figure 5.20: The frequency spectrum for different widths of the rock and clay domain with an elastic material model.

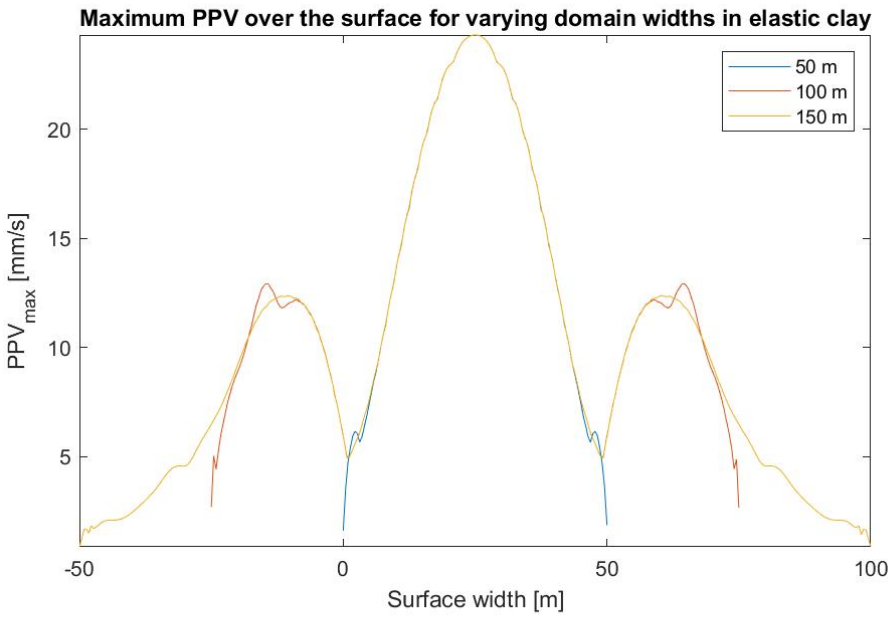

Figure 5.21: The maximum PPV for each point along the surface for different widths of the rock and clay domain with an elastic material model.

The velocity response and frequency spectrum for a clay with a poroelastic material model is plotted in Figures 5.22 and 5.23. In Figure 5.24 the maximum PPV is plotted for each point along the surface of the domain.

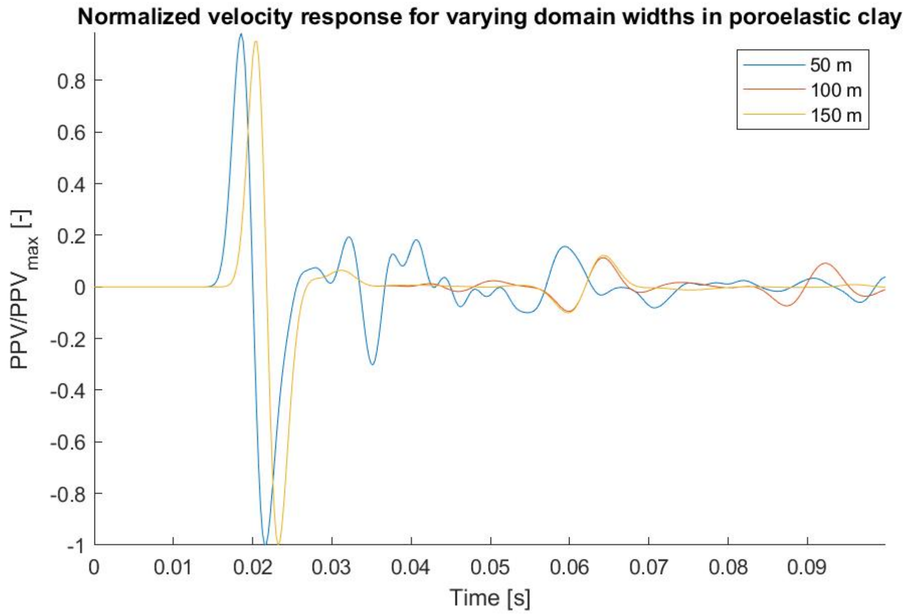

Figure 5.22: The velocity response for different widths of the rock and clay domain with a poroelastic material model.

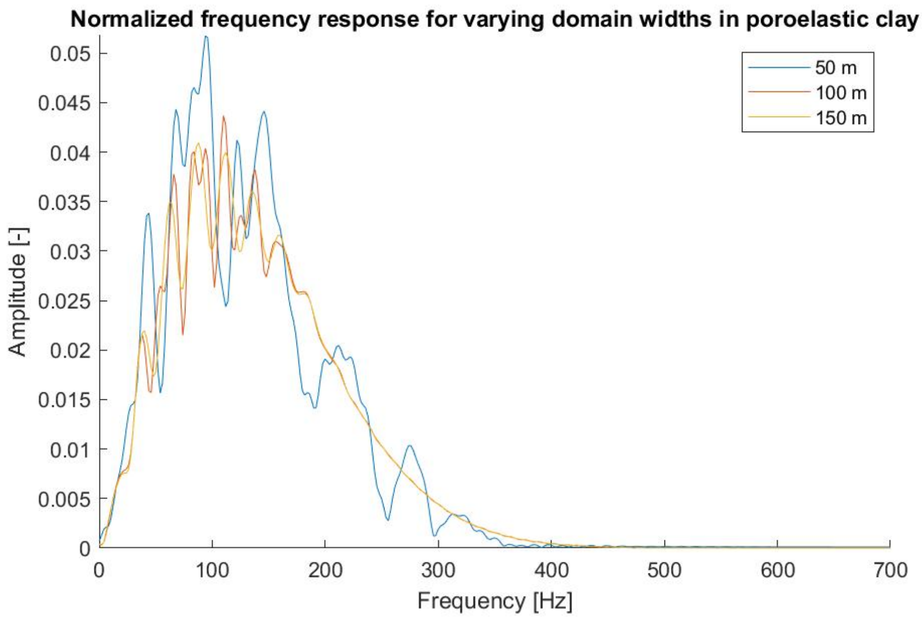

Figure 5.23: The frequency spectrum for different widths of the rock and clay domain with a poroelastic material model.

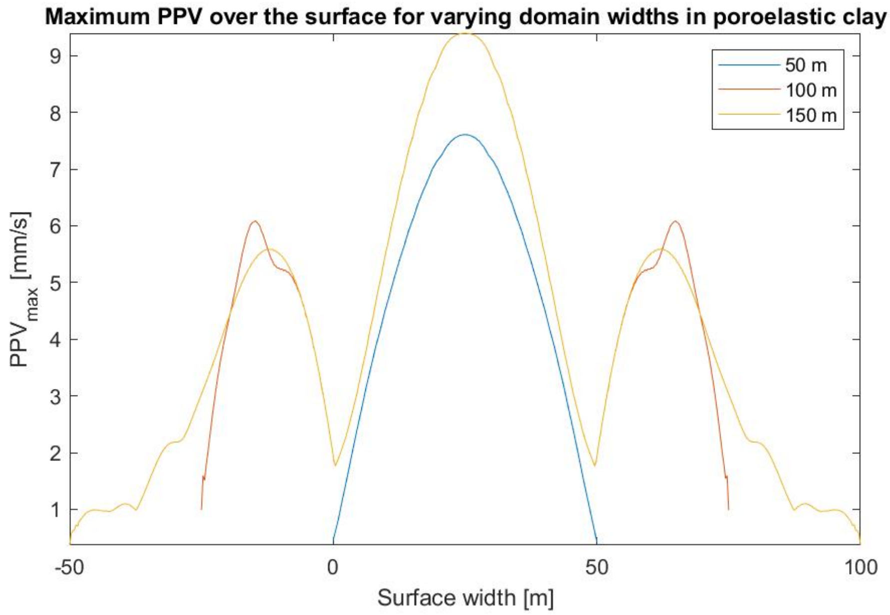

Figure 5.24: The maximum PPV for each point along the surface for different widths of the rock and clay domain with a poroelastic material model.

This study is done in order to evaluate the effect on the model with regard to the Low-Reflecting Boundary Conditions and the No Flow boundary conditions. As seen in Figures 5.18 and 5.21, a difference in width has no influence on the elastic material models. Whereas with the poroelastic material models, as seen in Figure 5.24, the No Flow boundary conditions has a significant influence on the maximum PPV on the free surface. With a width of 50 m, the maximum PPV is only 81% of the maximum PPV for a width of 100 and 150 m. This indicated that a model with a width of at least 100 m is needed in order for the boundary conditions to not have any effects on the PPV 90 degrees above the blast hole.

An interesting property of Figure 5.24 occurs at a distance of 30 m to the left and right of the peak above the blast hole. The same property is observed in the study of varying clay depth, as seen in Figure 5.37. In Appendix E, Figures E.5 to E.9 show the wave propagation for elastic material properties and it can be observed that this property occurs at the interface between the clay and the rock. It is likely that this is a consequence of the blast hole being close to the clay layer. However, as the hand calculation in Appendix D shows that the material parameters used in the model did not give rise to any interfaces waves. It is possible that this property occurs due to incident S-waves from the blast, which refract P-waves with a lower angle of refraction, as explained in Figure 2.10b.

5.5 Material parameters

In this section, the results for the parametric study of the material parameters are presented. As only one parameter is varied for each study, the other parameters are listed in Table 4.1.

5.5.1 Compressibility of fluid

The results from Section 4.2.2.1 are presented here. The velocity response and frequency spectrum for variation of saturation in clay with a poroelastic material model is presented in Figures 5.25 and 5.26. The difference between $S = 0.99$ and $S = 0.95$ is small and the plots for these values are almost identical.

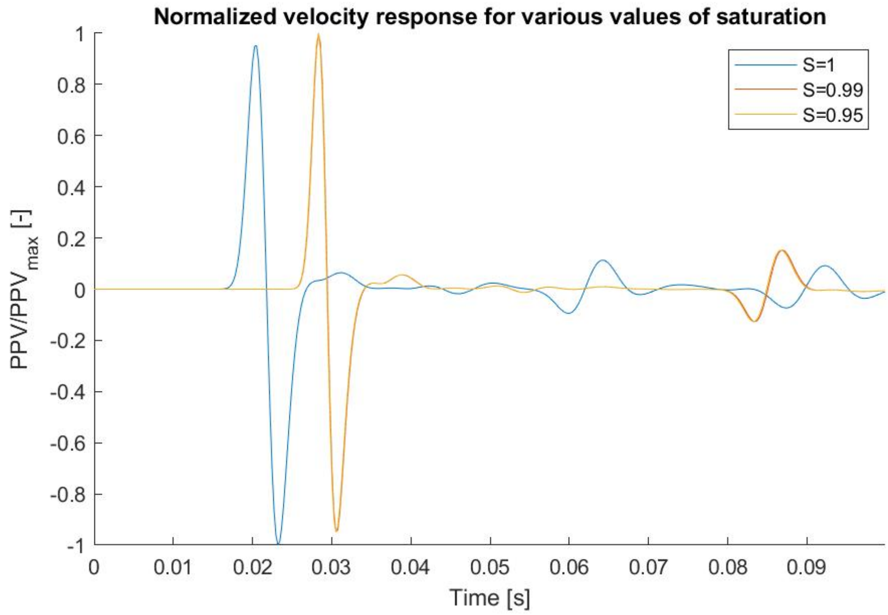

Figure 5.25: Normalized velocity time response of a numerical blast with saturation variation in the clay.

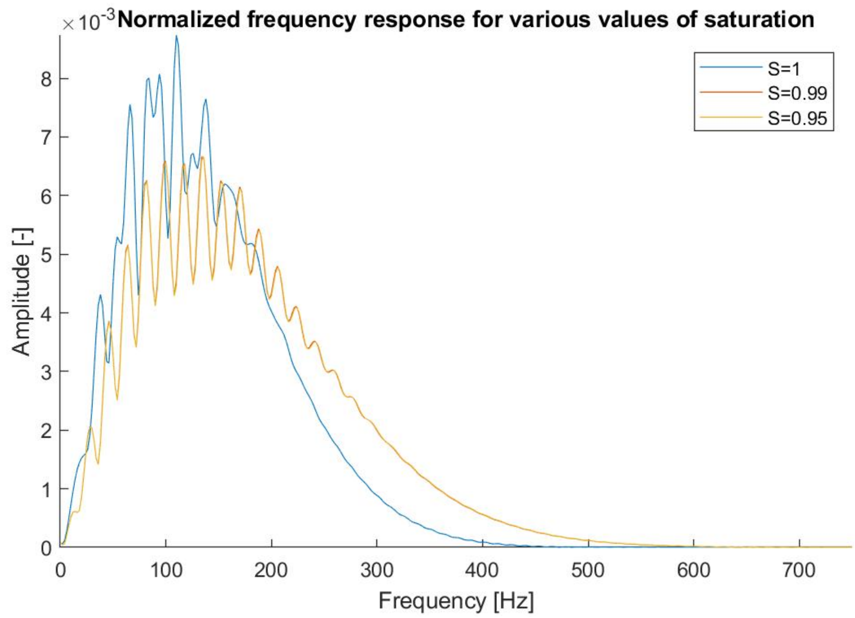

Figure 5.26: Normalized frequency spectrum of a numerical blast with saturation variation in the clay.

It is possible to evaluate the dependency on the degree of water saturation in the soil through the parameter compressibility. As mentioned in the Section 2.1.3, it is impossible for the degree of saturation to reach 100 %. The sensitivity analysis for the degree of saturation shows that even a small variation in saturation yields a significant change in velocity and frequency responses. As is seen in Figure 5.25, a higher degree of saturation resulted in an increased wave speed. It is also shown in Figure 5.26 that an increased degree of saturation gives rise to lower frequencies.

5.5.2 Poisson's ratio

The results from Section 4.2.2.2 are presented here. In Figures 5.27 and 5.28 the velocity response and the frequency spectrum can be seen for the variation of Poisson's ratio respectively.

Figure 5.27 shows that an increased Poisson's ratio gives rise to an increased wave speed. This is expected since an increased Poisson's ratio increases the value of the Lamé constant λ, which in turn increases the wave speed of the P-wave, c_P.

Figure 5.28 shows that an increased Poisson's ratio results in more frequencies in the higher frequency range. The study shows that Poisson's ratio is a sensitive parameter as it approaches 0.5.

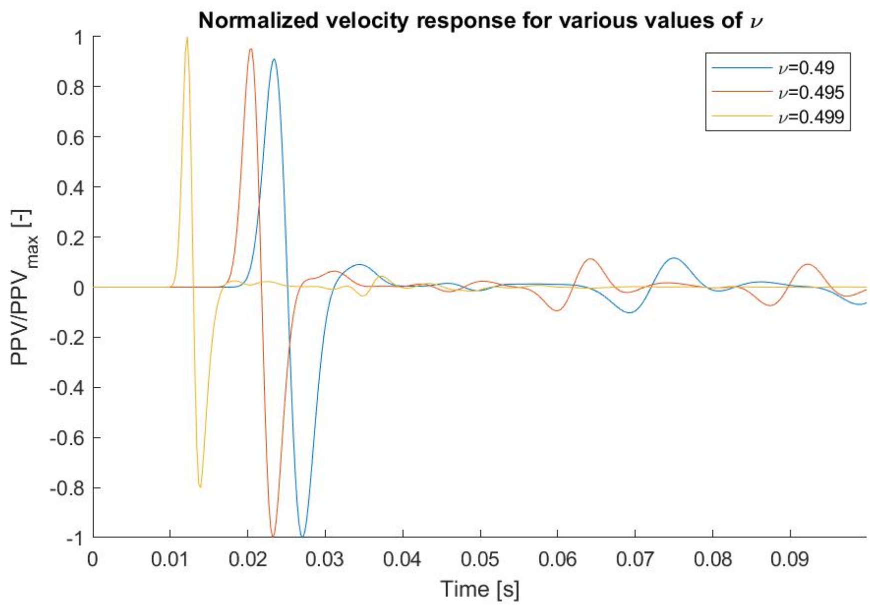

Figure 5.27: Normalized velocity time response of a numerical blast with variation of Poisson's ratio in the clay.

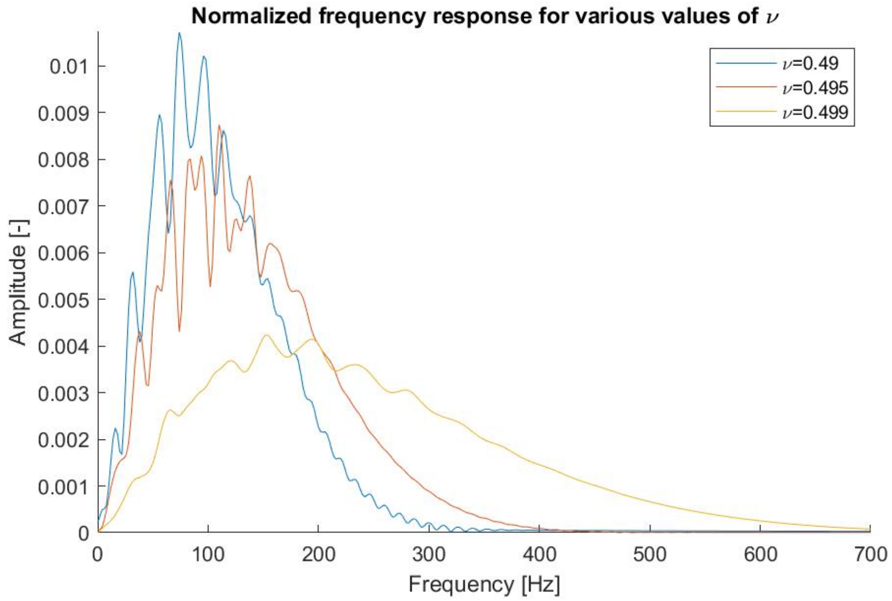

Figure 5.28: Normalized frequency spectrum of a numerical blast with variation of Poisson's ratio in the clay.

5.5.3 Young's modulus

The results for the simulation of a numerical blast where the stiffness variation in the clay are presented here, see Section 4.2.2.3. In Figure 5.29 the velocity response is shown and in Figure 5.30 the frequency spectra is shown.

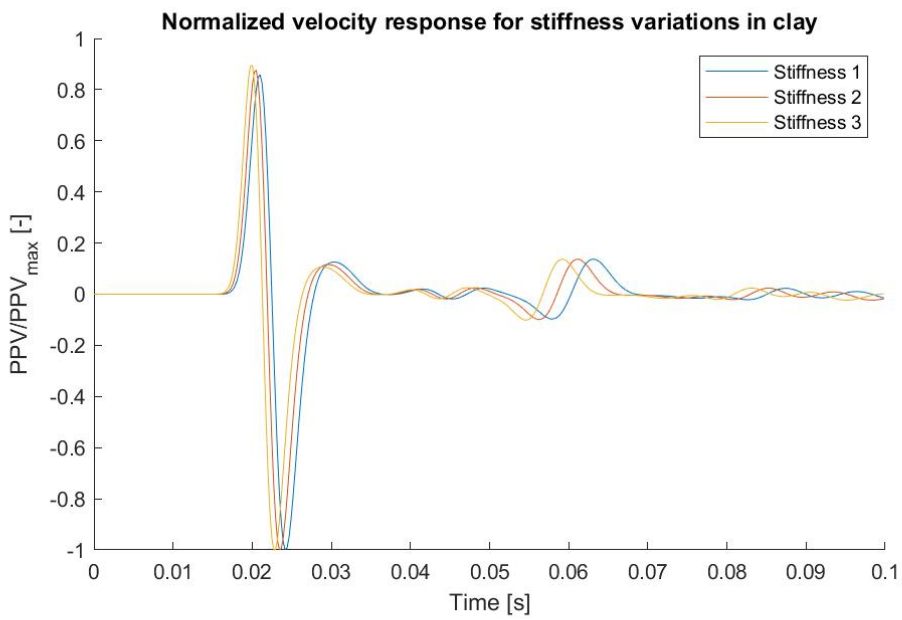

Figure 5.29: Normalized velocity time response of a numerical blast with stiffness variation in the clay. The variation of stiffness is given in Table 4.3.

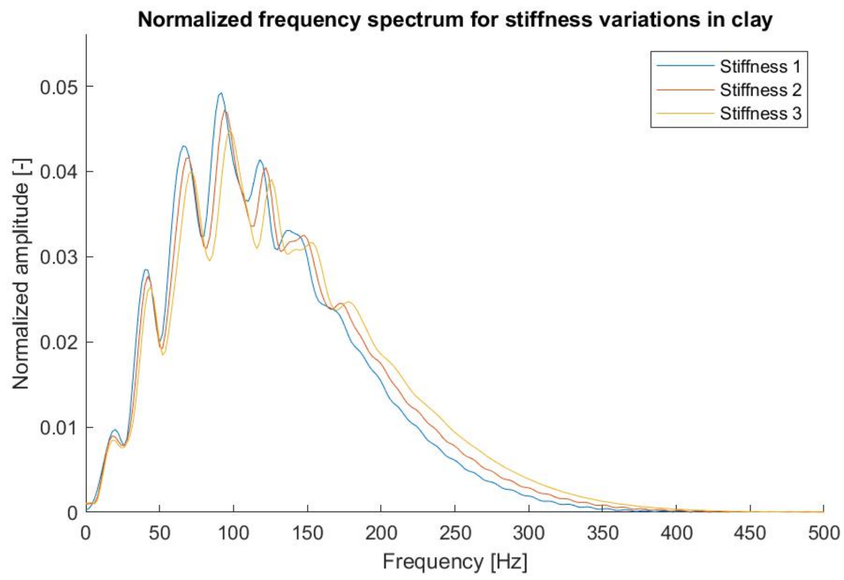

Figure 5.30: Normalized frequency spectrum of a numerical blast with stiffness variation in the clay.The variation of stiffness is given in Table 4.3.

Figures 5.29 and 5.30 shows only a small difference in the velocity- and frequency response, even though Young's modulus has doubled. Thus, the soil's sensitivity for a change in stiffness is not significant.

5.5.4 Overburden surface layer

The results from Section 4.2.2.4 are presented here. The velocity response for overburden surface layers of clay and rock is presented in Figure 5.31 and the frequency spectrum is shown in Figure 5.32.

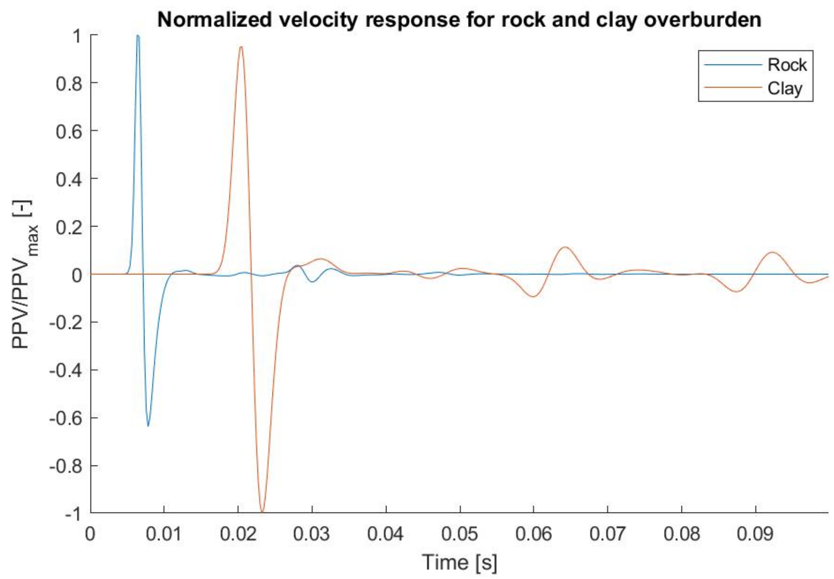

Figure 5.31: Normalized velocity time response of a numerical blast with different overburdening material.

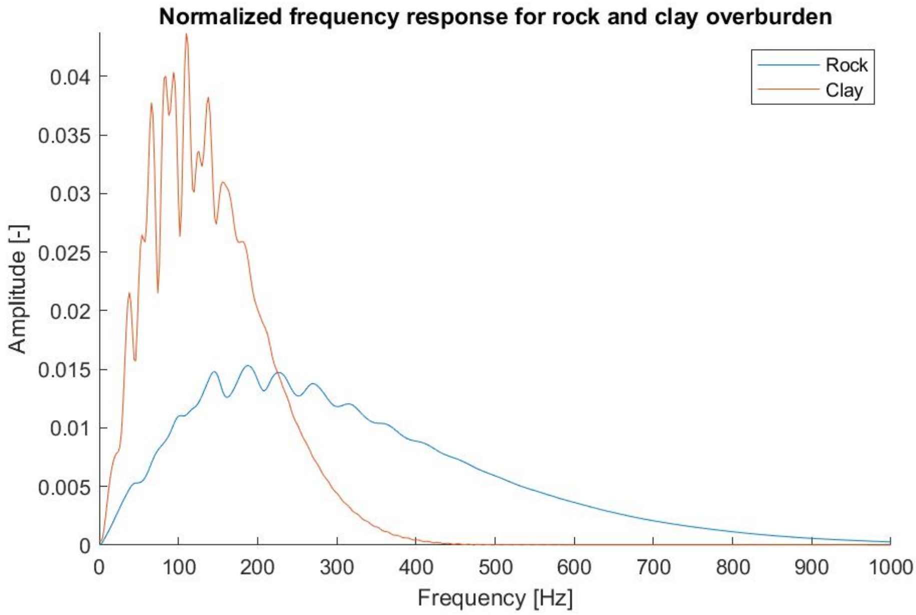

Figure 5.32: Normalized frequency spectrum of a numerical blast with different overburdening material.

The blasts are at the same distance of 34 m but with different overburden domains. One domain consists only of rock and the other domain consists of rock and 30 m clay overburden.

Figure 5.31 shows the difference in wave speed for the domain only consisting of rock and the domain with an overburdening layer of clay. This difference was expected since the wave speed in rock is considerably higher. The frequency response plotted in Figure 5.32 shows a difference between the two blasts. The model with overburdening clay has considerably lower frequencies than the model only consisting of rock. Since buildings are more susceptible to damage at lower frequencies, this would support that the Swedish Standard sets lower guidance levels for clay than for rock.

5.6 Geometrical parameters

In this section, the results for the parametric study of the geometrical parameters are presented.

5.6.1 Distance factor

The results from Section 4.2.3.1 are presented here. The velocity response for a change in distance between the point of measurement and the point of blasting is presented in Figure 5.33 and the frequency spectrum is shown in Figure 5.34.

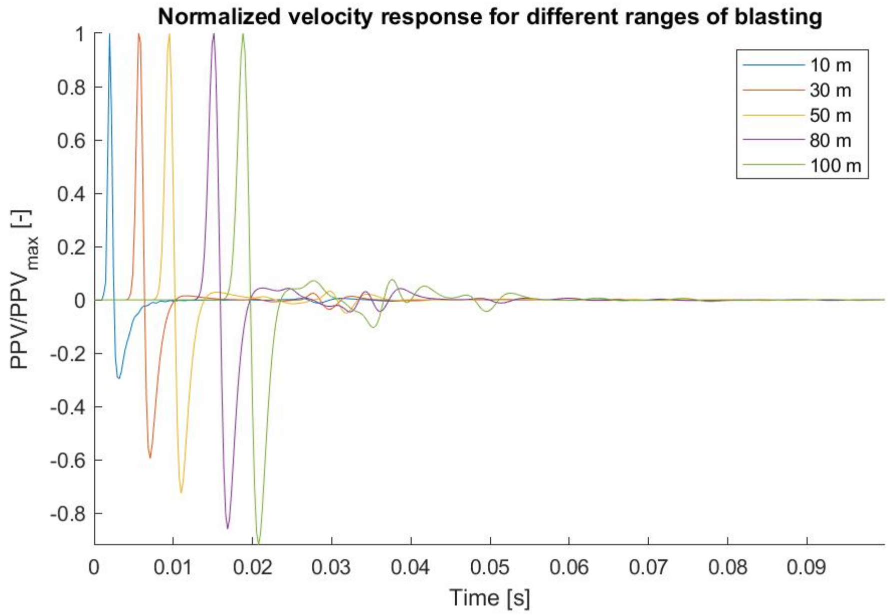

Figure 5.33: Normalized velocity time response of increased range of the blast.

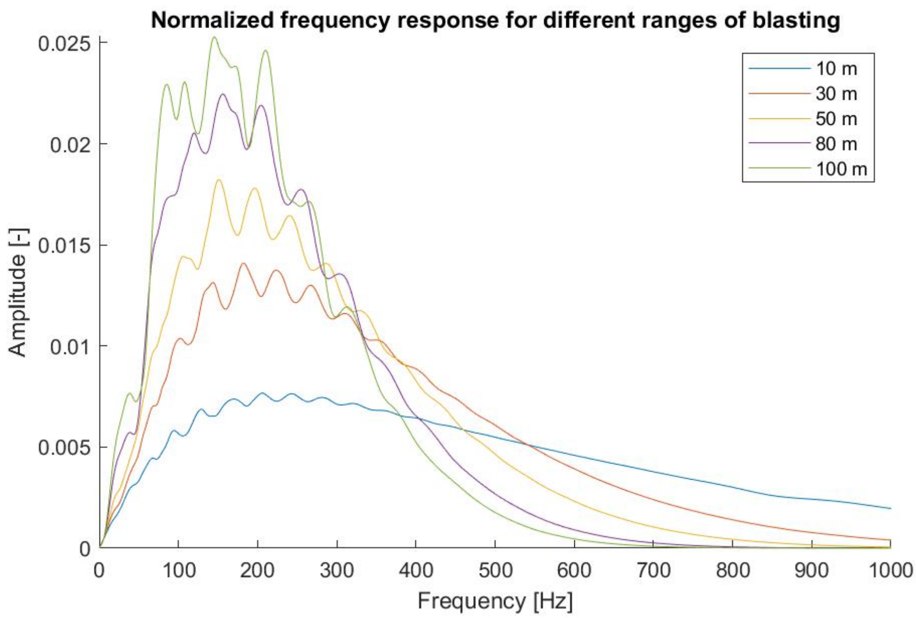

Figure 5.34: Normalized frequency spectrum of increased range of the blast.

The effect on the vibration for an increasing distance between the point of measurement and the blast delays the velocity response, as seen in Figure 5.33. This is a predictable result since it takes more time for the wave to travel to the surface. It is also shown that the negative amplitude in the initial response increases as the distance between the measurement and the blast increases, which is supported by Y. Chenglong & Han (2018).

However, more interesting is the fact that as the distance increased, the frequencies decrease, as seen in Figure 5.34. As mentioned by Yang J et. al (2016), irregularities in the rock dampen higher frequencies and the damping in the model is represented by the Rayleigh damping seen in Figure 5.3. The Rayleigh damping used in the model is a simplification and a more detailed study would give rise to a more exact representation of the damping.

As described in the Swedish Standard in Section 2.5.1 the guidance level is dependent on the distance with the parameter F_d. The guidance level in the Swedish Standard decreased as the range increased. As shown in the study, the frequencies decreases when the distance increases. Thus the range parameter in the Swedish Standard is reasonable, as buildings are more susceptible damage at low frequencies. However, an exact correlation between frequency and the range parameter in the Swedish Standard is dependent on the damping in the material.

5.6.2 Depth of clay

The results for the simulation of a numerical blasts dependency of clay depth from Section 4.2.3.2 is presented here. In Figures 5.35 and 5.36, the velocity response and frequency spectra are shown respectively.

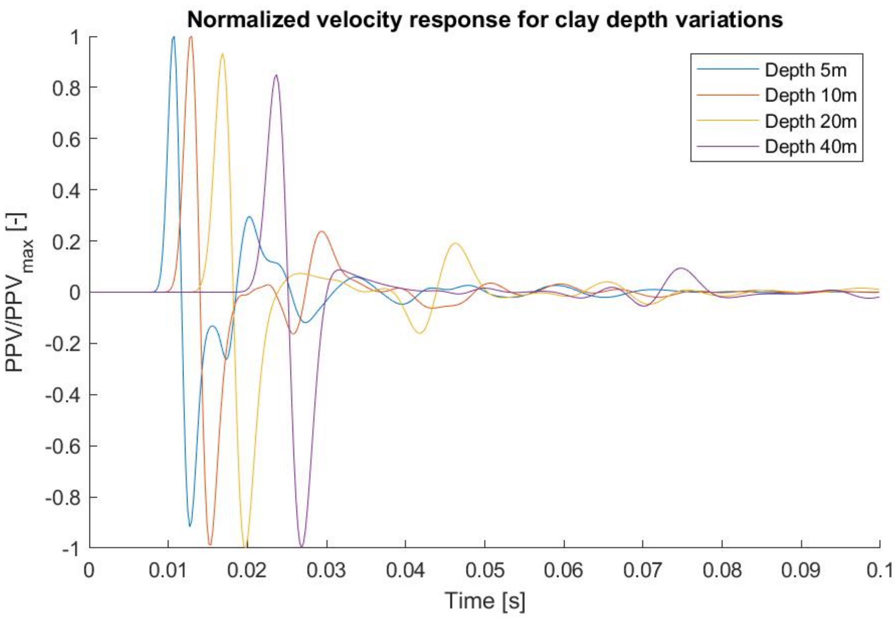

Figure 5.35: Normalized velocity time response of a numerical blast with clay depth variation.

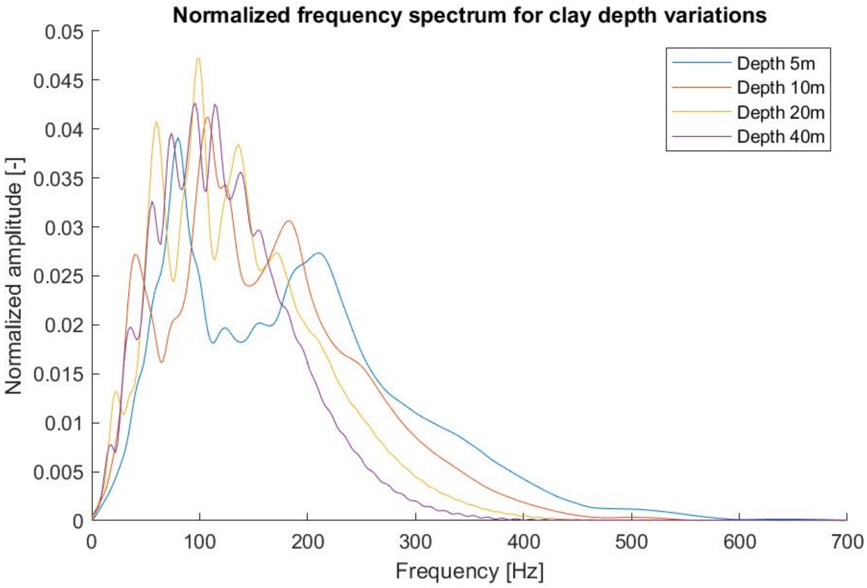

Figure 5.36: Normalized frequency spectrum of a numerical blast with clay depth variation.

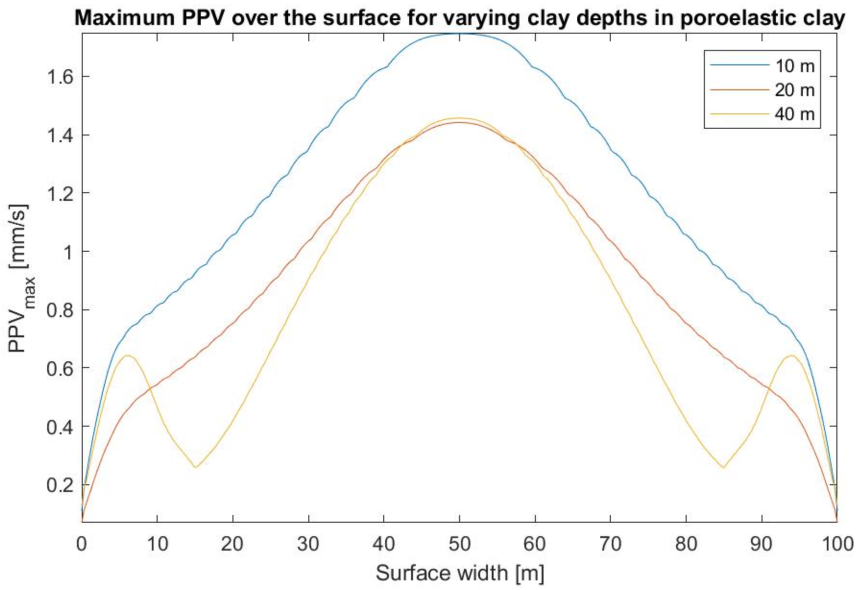

Figure 5.37: The maximum PPV for each point along the surface for different depths of clay.

This study is done since the Swedish Standards does not account for the depth of the overburden material and shows that as the depth of the clay layer increases, the wave is delayed, as seen in Figure 5.35. This is expected due to the higher compression wave speed in rock compared to clay. Furthermore, in the frequency response spectrum, as seen in Figure 5.36, the frequencies move towards the lower range as the distance increase. The change of frequency range shown by this study can be an argument for measurements on the overburden thickness, which is not included in the Swedish Standard.

5.6.3 Angle of incidence

The results from Section 4.2.3.3 are presented here. In Figures 5.38 and 5.39 the vertical velocity and normalized frequency response for three blasts with different angles of incidence are plotted.

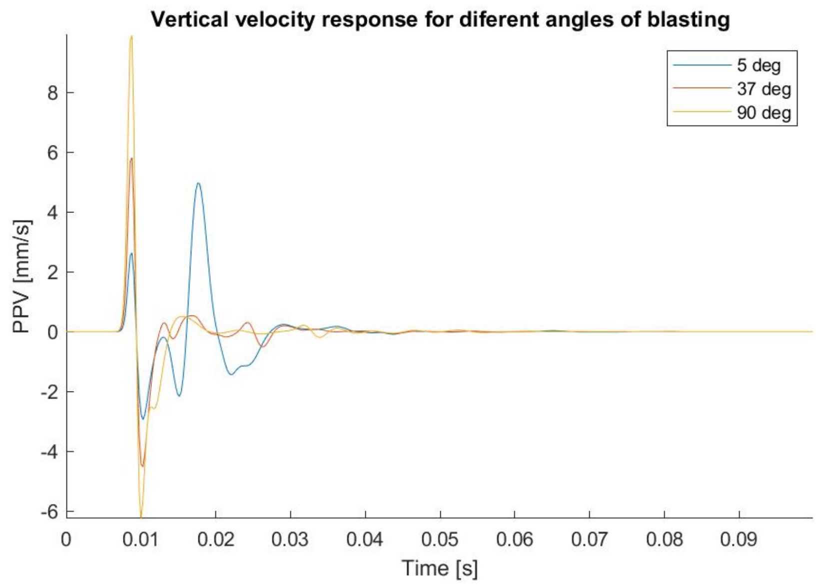

Figure 5.38: Vertical velocity time response for varying angle of incidence of the blast.

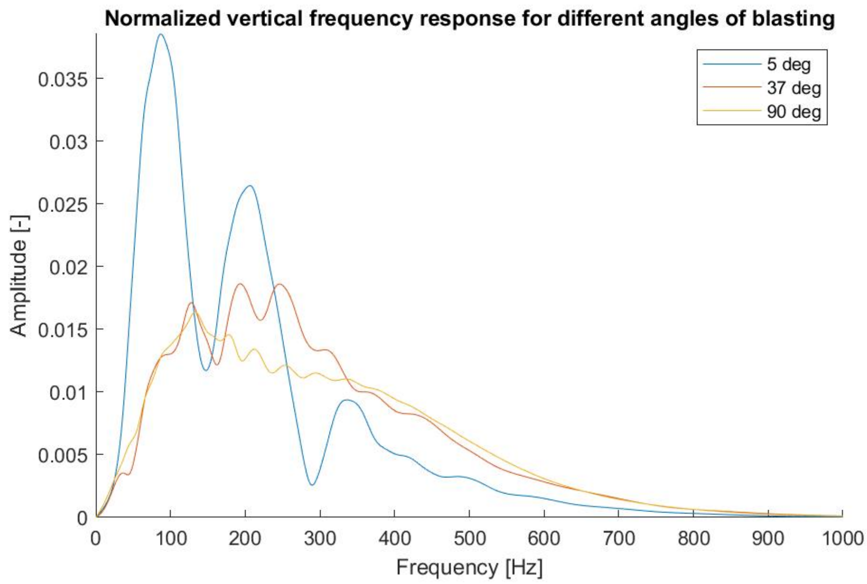

Figure 5.39: Normalized vertical frequency spectrum for varying angle of incidence of the blast.

Figures 5.40 and 5.41 shows the horizontal velocity response and normalized frequency response for blasts with varying incidence of blasting.

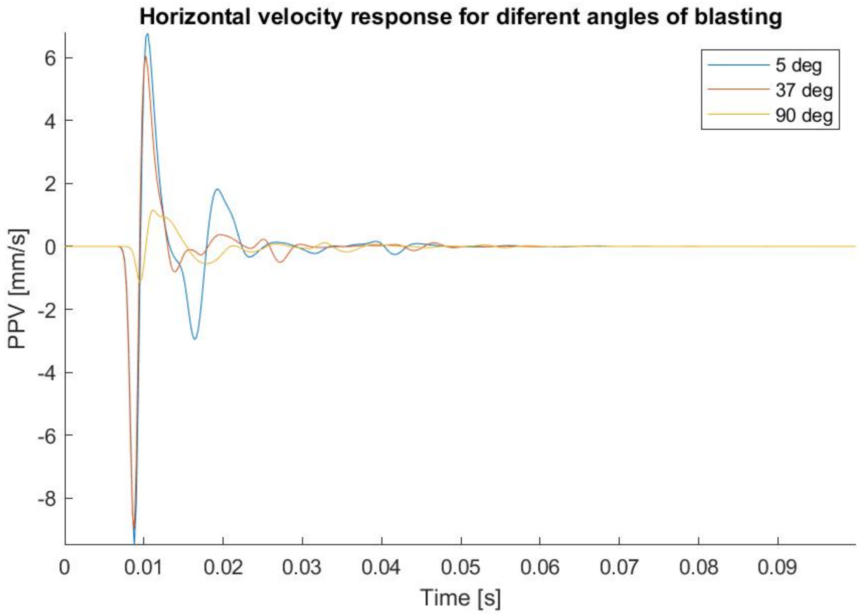

Figure 5.40: Horizontal velocity time response for varying angle of incidence of the blast.

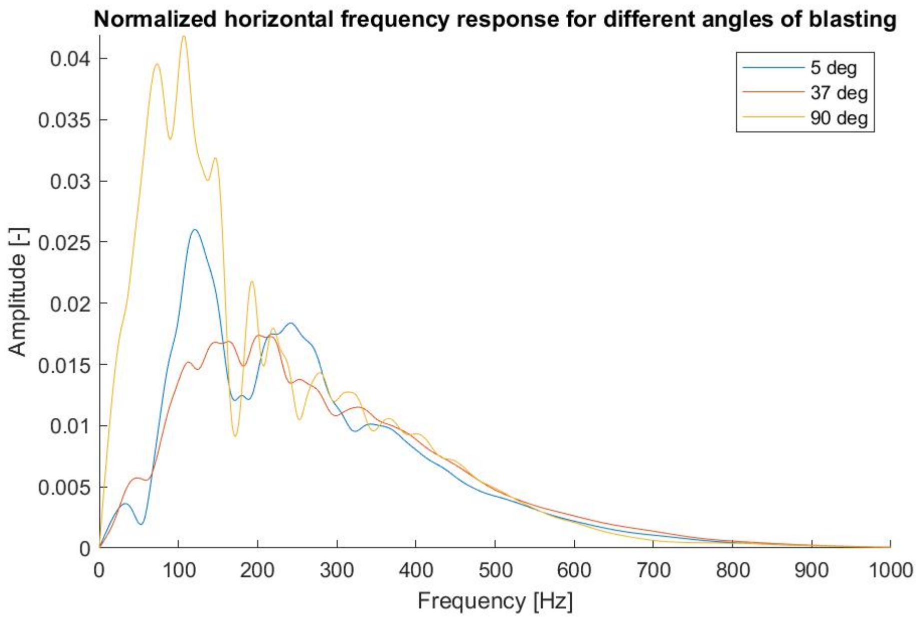

Figure 5.41: Normalized horizontal frequency spectrum for varying angle of incidence of the blast.

With the wave speeds shown in Table 5.1, it is possible to determine that the second wave in Figure 5.42 is the Rayleigh wave.

The vertical and horizontal velocity response for the blast with an incidence angle of 5 degrees are plotted in Figure 5.42. Also plotted in the figure are the time at which the P-wave and the Rayleigh wave arrive at the measure point.

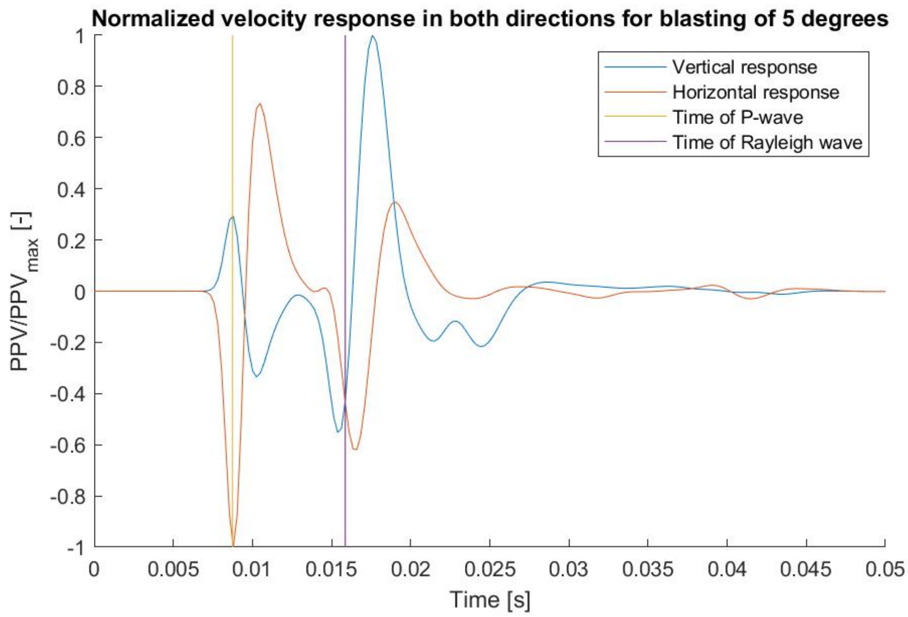

Figure 5.42: Normalized velocity response in both the vertical and the horizontal direction for a blast with an incidence angle of 5 degrees.

For this parametric study, the blast closest to the surface results in the lowest frequencies of the vertical velocity as seen in Figure 5.39. It is also observed that the blast closest to the surface produce two responses in the vertical velocity response, Figure 5.38. As described in section 2.2.4.3, Rayleigh waves occur at free surfaces and are slower than the P-wave. This would suggest that the slow response in Figure 5.38 is a Rayleigh wave. The same response is also observed in the horizontal direction as seen in Figure 5.40. In Figure 5.42 the P-wave can be distinguished for both the vertical and horizontal directions. For the Rayleigh wave however, the velocity response for the different directions does not align. As the horizontal velocity response for the Rayleigh wave is at its maximum, the vertical velocity is zero and vice versa. As is seen in Figure 2.11, the particles in the material move in an elliptic motion with a direction opposite to the direction of the Rayleigh wave. This would explain why there is a phase shift in the vertical and the horizontal response of the Rayleigh wave.

Also seen in the study of the angle of incidence, the horizontal component of the P-wave increases as the angle of incidence decreases, as seen in Figure 5.40. In a similar manner, the vertical response from the P-wave decreases as the angle of incidence decreases, as seen in Figure 5.38. With an angle of incidence of 5 degrees the horizontal component is 3 times larger than the vertical component. However, in Figure 5.38 the largest PPV for the angle of 5 degrees are observed at the Rayleigh wave. From Figure 5.39 it can be observed that the frequency response for the blast containing a Rayleigh wave is lower than the response from the blasts with a dominant P-wave. As the responses of the different blasts vary in this manner, but the guidance levels for all blasts according to the Swedish Standard would be the same, there is an uncertainty of which wave the standard sets guidance levels for.

6
Conclusion

The overburden material has an impact on the frequency response of a blast. The response in clay shows lower frequencies than in rock. According to the Swedish Standard, the uncorrected PPV for clay is lower than in rock. It is thus concluded that there is a connection between the frequency response in the overburden and the uncorrected PPV used in the Swedish Standard.

The results presented in the study shows that a blast will have lower frequencies further away from the measurement point. This concludes that there is a connection between the frequency response for increasing range and the distance parameter in the Swedish Standard, as it lowers the guidance level with regard to distance from the blast.

The velocity and frequency response shows a large sensitivity to small changes in Poisson's ratio and degree of saturation. This would suggest that precise measurements is needed in order to model the real behaviour of the clay. The sensitivity with regard to changes of the degree of saturation argues for the importance of including the effect of the water in the model, which is possible through the poroelastic material model. The vibrations in the soil do not show any significant sensitivity with regard to a change in Young's modulus, as shown in Figures 5.29 and 5.30.

An increased depth of the overburden causes lower frequencies in the vibration from the blast. This shows the importance of measurements on the overburden thickness, as buildings are more susceptible to damage at lower frequencies.

The angle of incidence can determine which wave will be dominant, for a high angle of incidence the P-wave is dominant, whereas for a low angle of incidence the Rayleigh wave is dominant. Since the P- and Rayleigh waves give rise to different frequency and velocity responses, guidance levels may be set differently depending on which is the dominant wave.

The horizontal component of the P-wave increases as the angle of incidence decreases. At an angle of incidence of 5 degrees the horizontal component is larger than the vertical component, making the horizontal vibration dominant. This argues for expanding the Swedish Standard for blasting induced vibration by taking horizontal vibrations into account.

A frequency based analysis generates the possibility to combine distance, overburden, material-, geometrical- and possible unidentified parameters, thus simplifying the method of establishing guidance levels for blasting induced vibrations in the soil structure. However, if Sweden would switch to a frequency based standard, it is important to evaluate the parameters pertaining to vibration sensitivity in buildings.

6.1 Further studies

Establishing a relationship between blasting weight and the blasting function in order to predict the amplitude of the blast.

Increasing the perspective of the study, including a model of frictional soil using an elastic or a poroelastic material model.

Examining the possibility of establishing a damage criteria for buildings affected of blasting induced vibrations, thus creating the possibility to evaluate the parameters F_b, F_m and F_t in the Swedish Standard pertaining to buildings.

Study on the maximum PPV along the surface when the blast is located close to the interface between rock and clay in order to describe the interesting property seen in Figures 5.24 and 5.37.

Studying how cracks in rock, soil layering with different material parameters and piles can act as waveguides and thus increasing the vibrations in buildings.

Bibliography

Ainalis, D et al (2016), Assessing blast source pressure modelling approaches for the numerical simulation of ground vibrations, In *23rd International Congress on Sound and Vibration*. 10-14 July, 2016, Athens.

Antes, O. & Von Estorff, O. (1987), 'On causality in dynamic response analysis by time-dependent boundary element methods', *Earthquake Engineering & Structural Dynamics*, vol 15, nr 7 pp. 865–870.

Biot, M. A. (1956), 'Theory of propagation of elastic waves in a fluid-saturated porous solid. i. low-frequency range', *The Journal of the Acoustical Society of America*, vol 28, nr 2 pp. 168–178.

Bos, L. & Slawinski, M. A. (2010), 'Elastodynamic equations: Characteristics, wavefronts and rays', *he Quarterly Journal of Mechanics and Applied Mathematics*, vol 63, nr 1 pp. 23–38.

Bouzidi, Y. & Schmitt, D. (2009), 'Measurement of the speed and attenuation of the Biot slow wave using a large ultrasonic transmitter', *Journal of Geophysical Research*, vol 114, nr B8, pp. 371–375. DOI: 10.1029/2008JB006018 (2018-04-11).

Chadwick, P. & Borejko, P. (1994), 'Existence and uniqueness of Stoneley waves', *Geophysical Journal International*, vol 118, nr 2 pp. 279–284. DOI: 10.1111/j.1365-246X.1994.tb03960.x (2018-04-28).

Chen, J. (1994), 'Time domain fundamental solution to Biot's complete equations of dynamic poroelasticity Part II: Three-dimensional solution', *International Journal of Solids and Structures*, vol 31, nr 2 pp. 169–202. DOI:10.1016/0020-7683(94)90049-3 (2018-05-21).

Cheng, A. (2016), *Poroelasticity - Theory and Applications of Transport in Porous Media*, [Electronic] Switzerland: Springer International Publishing.

Chertkov, V. & Ravina, I. (1993), 'A time integration algorithm for structural dynamics with improved numerical dissipation: the generalized-α method', *Journal of applied mechanics*, vol 60, nr 2, pp. 371–375. DOI: 10.1115/1.2900803 (2018-04-11).

Chung, J. & Hulbert, G. M. (1999), 'Tortuosity of Crack Networks in Swelling Clay Soils', *Soil Science Society of America*, vol 63, nr 6, pp. 371–375. DOI: 10.2136/sssaj1999.6361523x (2018-05-21).

COMSOL Documentation (n.d), '*Low-Reflecting Boundary Condition*'. COMSOL Documentation, 5.3a (2018-05-17).

Darendeli, M. B. (2001), ' *Development of a new family of normalized modulus reduction and material damping curves* '. The University of Texas, Austin.

D.E. Siskind et. al (1980), *Structure Response and Damage Produced by Ground Vibration From Surface Mine Blasting*, US Bureau of Mines (Report of Investigations 8507).

Dong-Soo, K. & Jin-Sun, L. (2000), 'Propagation and attenuation characteristics of various ground vibrations', *Soil Dynamics and Earthquake Engineering*, vol 19, nr 2, pp. 115–126. DOI: 10.1016/S0267-7261(00)00002-6 (2018-03-13).

Dynamic Viscosity (2015), 'In *A Dictionary of Geology and Earth Sciences*, 4 ed'. http://www.oxfordreference.com (2018-03-20).

Engineering Toolbox (2004), 'Water - dynamic and kinematic viscosity'. https://www.engineeringtoolbox.com (2018-04-20).

Flores-Mendez, E. et al. (2012), 'Rayleigh's, stoneley's, and scholte's interface waves in elastic models using a boundary element method', *Journal of Applied Mathematics*, vol 2012, pp. 15–31. DOI: 10.1155/2012/313207 (2018-05-22).

Geological Survey of Sweden (n.d), '*Kartvisare Lagerobservationer*'. https://apps.sgu.se/kartvisare/kartvisare-lagerobservationer.html (2018-02-21).

Gopalakrishnan, S. (2016), *Wave Propagation in Materials and Structures*, [Electronic] Boca Raton, FL: CRC Press.

Hagedorn, P. (2007), *Vibrations and Waves in Continuous Mechanical Systems*, Chichester, West Sussex: Wiley.

Haigh, S.K. Ghosh, B. M. S. (2005), 'Importance of time step discretisation for non-linear dynamic finite element analysis', *Canadian Geotechnical Journal*, vol 42, nr 3, pp. 957–963. DOI: 10.1139/t05-022 (2018-04-06).

Hall, L. Wersäll, C. (2013), *Markvibrationer: SGF Informationsskrift 1:2012*, Göteborg: Swedish Geotechnical Society. (SGF Informationsskrift 1:2012).

Jern, M. et al. (2013), *Förstudie ny Svensk Standard SS 460 48 66 - Sammanfattning och litteraturstudie*, Sis tk 111 ag 3.

Jueun, K. & Selvadurai, A. (2014), 'Group interaction on vertically loaded piles in saturated poroelastic soil', *Computers and Geotechnics*, vol 56 pp. 1 – 10.

Jueun, K. & Selvadurai, A. (2016), 'A note on the consolidation settlement of a rigid circular foundation on a poroelastic halfspace', *International Journal for Numerical and Analytical Methods in Geomechanics*, vol 40, nr 14 pp. 2003–2016.

Khandelwal, M. & Saadat, M. (2015), 'A dimensional analysis approach to study blast-induced ground vibration', *Rock Mechanics and Rock Engineering*, vol 48, nr 2, pp. 727—-735. DOI: 10.1007/s00603-014-0604-y (2018-02-26).

Knappett, J. Craig, R. F. (2012), *Craig's soil mechanics*, 8th ed. Abingdon, Oxon: Spon Press.

Kudarova, A. (2016), ' *Effective models for seismic wave propagation in porous media* '. Delft university of technology, Netherlands.

Lanari, M. & Fakhimi, A. (2011), 'Numerical study of contributions of shock wave and gas penetration toward induced rock damage during blasting', *Computational Particle Mechanics*, vol 2, nr 2 pp. 440–448. DOI: 10.1007/s40571-015-0053-8 (2018-04-24).

Langefors, U. Kihlström, B. (1978), *The Modern Technique of Rock Blasting*, 3th ed. New York: Wiley.

Larsson, R. (2008), *Jords egenskaper*, Swedish Geotechnical Institute. (SGI Information 1).

Lu, W et al. (2012), 'An introduction to Chinese safety regulations for blasting vibration', *Environmental Earth Sciences*, vol 67, nr 7, pp. 1951–1959. DOI: 10.1007/s12665-012-1636-9 (2018-02-13).

Lubis, A. M., Hashima, A. & Sato, T. (2012), 'Analysis of afterslip distribution following the 2007 september 12 southern sumatra earthquake using poroelastic and viscoelastic media', *Geophysical Journal International*, vol 192, nr 1 pp. 18–37. DOI: 10.1093/gji/ggs020 (2018-05-31).

Möller, B. et al. (2017), *Geodynamik i pratiken*, Swedish Geotechnical Institute. (SGI Information 17).

Olsson, P. (1990), *Svängningar och Ljudutbredning*, Gothenburg: Avdelning Mekanik CTH.

Papagiannopoulos, G., Beskos, D. & Triantafyllidis, T. (2015), 'Seismic pressures on rigid cantilever walls retaining linear poroelastic soil: An exact solution', *Soil Dynamics and Earthquake Engineering*, vol 77 pp. 208 – 219.

Persson, P.-A., Holmberg, R. & Lee, J. (1993), *Rock Blasting and Explosive Engineering*, [Electronic] Boca Raton, FL: CRC Press.

Pisani, L. (2011), 'Simple Expression for the Tortuosity of Porous Media', *Transport in Porous Media*, vol 88, nr 2 pp. 193–203. DOI:10.1007/s11242-011-9734-9 (2018-05-21).

Rao, S. S. (2007), *Vibration of continuous systems*, Hoboken, New Jersey: Wiley.

Sällfors, G. (2001), *Geoteknik: jordmateriallära*, 3rd ed. Göteborg: Vasastadens Tryckeri.

Sazid, M. & Singh, T. N. (2013), 'Two-dimensional dynamic finite element simulation of rock blasting', *Arabian Journal of Geosciences*, vol 6, nr 10, pp. 3703–3708. DOI: 10.1007/s12517-012-0632-4 (2018-02-08).

Sebastian, R. Siltharam, T. (2015), 'Long Wavelength Propagation of Elastic Waves Across Frictional and Filled Rock Joints with Different Orientations: Experimental Results', *Geotechnical and Geological Engineering*, vol 33, nr 4, pp. 923–934. DOI: 10.1007/s10706-015-9874-8 (2018-03-28).

Semblat, J. F. (2015), 'Modeling Seismic Wave Propagation and Amplification in 1D/2D/3D Linear and Nonlinear Unbounded Media', *International Journal of Geomechanics*, vol 11, nr 6 pp. 440–448. DOI: 10.1061/(ASCE)GM.1943-5622.0000023 (2018-02-20).

Sheng-Huoo, N. & Shen-Haw, J. (2007), 'Determining Rayleigh damping parameters of soils for finite element analysis', *International Journal for Numerical and Analytical methods in Geomechanics*, vol 31, nr 10, pp. 1239–1255. DOI: 10.1002/nag.598 (2018-03-29).

Swedish Standard Institute (2011), *Vibration and shock - Guidance levels for blasting-induced vibration in buildings*, Swedish Standard (SS 4604866:2011).

Swedish Standards Instiute (n.d), '*What is a standard?*'. https://www.sis.se (2018-03-26).

Thelin, C. (2009), *Sprängningsinducerade vibrationer - Kyrkorna och citybanan*, Växjö: Tyréns.

Trafikverket (2016), 'The west swedish agreement – initiatives for a sustainable west sweden'. https://www.trafikverket.se (2018-01-25).

Trafikverket (n.d), 'The west swedish agreement'. http://www.vastsvenskapaketet.se/ (2018-01-25).

Verruijt, A. (2010), *Soil Mechanics*, Delft.

V.W. L et. al (2014), 'Scattering and diffraction of earthquake motions in irregular elastic layers, I: Love and SH waves', *Soil Dynamics and Earthquake Engineering*, vol 66 pp. 125– 134. DOI: 10.1016/j.soildyn.2014.07.002 (2018-04-23).

Wang, H. (2000), *Theory of linear poroelasticity with applications to geomechanics and hydrogeology*, [Electronic] Princeton, New Jersey: Princeton University Press.

Wersäll, C. et al. (2008), 'Riskhantering vid sprängningsarbeten', *Bygg Teknik,* January, pp. 52–60. https://issuu.com/byggteknikforlaget/docs/1-08/52 (2018-01-25).

Wersäll, C. et al. (2009), 'Planering och övervakning i bebyggda områden', *Bygg Teknik,* January, pp. 64–74. https://issuu.com/byggteknikforlaget/docs/1-09/72 (2018-01-25).

Xia, X et al. (2018), 'A case study on the cavity effect of a water tunnel on the ground vibrations induced by excavating blasts', *Tunnelling and Underground Space Technology*, vol 71, pp. 292–297. DOI: 10.1016/J.TUST.2017.08.026 (2018-02-13).

Y. Chenglong, Z. W. & Han, W. (2018), 'A prediction model for frequency spectrum of blast-induced seismicwave in viscoelastic medium', *Geophysical Prospecting*, vol 66 p. 87–98. DOI: 10.1111/1365-2478.12601 (2018-05-11).

Yang J et. al (2016), 'A Study on the Vibration Frequency of Blasting Excavation in Highly Stressed Rock Masses', *Rock Mechanics and Rock Engineering*, vol 49, nr 7 pp. 2825—-2843. DOI: 0.1007/s00603-016-0964-6 (2018-04-27).

Yu, Z., Yixian, X. & Jianghai, X. (2012), 'Wave fields and spectra of rayleigh waves in poroelastic media in the exploration seismic frequency band', *Advances in Water Resources*, vol 49, pp. 62–71. DOI: 10.1016/j.advwatres.2012.05.014 (2018-05-22).

Appendices

A Material data in Gothenburg

Table A.1: Material parameters at Liseberg

MATERIAL PARAMETERS AT LISEBERG											
Depth [m]	Level [m]	Soil material	Density [t/m^3]	Natural water content [%]	Liquid limit [%]	Effective stress σ'_c [kPa]	Shear stiffness Cu [kPa]	E_{50} empirical TK Geo [MPa]	G empirical TK Geo [MPa]	Initial permeability [m^2/s]	Inner frictional angle
0	2	Fill	1,9	20			-				35°
1	1		1,9	20			-				
1	1		1,9	20			-				
1,5	0,5		1,9	20			-				
1,5	0,5	Muddy clay	1,5	89,3	90	50	14	3,5	7,8	2,00E-09	30°
4	-2	(highly plastic)	1,5	95,5	100	50	14	3,5	7,1	2,00E-09	
4	-2		1,5	95,5	100	50	14	3,5	7,1	2,00E-09	
5	-3		1,5	98	104	50	14	3,5	6,8	2,00E-09	
5	-3		1,45	98	104	50	14	3,5	6,8	2,00E-09	
7	-5		1,45	103	112	56	14	3,5	6,3	2,00E-09	
7	-5		1,45	103	112	56	14	3,5	6,3	2,00E-09	
10	-8		1,45	94	95,5	65	17,6	4,4	9,3	2,00E-09	
10	-8		1,5	94	95,5	65	17,6	4,4	9,3	2,00E-09	
15	-13		1,5	94	68	95	23,6	5,9	17,5	2,00E-09	
15	-13		1,5	94	68	95	23,6	5,9	17,5	2,00E-09	
17	-15		1,5	94	57	107	26	6,5	23	2,00E-09	
17	-15		1,5	94	57	107	26	6,5	23	2,00E-09	
19	-17		1,5	94	46	127	28,4	7,1	31,1	2,00E-09	
19	-17	Frictional material	1,9				-	20	27		39°
20	-18		1,9				-	20	27		
20	-18		1,9				-	20	27		
21	-19		1,9				-	20	27		
23	-21		1,9				-	20	27		
25	-23		1,9				-	20	27		
27	-25		1,9				-	20	27		
29	-27		1,9				-	20	27		

Table A.2: Material parameters at Haga

MATERIAL PARAMETERS AT HAGA

Depth	Weight density γ	Saturated weight density γ_m	Natural water content w_n	Liquid limit w_L	Inner frictional angle ϕ'	Shear stiffness c_u	Effective stress σ'_c	E_{50} Empirical TK Geo (50 x σ'_c)	G_0 Empirical TK Geo (504 x c_u / w_L)
[m]	[kN/m^3]	[kN/m^3]	[%]	(%)	(º)	(kPa)	(kPa)	(kPa)	(kPa)
3,0	18,0	21,0			38,0				
2,0	18,0	21,0			38,0				
2,0	18,0	21,0			35,0				
1,0	18,0	21,0			35,0				
1,0	16,2	16,2	70,0	75,0		22,0	95,0	4750	14784
-4,0	16,2	16,2	70,0	75,0		22,0	95,0	4750	14784
-4,0	16,2	16,2	70,0	75,0		22,0	95,0	4750	14784
-19,0	16,2	16,2	70,0	75,0		41,5	188,0	9400	27888
-19,0	16,2	16,2	70,0	75,0		41,5	188,0	9400	27888
-21,0	16,2	16,2	66,7	75,0		44,1	200,4	10020	29635
-21,0	16,2	16,2	66,7	75,0		44,1	200,4	10020	29635
-25,0	16,2	16,2	60,1	67,4		49,3	228,0	11400	36865
-30,0	16,2	16,2	51,9	57,9		55,8	262,5	13125	48572
-37,0	18,6	18,6	40,3	44,6		64,9	310,8	15540	73340
-40,0	19,1	19,1	40,3	44,6		68,8	331,5	16575	77747
-45,0	19,1	19,1	40,3	44,6		75,3	366,0	18300	85092
-50,0	19,1	19,1	40,3	44,6		81,8	400,5	20025	92438

.

B Rayleigh wave speed in rock

Rayleigh wave speed calculation

Calculate $\kappa^2 = c_P^2 / c_S^2$ for rock with

In[66]:=
```
Em = 60 × 10^9; ρ = 2600; ν = 0.25;
κ = (Em / (ρ * (1 + ν)) * ((1 - ν) / (1 - 2 * ν))) / (Em / (2 * ρ * (1 + ν)))
```
Out[67]= 3.

Define Equation 2.48

In[68]:=
```
F[ξ_] = (ξ^6 - 8 * ξ^4 + 8 * (3 - 2 / κ) * ξ^2 - 16 * (1 - 1 / κ))
```
Out[68]= $-10.6667 + 18.6667\,\xi^2 - 8\,\xi^4 + \xi^6$

In[69]:=
```
Simplify[Solve[F[ξ] == 0, ξ]]
```
Out[69]= {{ξ → -2.}, {ξ → -1.77615}, {ξ → -0.919402}, {ξ → 0.919402}, {ξ → 1.77615}, {ξ → 2.}}

Use conditions 2.49

In[70]:=
```
ξ < 1
```
Out[70]= ξ < 1

Resulting in

In[71]:=
```
cR = 0.9546954342732867` * cS //. cS → √((Em / (2 * ρ * (1 + ν))))
```
Out[71]= 2900.57

C Poroelastic wave speed

Calculation for poroelastic wavespeeds

Defining input data for the P-waves

In[73]:= $\lambda = 3.7\times10^{9}$; $M = 1/(3.5*10^{-10})$; $G = 37.5\times10^{6}$; $\alpha = 1$; $\rho = 1700$;
$\rho f = 1190$;
$\rho p = \frac{\rho f}{0.7}$;

Defining material matrices

In[75]:= Styv = $\begin{pmatrix} \lambda + 2G & \alpha M \\ \alpha M & M \end{pmatrix}$; Tung = $\begin{pmatrix} \rho & \rho f \\ \rho f & \rho p \end{pmatrix}$; Seg = $\begin{pmatrix} 0 & 0 \\ 0 & \frac{1}{\kappa} \end{pmatrix}$;

Calculating wavespeeds and diagonalize the wavespeed matrix

In[76]:=
```
Hast = Simplify[Inverse[Tung].Styv];
eig = Eigensystem[Hast];
P = Transpose[Part[eig, 2]];
PInv = Inverse[P];
diag = PInv.Hast.P;
```

Extracting the wave speeds

In[81]:=
```
vp1 = Sqrt[Part[diag, 1, 1]]
vp2 = Sqrt[Part[diag, 2, 2]]
```

Out[81]= 1497.49

Out[82]= 890.747

Defining input data for the S-wave

In[83]:= $G = 37.5\times10^{6}$; $\alpha = 1$; $\rho = 1700$; $\rho f = 1190$; $\rho p = \frac{\rho f}{0.7}$;

Defining material matrices

In[84]:= Styv = $\begin{pmatrix} G & 0 \\ 0 & 0 \end{pmatrix}$; Tung = $\begin{pmatrix} \rho & \rho f \\ \rho f & \rho p \end{pmatrix}$; Seg = $\begin{pmatrix} 0 & 0 \\ 0 & \frac{1}{\kappa} \end{pmatrix}$;

Calculating wavespeeds and diagonalize the wavespeed matrix

In[85]:=
```
Hast = Simplify[Inverse[Tung].Styv];
eig = Eigensystem[Hast];
P = Transpose[Part[eig, 2]];
PInv = Inverse[P];
diag = PInv.Hast.P;
```

Extracting the wave speed

In[90]:=
```
vp1 = Sqrt[Part[diag, 1, 1]]
```

Out[90]= 207.973

D Surface wave between two layers

Calculation for surface waves between layers

Defining the wavenumbers for the P waves and S waves above (subscript O) and below (subscript N) the interface of the solids.

$$h_{Op}=\sqrt{q^2-\frac{\omega^2}{cOp^2}}\ ;\ h_{Os}=\sqrt{q^2-\frac{\omega^2}{cOs^2}}\ ;\ h_{Np}=\sqrt{q^2-\frac{\omega^2}{cNp^2}}\ ;\ h_{Ns}=\sqrt{q^2-\frac{\omega^2}{cNs^2}}\ ;$$

Defining the displacements fields both above and below with the same subscripts as before

$$\texttt{uO[x\_, y\_, t\_]} := A_{Op}\,\{i\,q,\ -h_{Op}\}\,e^{i\,q\,x-h_{Op}\,y-i\,t\,\omega}+A_{Os}\,\{-h_{Os},\ -i\,q\}\,e^{i\,q\,x-h_{Os}\,y-i\,t\,\omega};$$
$$\texttt{uN[x\_, y\_, t\_]} := A_{Np}\,\{i\,q,\ h_{Np}\}\,e^{i\,q\,x+h_{Np}\,y-i\,t\,\omega}+A_{Ns}\,\{h_{Ns},\ -i\,q\}\,e^{i\,q\,x+h_{Ns}\,y-i\,t\,\omega};$$

Calculating the stress sensor for the material above and below

$$\begin{aligned}\texttt{tO[U\_]} := \{&\mu O\,(\partial_x(\{0,1\}.U)+\partial_y(\{1,0\}.U)),\\ &(\lambda O+2\,\mu O)\,(\partial_x(\{1,0\}.U)+\partial_y(\{0,1\}.U))-2\,\mu 0\,\partial_x(\{1,0\}.U)\};\\ \texttt{tN[U\_]} := \{&\mu N\,(\partial_x(\{0,1\}.U)+\partial_y(\{1,0\}.U)),\\ &(\lambda N+2\,\mu N)\,(\partial_x(\{1,0\}.U)+\partial_y(\{0,1\}.U))-2\,\mu N\,\partial_x(\{1,0\}.U)\};\end{aligned}$$

and rewriting the stress tensor in terms of wavespeeds:

$$\begin{aligned}\texttt{tOc[U\_]} := \rho 0\,\{&cOs^2\,(\partial_x(\{0,1\}.U)+\partial_y(\{1,0\}.U)),\\ &cOp^2\,(\partial_x(\{1,0\}.U)+\partial_y(\{0,1\}.U))-2\,cOs^2\,\partial_x(\{1,0\}.U)\};\\ \texttt{tNc[U\_]} := \rho N\,\{&cNs^2\,(\partial_x(\{0,1\}.U)+\partial_y(\{1,0\}.U)),\\ &cNp^2\,(\partial_x(\{1,0\}.U)+\partial_y(\{0,1\}.U))-2\,cNs^2\,\partial_x(\{1,0\}.U)\};\end{aligned}$$

The amplitudes of the displacment fields are removed and the boundary conditions at the surface are introduced

$$\begin{aligned}\texttt{koeffc} = \texttt{Simplify}\Big[\Big\{&\\ &\{\{1,0\}.\{i\,q,\ -h_{Op}\}\,e^{i\,q\,x-h_{Op}\,y-i\,t\,\omega},\ \{1,0\}.\{-h_{Os},\ -i\,q\}\,e^{i\,q\,x-h_{Os}\,y-i\,t\,\omega},\\ &\ -\{1,0\}.\{i\,q,\ h_{Np}\}\,e^{i\,q\,x+h_{Np}\,y-i\,t\,\omega},\ -\{1,0\}.\{h_{Ns},\ -i\,q\}\,e^{i\,q\,x+h_{Ns}\,y-i\,t\,\omega}\},\\ &\{\{0,1\}.\{i\,q,\ -h_{Op}\}\,e^{i\,q\,x-h_{Op}\,y-i\,t\,\omega},\ \{0,1\}.\{-h_{Os},\ -i\,q\}\,e^{i\,q\,x-h_{Os}\,y-i\,t\,\omega},\\ &\ -\{0,1\}.\{i\,q,\ h_{Np}\}\,e^{i\,q\,x+h_{Np}\,y-i\,t\,\omega},\ -\{0,1\}.\{h_{Ns},\ -i\,q\}\,e^{i\,q\,x+h_{Ns}\,y-i\,t\,\omega}\},\\ &\{\{1,0\}.\texttt{tOc}[\{i\,q,\ -h_{Op}\}\,e^{i\,q\,x-h_{Op}\,y-i\,t\,\omega}],\ \{1,0\}.\texttt{tOc}[\{-h_{Os},\ -i\,q\}\,e^{i\,q\,x-h_{Os}\,y-i\,t\,\omega}],\\ &\ -\{1,0\}.\texttt{tNc}[\{i\,q,\ h_{Np}\}\,e^{i\,q\,x+h_{Np}\,y-i\,t\,\omega}],\\ &\ -\{1,0\}.\texttt{tNc}[\{h_{Ns},\ -i\,q\}\,e^{i\,q\,x+h_{Ns}\,y-i\,t\,\omega}]\},\\ &\{\{0,1\}.\texttt{tOc}[\{i\,q,\ -h_{Op}\}\,e^{i\,q\,x-h_{Op}\,y-i\,t\,\omega}],\ \{0,1\}.\texttt{tOc}[\{-h_{Os},\ -i\,q\}\,e^{i\,q\,x-h_{Os}\,y-i\,t\,\omega}],\\ &\ -\{0,1\}.\texttt{tNc}[\{i\,q,\ h_{Np}\}\,e^{i\,q\,x+h_{Np}\,y-i\,t\,\omega}],\ -\{0,1\}.\texttt{tNc}[\{h_{Ns},\ -i\,q\}\,e^{i\,q\,x+h_{Ns}\,y-i\,t\,\omega}]\}\\ &\Big\}\Big];\end{aligned}$$

The wavespeed of the Rayliegh are introduced as v. As the speed of the wave is the same along the surface, the coordinates can be set to 0 and since it is not dependent on the frequency it is set to 1.

$$\texttt{koeffc1} = \texttt{koeffc} \ \texttt{//.}\ \left\{q\to\frac{\omega}{v},\ y\to 0,\ t\to 0,\ x\to 0,\ \omega\to 1\right\};$$

Collecting the wavespeed terms.

Printed by Wolfram Mathematica Student Edition

```
ekvVL = Collect[FullSimplify[Det[koeffc1]], {Sqrt[-1/cNp^2 + 1/v^2], Sqrt[-1/cOp^2 + 1/v^2]}]
```

$$\text{ekvVL} = \text{Collect}\left[\text{FullSimplify}[\text{Det}[\text{koeffc1}]], \left\{\sqrt{-\frac{1}{\text{cNp}^2}+\frac{1}{v^2}}, \sqrt{-\frac{1}{\text{cOp}^2}+\frac{1}{v^2}}\right\}\right]$$

$$\frac{1}{v^6}\left(-4\,\text{cOs}^4\rho 0^2 + 4\,\text{cOs}^2 v^2 \rho 0^2 - v^4 \rho 0^2 + 8\,\text{cNs}^2\text{cOs}^2 \rho 0\,\rho N - 4\,\text{cNs}^2 v^2 \rho 0\,\rho N - 4\,\text{cOs}^2 v^2 \rho 0\,\rho N + 2 v^4 \rho 0\,\rho N - 4\,\text{cNs}^4 \rho N^2 + 4\,\text{cNs}^2 v^2 \rho N^2 - v^4 \rho N^2\right) +$$

$$\frac{1}{v^6}\sqrt{-\frac{1}{\text{cOp}^2}+\frac{1}{v^2}}\left(4\,\text{cOs}^4\sqrt{-\frac{1}{\text{cOs}^2}+\frac{1}{v^2}}\,v^2\rho 0^2 - 8\,\text{cNs}^2\text{cOs}^2\sqrt{-\frac{1}{\text{cOs}^2}+\frac{1}{v^2}}\,v^2\rho 0\,\rho N + 4\,\text{cOs}^2\sqrt{-\frac{1}{\text{cOs}^2}+\frac{1}{v^2}}\,v^4\rho 0\,\rho N + \sqrt{-\frac{1}{\text{cNs}^2}+\frac{1}{v^2}}\,v^6\rho 0\,\rho N + 4\,\text{cNs}^4\sqrt{-\frac{1}{\text{cOs}^2}+\frac{1}{v^2}}\,v^2\rho N^2 - 4\,\text{cNs}^2\sqrt{-\frac{1}{\text{cOs}^2}+\frac{1}{v^2}}\,v^4\rho N^2 + \sqrt{-\frac{1}{\text{cOs}^2}+\frac{1}{v^2}}\,v^6\rho N^2\right) + \sqrt{-\frac{1}{\text{cNp}^2}+\frac{1}{v^2}}$$

$$\left(\frac{1}{v^6}\left(4\,\text{cOs}^4\sqrt{-\frac{1}{\text{cNs}^2}+\frac{1}{v^2}}\,v^2\rho 0^2 - 4\,\text{cOs}^2\sqrt{-\frac{1}{\text{cNs}^2}+\frac{1}{v^2}}\,v^4\rho 0^2 + \sqrt{-\frac{1}{\text{cNs}^2}+\frac{1}{v^2}}\,v^6\rho 0^2 - 8\,\text{cNs}^2\text{cOs}^2\sqrt{-\frac{1}{\text{cNs}^2}+\frac{1}{v^2}}\,v^2\rho 0\,\rho N + 4\,\text{cNs}^2\sqrt{-\frac{1}{\text{cNs}^2}+\frac{1}{v^2}}\,v^4\rho 0\,\rho N + \sqrt{-\frac{1}{\text{cOs}^2}+\frac{1}{v^2}}\,v^6\rho 0\,\rho N + 4\,\text{cNs}^4\sqrt{-\frac{1}{\text{cNs}^2}+\frac{1}{v^2}}\,v^2\rho N^2\right) + \frac{1}{v^6}\sqrt{-\frac{1}{\text{cOp}^2}+\frac{1}{v^2}}\left(-4\,\text{cOs}^4\sqrt{-\frac{1}{\text{cNs}^2}+\frac{1}{v^2}}\sqrt{-\frac{1}{\text{cOs}^2}+\frac{1}{v^2}}\,v^4\rho 0^2 + 8\,\text{cNs}^2\text{cOs}^2\sqrt{-\frac{1}{\text{cNs}^2}+\frac{1}{v^2}}\sqrt{-\frac{1}{\text{cOs}^2}+\frac{1}{v^2}}\,v^4\rho 0\,\rho N - 4\,\text{cNs}^4\sqrt{-\frac{1}{\text{cNs}^2}+\frac{1}{v^2}}\sqrt{-\frac{1}{\text{cOs}^2}+\frac{1}{v^2}}\,v^4\rho N^2\right)\right)$$

Introducing the material parameters of the wave and plotting the absolute value of the wavespeed.

```
λO = 5.77 * 10^9; μO = 5.83 * 10^7; cOp = 1837; cNp = 5262; cOs = 184;
cNs = 3038; λN = 2.4 * 10^10; μN = 2.4 * 10^10;
ρ0 = μO / cOs^2;
ρN = μN / cNs^2;
```

```
Plot[Abs[ekvVL], {v, 0, 10 000}, AxesLabel → {"Wave Speed [m/s]"},
 PlotLabel → "Solutions for Interface Wave"]
```

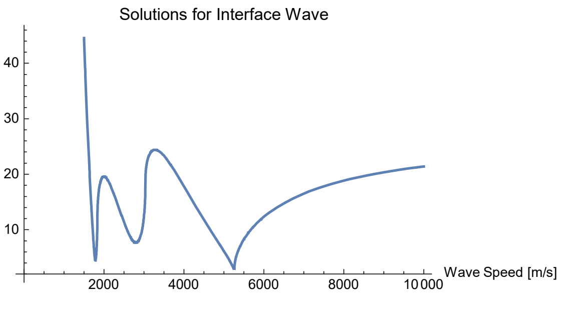

As there is no value for the wavespeed at y=0, no stoneley wave exists for these two materials.

E Wave propagation

Figures of the wave propagation showing P-waves in rock for the calibration models from Section 4.2.1 are presented here.

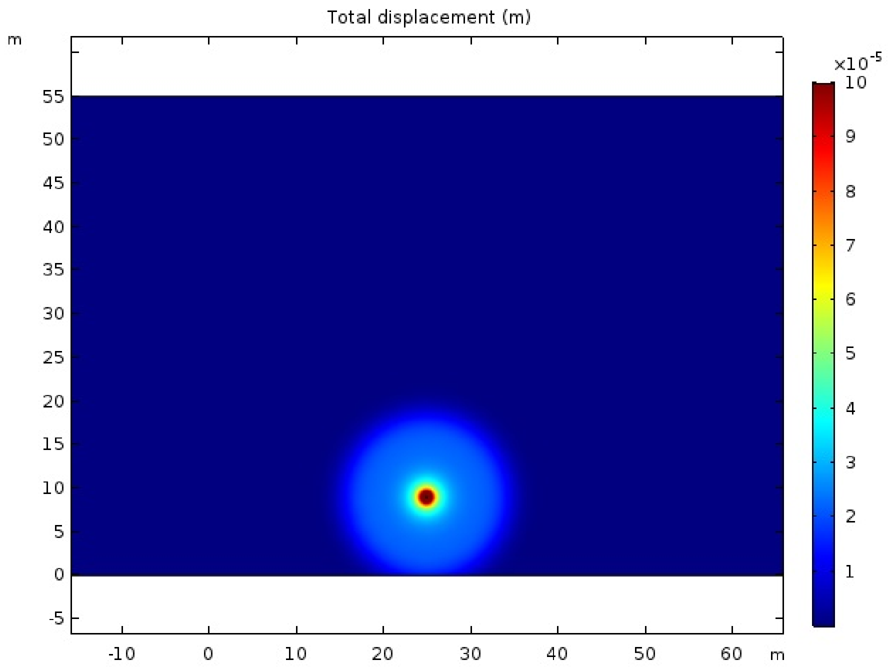

Figure E.1: Total displacement in the domain at time 0.002 s.

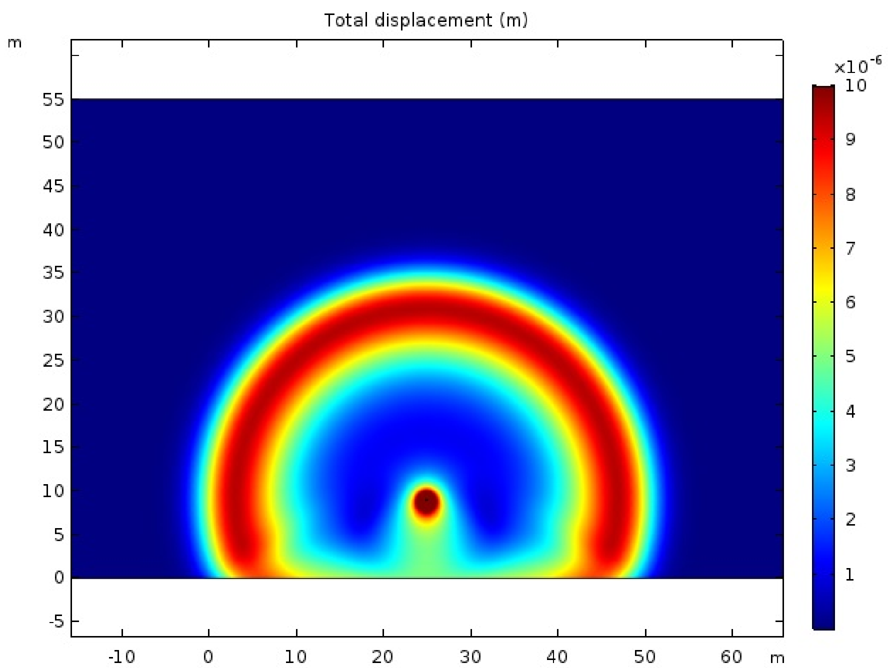

Figure E.2: Total displacement in the domain at time 0.005 s.

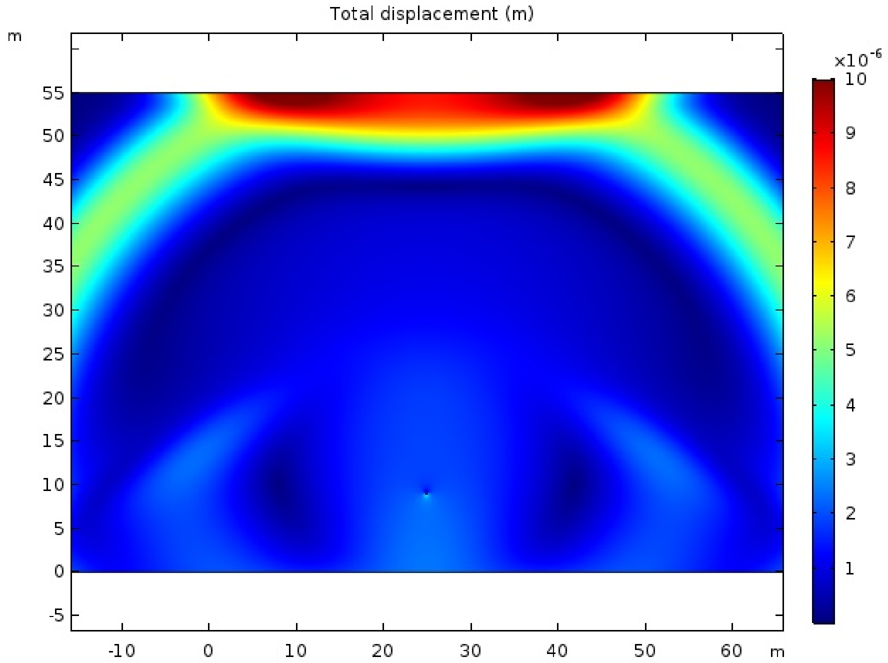

Figure E.3: Total displacement in the domain at time 0.01 s.

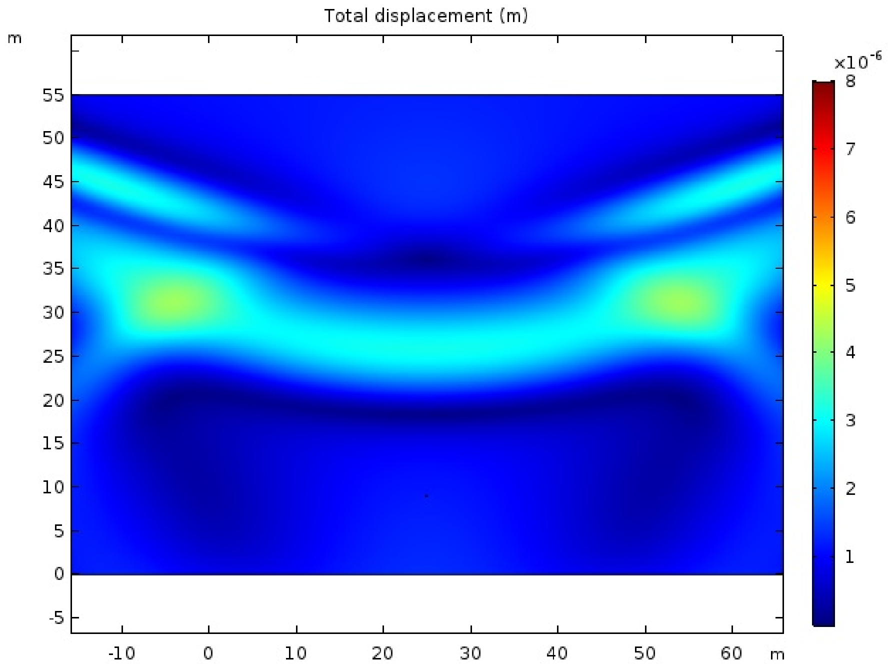

Figure E.4: Total displacement in the domain at time 0.015 s.

Figures of the wave propagation in rock and elastic clay for the calibration models from Section 4.2.1 are presented here. The fast waves are P-waves, the slow horisontal waves are S-waves.

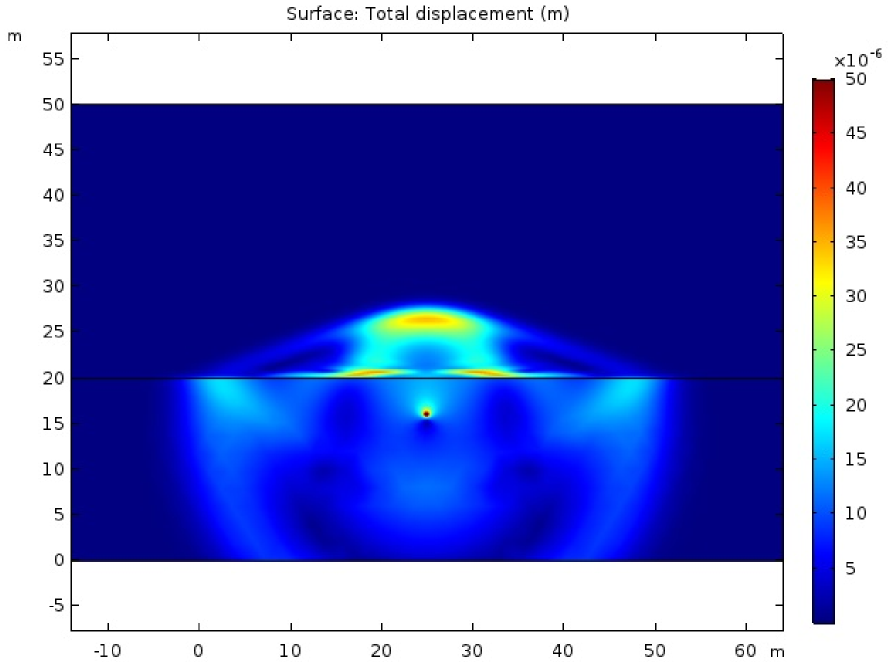

Figure E.5: Total displacement in the domain at time 0.005 s.

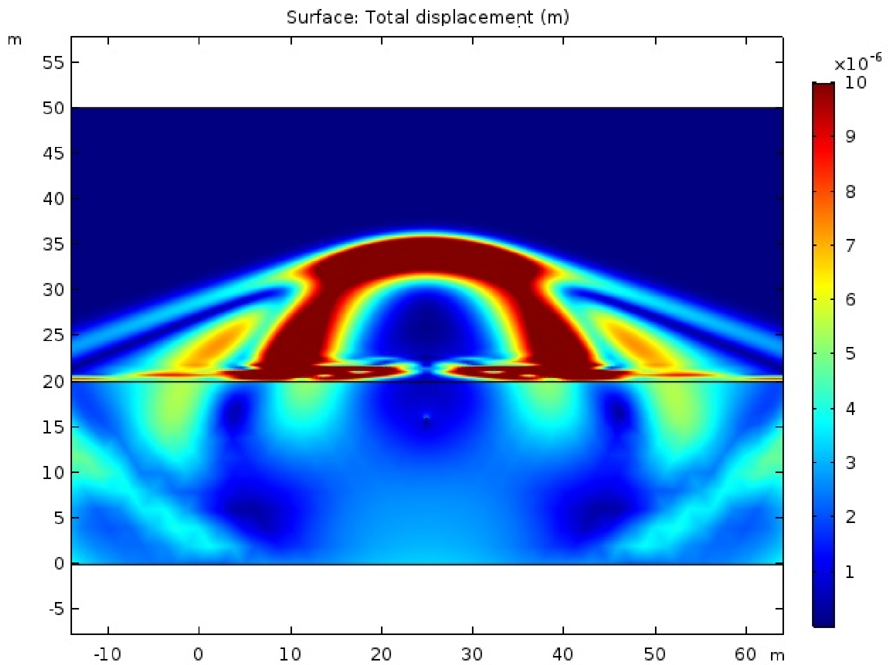

Figure E.6: Total displacement in the domain at time 0.01 s.

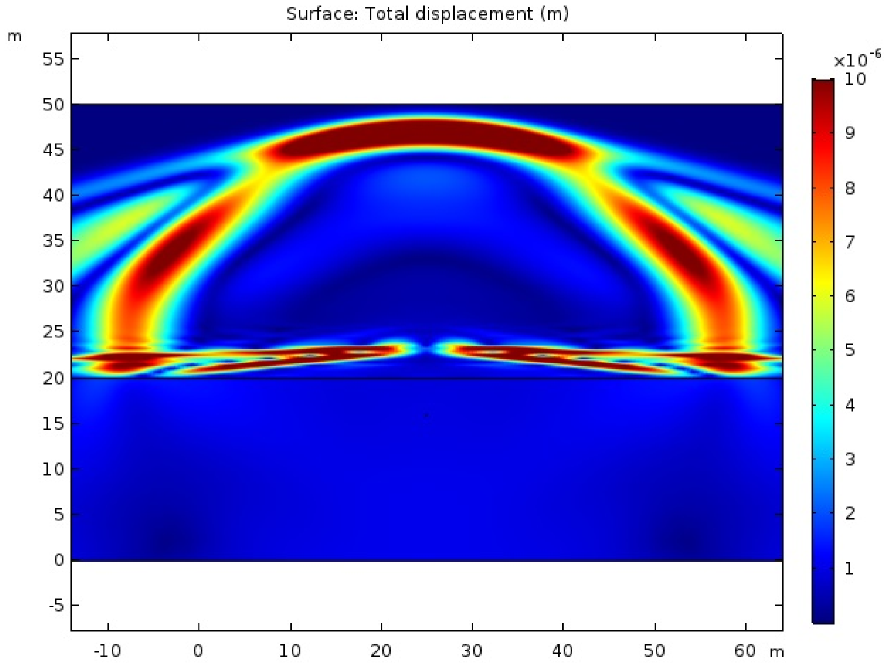

Figure E.7: Total displacement in the domain at time 0.015 s.

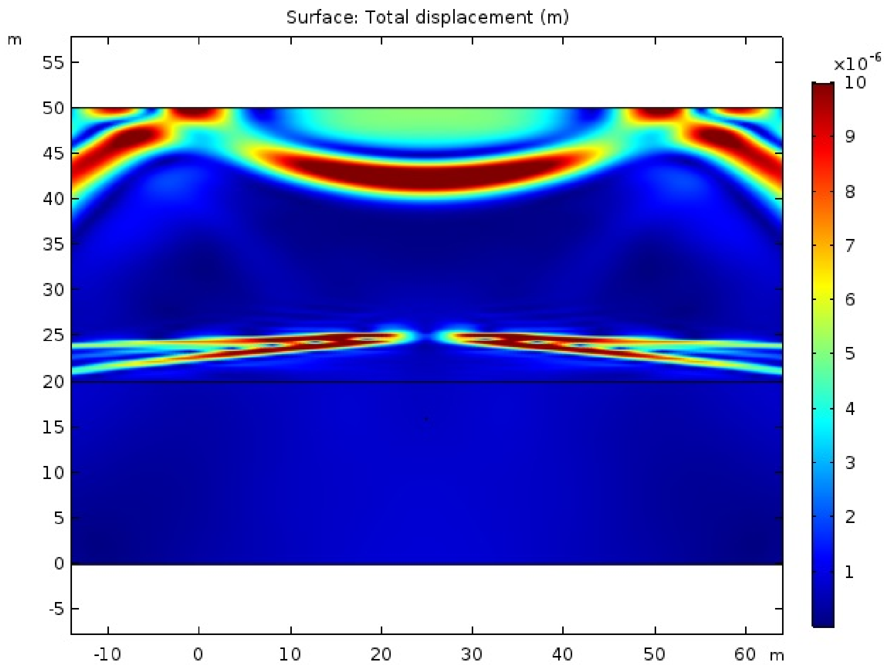

Figure E.8: Total displacement in the domain at time 0.002 s.

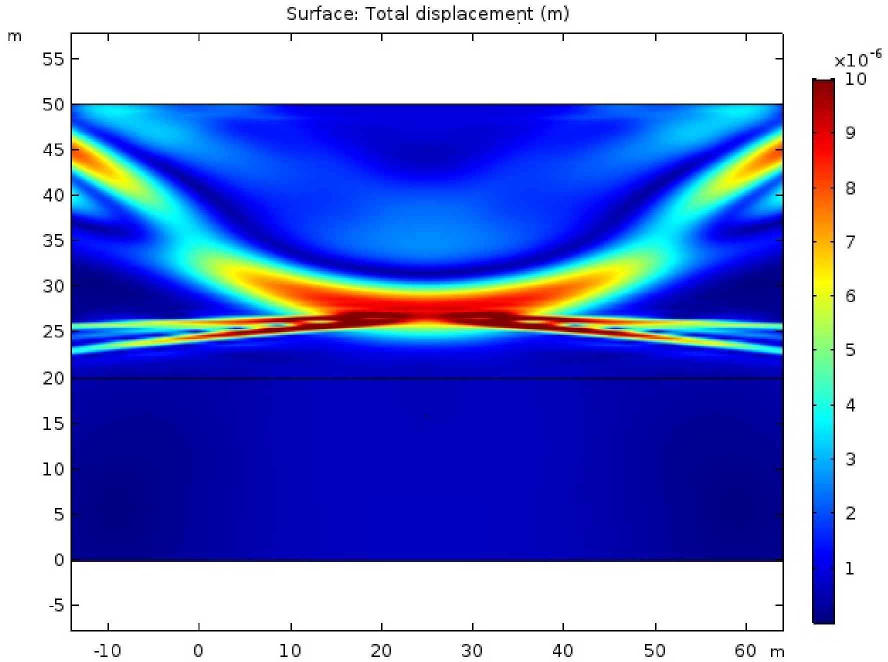

Figure E.9: Total displacement in the domain at time 0.002 s.

Figures of the wave propagation in rock and poroelastic clay for the calibration models from Section 4.2.1 are presented here. The fast waves are P-waves, the slow horisontal waves are S-waves.

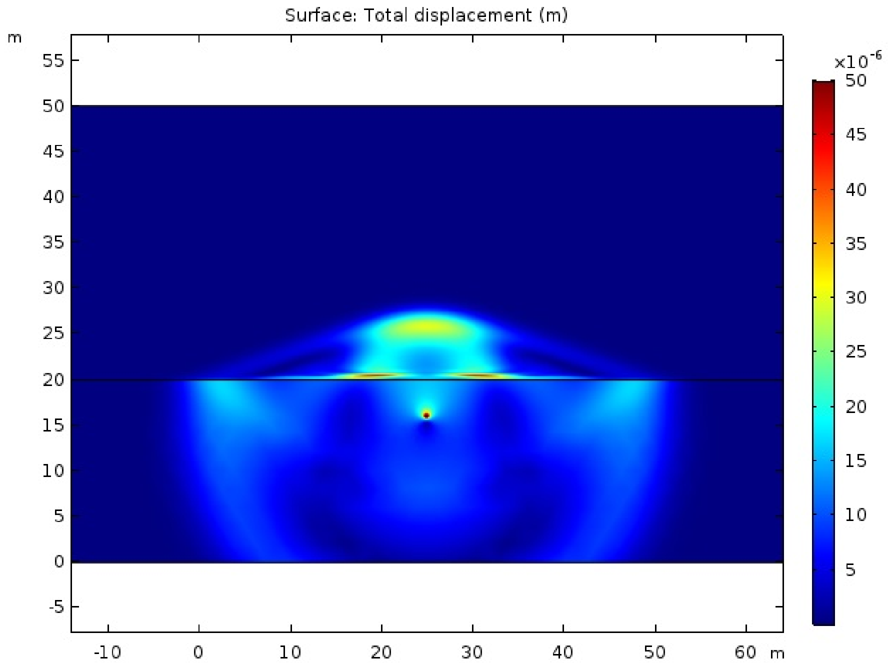

Figure E.10: Total displacement in the domain at time 0.005 s.

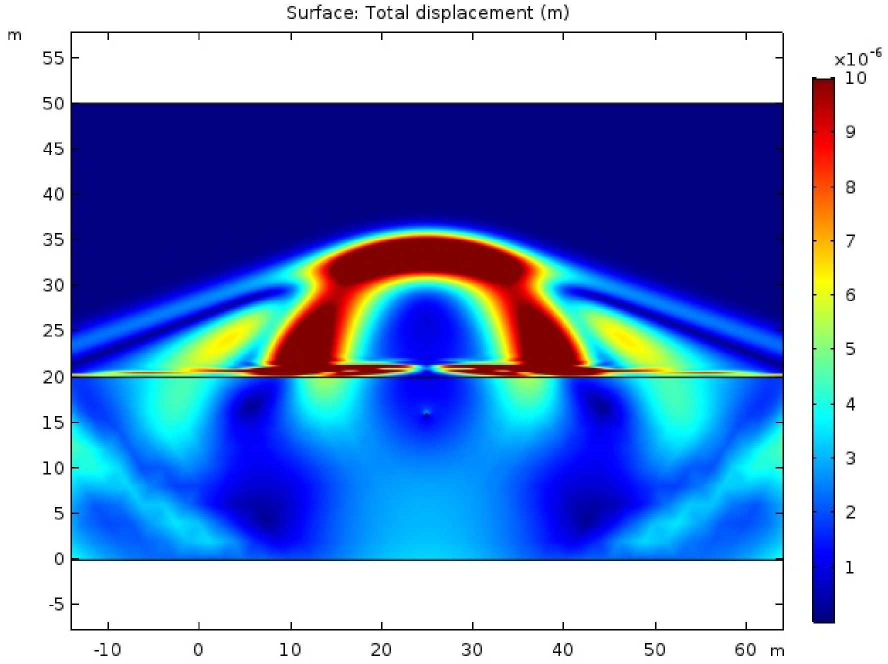

Figure E.11: Total displacement in the domain at time 0.01 s.

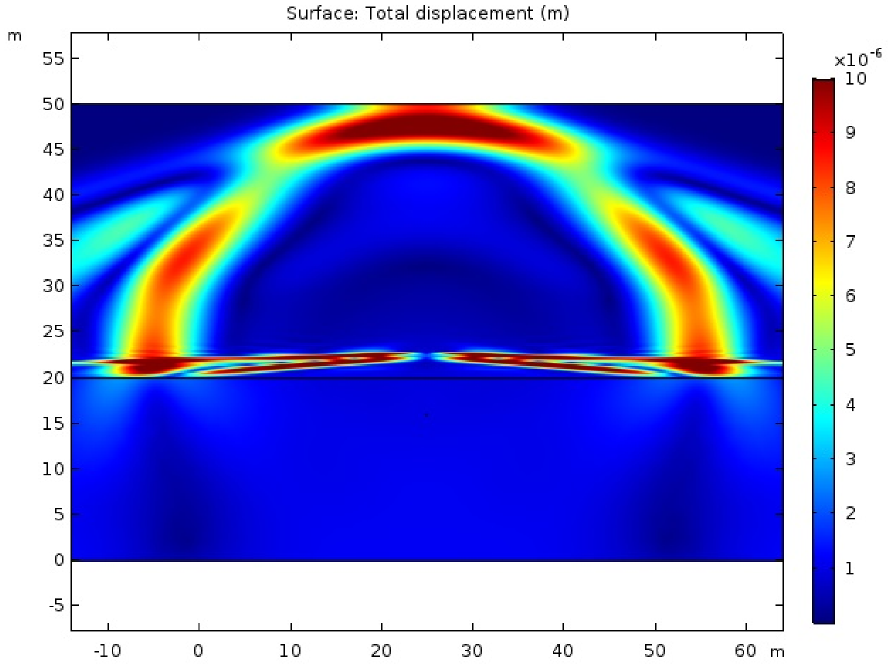

Figure E.12: Total displacement in the domain at time 0.015 s.

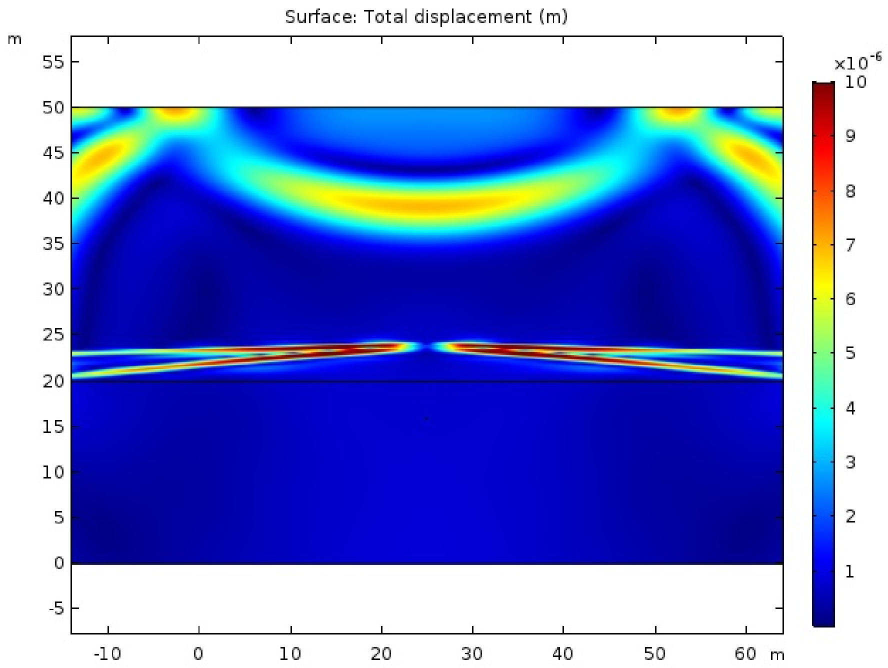

Figure E.13: Total displacement in the domain at time 0.002 s.

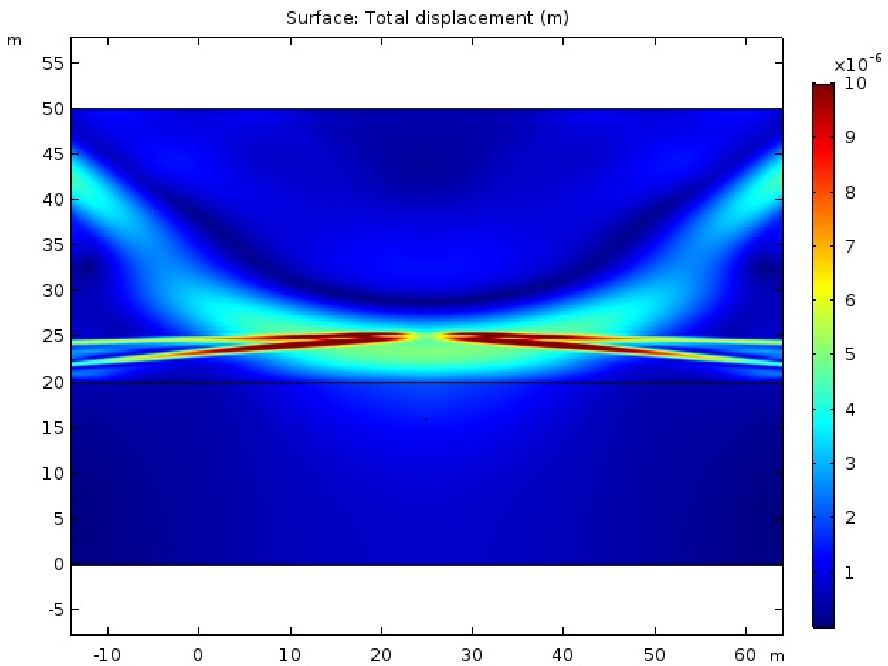

Figure E.14: Total displacement in the domain at time 0.002 s.